Title
Discrete analysis of stochastic NMR

Author
Wong, Sam Tak-Sum

Publication Date
1989

Peer reviewed|Thesis/dissertation

Discrete Analysis of Stochastic NMR

by

Sam Tak-Sum Wong

DISSERTATION

Submitted in partial satisfaction of the requirements for the degree of

DOCTOR OF PHILOSOPHY

in

Bioengineering

in the

GRADUATE DIVISION

of the

UNIVERSITY OF CALIFORNIA

San Francisco

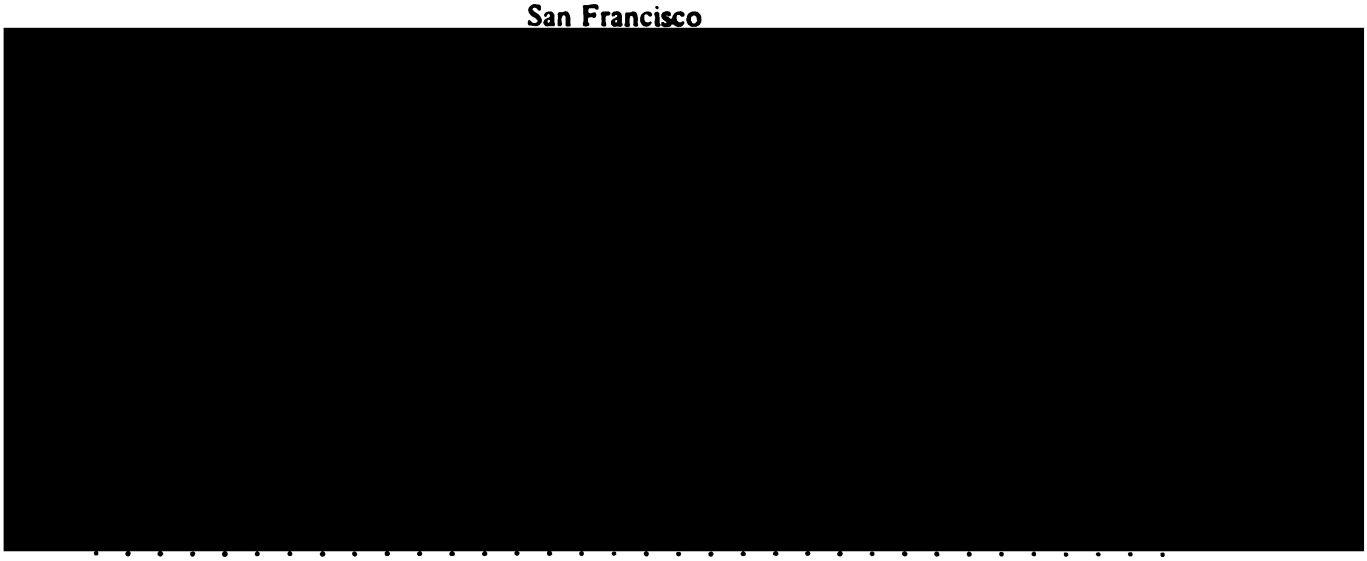

. . . . . .

Date **University Librarian**

Degree Conferred: . . . . . .

Acknowledgements

I wish to give my warmest thanks to Dr. Thomas F. Budinger for his advice, encouragement and funding for this work. Special thanks to Dr. Mark S. Roos for his continuous guidance and supports. Thanks to Dr. Lawrence E. Crooks, Dr. Samuel Patz, Dr. Ronald H. Huesman, Dr. Richard D. Newmark, John R. Baker and Marc L. Kessler for their helpful discussions. Many thanks to Brian L. Knittel for his easy-to-use graphic package that allows me to produce most of the figures. Finally, I would like to thank Dr. Dov Rosenfeld for introducing me to NMR.

This work was partly supported by the Whittaker Foundation (Dr. Mark S. Roos) and the U.S. Department of Energy under contract No. DE-AC03-76SF00098.

Discrete Analysis of Stochastic NMR

By

Sam Tak-Sum Wong

Abstract

Stochastic NMR is an efficient technique for high field *in vivo* imaging and spectroscopic studies in cases where the peak RF power required may be prohibitively high for conventional pulsed NMR techniques. This dissertation presents a theoretical analysis of a stochastic NMR method of acquiring spectroscopy data. The spin system is excited with RF pulses where the flip angles or the phases of the pulses are samples of a discrete stochastic process. The method is formulated as a stochastic difference equation which is then converted to ordinary deterministic difference equations describing the input-output cross-correlation, average signal power and signal power spectrum. The solutions of these equations are used to evaluate the stochastic technique in terms of peak RF power requirement, spectral distortions and signal-to-noise ratio. Experimental results are also presented which verify the results of the discrete analysis.

The analysis shows that the maximum signal-to-noise ratio is achieved when the RMS flip angle is approximately the Ernst angle. When the RMS flip angle is below the Ernst angle, the input-output cross-correlation is a good estimate of the FID. Increase of excitation power causes line broadening. In addition, the use of random flip angle, fixed phase excitation causes a notch artifact and a non-uniform response across the spectrum both of which are not found in two new types of excitation, the random phase excitation and the random quadrature excitation. The signal power spectrum is also a good estimate of the real spectrum. The approximation of the cross-correlation by a time average causes systematic noise. The amount of systematic noise is found to

be significantly reduced when an entire maximum length sequence (MLS) is used for excitation. Noise-like distortion at high power MLS excitation is discovered to be related to the number of feedback paths in the MLS generator, more feedback paths gives less distortion.

This analysis shows that stochastic NMR with random phase excitation or random quadrature excitation using MLS is simple to implement and is an effective technique for high field *in vivo* NMR studies.

Contents

List of Figures

Symbol Table

Symbol	Definition and page number
α	RMS flip angle 15
$\boldsymbol{\alpha}(n)$	Stochastic RF excitation sequence, $[\alpha_x(n), \alpha_y(n), 0]^T$ 15
α_{max}	RMS flip angle that maximizes the S/N ratio 28
$\beta(n)$	Magnitude of $\boldsymbol{\alpha}(n)$ 45
δ_{mn}	Kronecker delta function 15
θ	Interpulse dephase, $2\pi\nu T_R$ 16
θ'	Effective interpulse dephase, $2\pi\nu' T_R$ 26
$\boldsymbol{\mu}_\alpha$	Mean of $\boldsymbol{\alpha}(n)$, $[\mu_x, \mu_y, 0]^T$ 15
$\boldsymbol{\mu}_M$	Mean magnetization, $\langle \boldsymbol{M}(n) \rangle$ 17
$\boldsymbol{\mu}_R$	Mean RF rotation matrix, $\langle \boldsymbol{R}_\alpha(n) \rangle$ 17
ν	Resonance offset of the spins 16
ν'	Resonance offset of the reconstructed line 26
σ^2	Measurement noise variance 60
$\phi(n)$	Phase of $\boldsymbol{\alpha}(n)$ 37
$\varphi_\alpha(t)$	Characteristic function of the random variable $\alpha_x(n)$ 21
$\dot{\varphi}_\alpha(t)$	First derivative of $\varphi_\alpha(t)$ 22

Symbol	Definition and page number
$\boldsymbol{A}$	Cross-covariance of $\boldsymbol{M}(n)$ and $\boldsymbol{\alpha}(n)$ 18
$\boldsymbol{B}$	$[1, -i, 0]^T$ 17
$\boldsymbol{C}$	$[0, 0, M_e(1 - E_1)]^T$ 16
$\boldsymbol{C}_\alpha$	Auto-covariance of $\boldsymbol{\alpha}(n)$ 15
$D(\omega)$	Denominator of $F(\omega)$ 22
E_1	T_1 relaxation, e^{-T_R/T_1} 16
E_2	T_2 relaxation, e^{-T_R/T_2} 16
$F(\omega)$	Line shape of $K_1(\omega)$ 22
${}_1F_1$	Degenerate hypergeometric function 48
G_j	The j^{th} order Wiener functional 34
$g(x)$	 48
H_j	The j^{th} order Volterra functional 33
$h_1(m)$	The first order Volterra kernel, the FID 35
i	$\sqrt{-1}$ 11
$K_1(\omega)$	Fourier transform of $k_1(m)$ 19
$K_{1(3)}(\omega)$	Fourier transform of $k_{1(3)}(m)$ 35
$K_{1(5)}(\omega)$	Fourier transform of $k_{1(5)}(m)$ 36
$k_1(m)$	The first order input-output cross-covariance 17
$k_1^N(m)$	$k_1(m)$ estimated by time averaging 60
$\tilde{k}_1^N(m)$	$k_1^N(m)$ calculated with a noisy signal 61
$k_{1(3)}(m)$	1^{st} order derived kernel of the 3^{rd} order Wiener kernel 35
$k_{1(5)}(m)$	1^{st} order derived kernel of the 5^{th} order Wiener kernel 35
$\boldsymbol{M}(n)$	Magnetization vector, $[M_x(n), M_y(n), M_z(n)]^T$ 11

Symbol	Definition and page number
M_e	Equilibrium longitudinal magnetization 15
$M_{xy}(n)$	Complex transverse magnetization, $M_x(n) + i\, M_y(n)$ 11
N	Number of data points used to calculate the time average 60
$\mathcal{N}(n)$	Measurement noise sequence, $[\mathcal{N}_x(n), \mathcal{N}_y(n), 0]^T$ 60
P	Average signal power 19
$\boldsymbol{R}_\alpha(n)$	RF rotation matrix for the n^{th} pulse 16
$\boldsymbol{R}_\theta$	Rotation matrix summarizing interpulse dephase and relaxation 16
$r(m)$	Auto-covariance of the complex signal 19
$r^N(m)$	$r(m)$ estimated by time averaging 60
$\tilde{r}^N(m)$	$r^N(m)$ calculated with a noisy signal 62
$S(\omega)$	Signal power spectrum, Fourier transform of $r(m)$ 20
T_1	Spin-lattice relaxation time constant 16
T_2	Spin-spin relaxation time constant 16
T_R	Duration between two consecutive RF pulses 9

Chapter 1

Introduction

1.1 Motivation

In vivo NMR is an excellent non-invasive technique to obtain information about the chemical composition and physical environment of living tissues. NMR signals arise from the transitions of nuclear spins from a higher to a lower energy state. Observable transitions are dependent on the population difference of the spin states, which is on the order of parts per million (ppm) or less. The intrinsic low sensitivity is made worse by the low magnetic moments and small isotopic abundance of the spin $\frac{1}{2}$ nuclei of biological interest. For example, ^{13}C has a natural abundance of only 1.1% and a magnetic moment one-fourth that of ^{1}H. Improvement of signal-to-noise (S/N) ratio becomes a major issue in studies designed to evaluate ^{13}C *in vivo*.

In 1966, Ernst *et al* [1] introduced pulsed Fourier Transform NMR (FT-NMR) as an alternative to continuous wave NMR. FT-NMR rapidly became the more popular modality due to its better signal-to-noise (S/N) ratio. Nowadays, scientists are pushing for higher and higher magnetic field strength because the S/N ratio for a weakly conducting sample is proportional to the magnetic field strength [2]. Whole body spectrometers with fields up to 10 Tesla have been proposed. The availability of high current density superconducting materials allows such high field superconducting magnets to be constructed. The power needed for the NMR spectroscopy experiment is determined by the excitation bandwidth, which in turn is proportional to the range of chemical shift

in the sample, which is proportional to the magnetic field. The excitation bandwidth also determines the duration of the RF pulse in pulsed FT-NMR. For a given range of chemical shift of interest, an increase in field strength corresponds to a decrease in pulse duration. This implies that the peak RF power has to be increased in order to deliver the same amount of RF energy to the sample. For example, a 20μsec 90° RF pulse for ^{13}C spectroscopy of the human head in a 4.7 Tesla static field requires a peak power of approximately 400 KW. Such high peak power imposes considerable difficulties in hardware design.

In a conventional pulsed FT-NMR experiment, a short (10 to 100 μsec) RF pulse is usually repeated at intervals comparable to the longitudinal relaxation time constant T_1 (typically 10^{-2} to 10^2 seconds). This corresponds to a very small duty cycle for the RF amplifier. Stochastic excitation reduces the peak RF power requirement by several orders of magnitude by increasing the duty cycle of the RF excitation, i.e. by delivering the RF excitation energy more evenly in time (Figure 1.1). It is an efficient technique especially for high field *in vivo* imaging and spectroscopic studies where the peak RF power required may be prohibitively high for conventional pulsed NMR techniques. Ernst [3] and Kaiser [4] have shown that stochastic NMR not only eases the RF instrument design but also provides a sensitivity and a controllable resolution similar to those of conventional pulsed FT-NMR.

1.2 Basic Principle and Historical Development

The underlying principle of stochastic NMR comes from linear system theory. The impulse response of an unknown linear system is given by the cross-correlation of the input and output of the system when the system is excited by zero mean Gaussian white noise [5] (Figure 1.2a). To understand this mathematically we let $h(t)$ be the impulse response of the unknown system. The input $x(t)$ and the output $y(t)$ is related by the

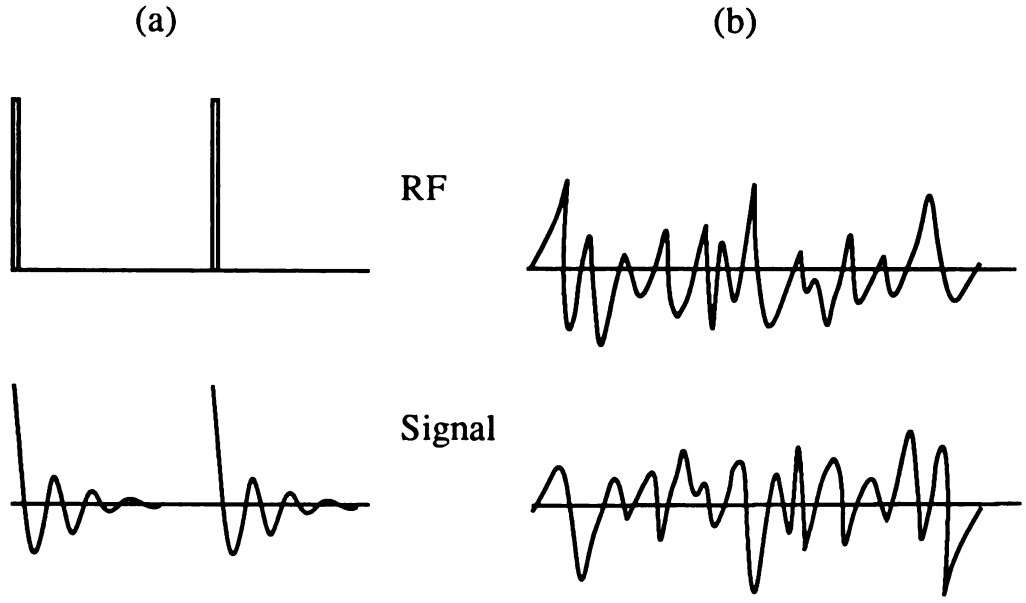

Figure 1.1: (a) Conventional pulsed FT-NMR, (b) Stochastic excitation.

convolution operation:

$$y(t) = \int_{-\infty}^{\infty} h(\tau)\, x(t-\tau)\, d\tau. \tag{1.1}$$

A zero mean Gaussian white noise input satisfies the condition

$$\langle x(t)\, x^*(t-\tau)\rangle = \sigma^2\, \delta(\tau) \tag{1.2}$$

where the angle brackets denote expectation, the superscript * indicates complex conjugate, σ^2 is the average noise power and $\delta(t)$ is the delta function. The input-output cross-correlation defined as follows gives the impulse response of the linear system:

$$\begin{aligned}
\frac{1}{\sigma^2}\,\langle y(t)\, x^*(t-t')\rangle &= \frac{1}{\sigma^2}\langle \int_{-\infty}^{\infty} h(\tau)\, x(t-\tau)\, x^*(t-t')\, d\tau\rangle \\
&= \frac{1}{\sigma^2}\int_{-\infty}^{\infty} h(\tau)\,\langle x(t-\tau)\, x^*(t-t')\rangle\, d\tau \\
&= \frac{1}{\sigma^2}\int_{-\infty}^{\infty} h(\tau)\,\sigma^2\,\delta(\tau-t')\, d\tau \\
&= h(t'). \qquad (1.3)
\end{aligned}$$

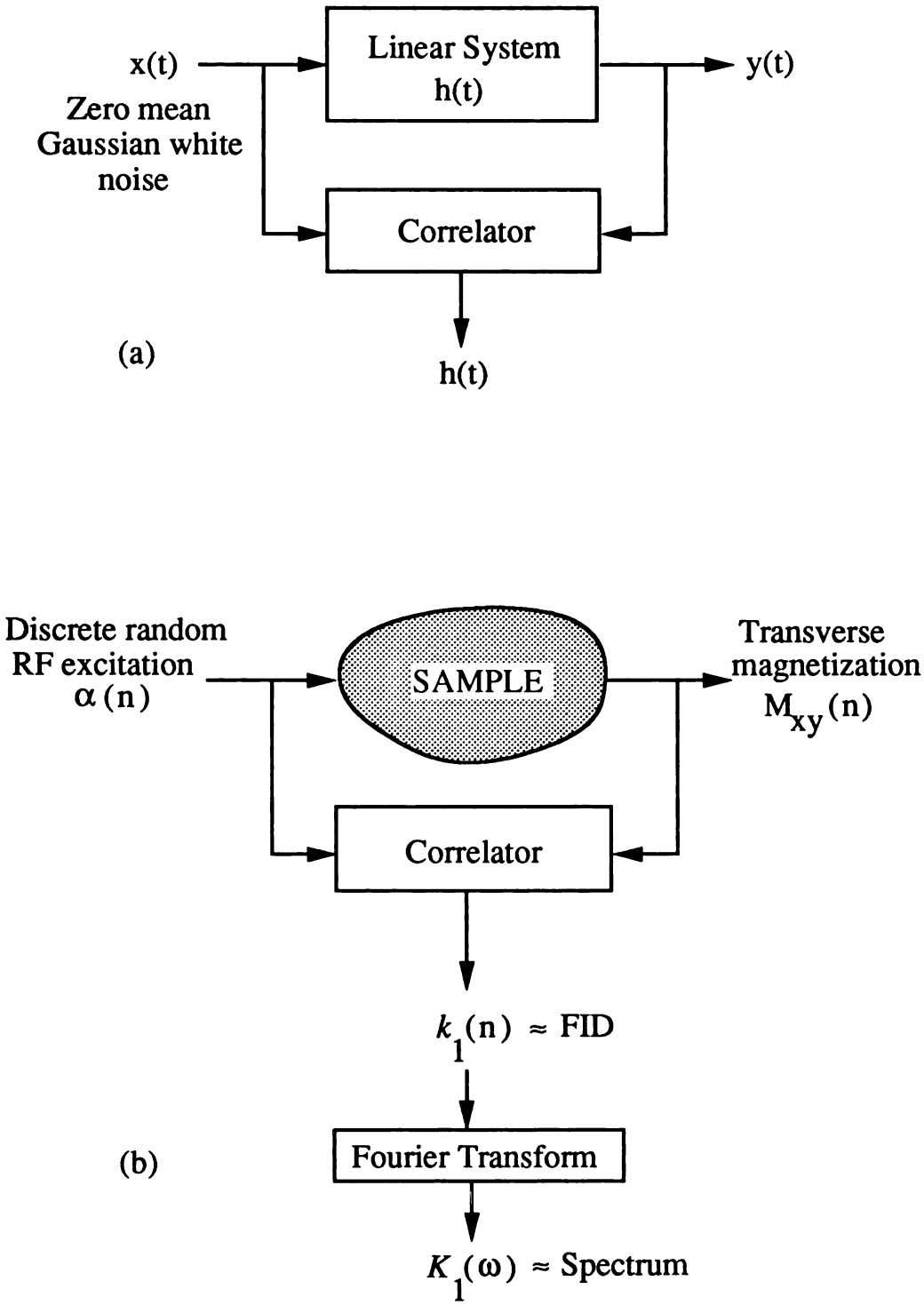

Figure 1.2: (a) Identification of the impulse response $h(t)$ of a linear system by the cross-correlation of the input $x(t)$ and the output $y(t)$ of the system. (b) The same principle applied to stochastic spectroscopy experiment and spectral estimation.

This principle was first applied to stochastic NMR by Ernst [3] and Kaiser [4] independently in 1970. The NMR spin system was excited by a stochastic RF signal. The first order input-output cross-correlation was used to approximate the FID obtained by a pulsed FT-NMR experiment (Figure 1.2b). The Fourier transform of the cross-correlation was an estimate of the true spectrum. Pulsed FT-NMR has since become a more popular technique for most experiments because the hardware design is simpler and the reconstructed spectra have less nonlinear distortions and no systematic noise. However, stochastic NMR does have advantages over pulsed FT-NMR as discussed in the previous section.

Based on Wiener's theory of nonlinear systems with Gaussian white noise excitation [6,7], Ernst expanded the magnetization response of the stochastic experiment into sums and products of orthogonal Hermite polynomials. From such expansions, he obtained expressions for the input-output cross-correlation, signal power spectrum and the average signal power. The Fourier transform of the input-output cross-correlation was used to approximate the desired spectrum (Figure 1.2b). His results showed no saturation effects detectable in the line shape. He demonstrated the stochastic technique experimentally with binary maximum length sequence (MLS) excitation. Each random bit of a binary MLS is generated from the n preceeding ones, where n is arbitrary. The MLS has a period of $2^n - 1$, the maximum possible sequences of n binary bits (except all zeros) [8]. Kaiser restricted his analysis to small excitation power so that the signal response could be regarded as a linear function of the excitation and the principle behind Equation 1.1-1.3 was applicable. Both his analysis and experimental results were based on continuous Gaussian white noise excitation. In 1974, Kaiser [9] showed that with binary MLS excitations, the input-output cross-correlation could be processed by Hadamard transforms which required no multiplication, and hence is even faster than the FFT. In addition, the periodicity of the binary MLS allowed coherent signal averaging to be used to improve the S/N ratio.

In 1976, Bartholdi *et al* [10] did a rigorous calculation of the input-output cross-correlation, signal power spectrum and the average signal power by interpreting the Bloch equations as a stochastic differential equation and solved the equation using Itô and Stratonovich calculus. They showed that the use of ordinary calculus to solve a stochastic differential equation, as was done in Ernst's 1970 paper, might lead to incorrect results. Their computer simulated results showed that the estimated spectral line broadened as the excitation power was increased.

Six years later Knight and Kaiser [11,12], using a different approach, repeated the theoretical calculations done by Bartholdi *et al.* Instead of solving the stochastic differential equation for the magnetization response using Itô and Stratonovich calculus, they converted the stochastic differential equation to ordinary differential equations describing the various product terms needed for the calculation of the input-output cross-correlation, the signal power spectrum and the average signal power. They performed the analysis for both one spin and multi-spin systems using, respectively, the Bloch equations and the equation of motion of the spin density matrix. For the one spin analysis, their results differed from those obtained by Bartholdi *et al* slightly regarding line broadening and spectral shift. The reason for the discrepancy is that the two groups obtained two different halves of the actual solution. Bartholdi *et al* obtained the solution for spins at resonance, while Knight and Kaiser obtained the solution for spins off resonance. It will be shown in Chapter 2 that the responses to spins on resonance and spins off resonance are indeed different.

Knight and Kaiser's analysis also showed that the higher order input-output cross-correlations are related to multi-dimensional spectroscopic data obtained by conventional pulsed FT-NMR. These correlations are the expectation of the product of the output and multiple versions of the input with different time lags. The same set of data that is used to estimate the one dimensional spectrum can also be used to study the correlations between different resonances and multiple-quantum coherence effects in

complex spin systems. This was demonstrated experimentally by Blümich and Ziessow [13,14,15,16,17,18,19,20].

The use of time varying gradients in stochastic experiments to encode spatial information was first proposed by Blümich in 1984 [21]. He worked out the principle for spatial encoding with stochastic gradients and demonstrated the idea with computer simulations. However, the idea is impractical due to tremendous difficulties in implementing stochastic gradients in hardware. The stochastic NMR spectroscopy experiment can easily be converted to an imaging experiment by applying constant gradients throughout the experiment as demonstrated by Chaudhuri in 1986 [22]. The reconstructed spectrum will be a projection of the sample along a direction orthogonal to the direction of the resultant gradient vector. A set of projects can be obtained by changing the direction of the gradient vector. A three dimensional image can be reconstructed from the set of projections by back-projection reconstruction techniques. Chaudhuri used binary MLS excitations and he reported artifacts in the middle of the reconstructed image as the excitation is increased. The reason for such distortion will be addressed in Chapter 2.

In 1986, Blümich proposed an alternative to stochastic gradients, the use of sinusoidal gradients with incommensurate frequencies that are also incommensurate to the data sampling frequency. His idea was pursued further in 1988 by Roos *et al* [23]. They obtained theoretical expressions describing the spatial localization function achieved with sinusoidal gradients. The idea was further extended to chemical shift imaging and localized spectroscopy with stochastic excitation and was verified experimentally.

1.3 Aims and Contributions

So far, all the analyses of the stochastic experiment for a one spin system have assumed continuous random excitation. Continuous random excitation is undesirable from a practical experimental point of view since the RF transmitter of a NMR system that is set up

for FT-NMR is usually gated off during data sampling in order to avoid saturation of the receiver. The theoretical analysis based on continuous excitation is at best an approximate description of the experiment performed on such NMR systems. It is more appropriate to perform the discrete stochastic experiment shown in Figure 1.3: A stochastic sequence of RF excitations, $\alpha(n)$, is applied at intervals of T_R seconds and one data point is sampled after every RF pulse. It is the aim of this dissertation to characterize the discrete stochastic spectroscopy experiment, obtaining analytic results that correspond exactly to practical experiments. The results will also be applicable to stochastic NMR imaging experiments with constant gradients.

The driven NMR spin system is intrinsically nonlinear. The magnetization response is a nonlinear function of the RF excitation. A single one pulse excitation will give a FID, which is proportional to the linear component of the nonlinear spin system. When a sequence of pulses are applied, the response after the second pulse will no longer be a pure FID. This is the reason why pulsed FT-NMR requires a considerable time delay after data sampling before the next RF pulse is applied. In stochastic NMR, RF pulses with low power are applied in rapid succession. The spin system can easily be pushed towards the nonlinear regime. The first order input-output cross-correlation shown in Figure 1.2b will not always give the FID. The first objective of this dissertation is to understand the performance of the discrete stochastic NMR experiment by analyzing the follow aspects of the experiment:

- The conditions for the first order input-output cross-correlation to be a faithful estimate of the FID obtained by a pulsed FT-NMR experiment,
- the saturation behavior when the excitation power is high,
- the experimental parameters that give maximum S/N ratio, and
- evaluation of the signal power spectrum as an alternative estimate of the true spectrum.

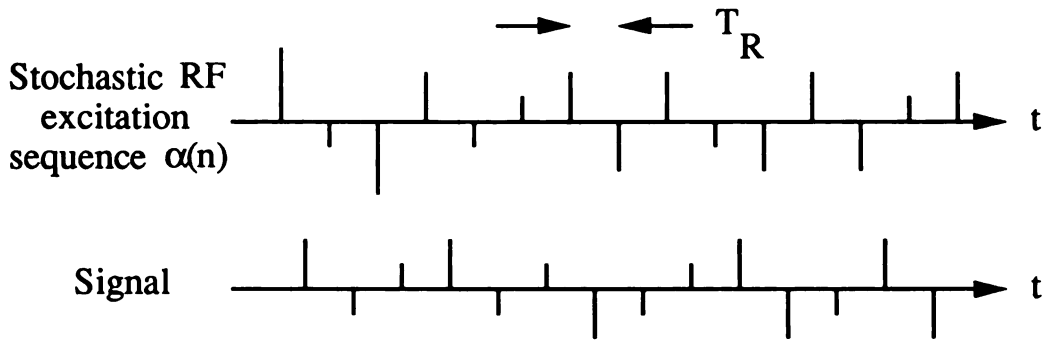

Figure 1.3: NMR experiment with discrete stochastic RF excitation.

In all past analyses, the RF vector was assumed to lie along one axis in the rotating frame with the flip angle being random. This type of excitation will be denoted as random flip angle excitation (Figure 1.4a). The analysis in the next chapter will show that this type of excitation causes undesirable spectral distortions as the RF excitation power is increased. This result will be used to explain discrepancies and artifacts in earlier results [10,12,22]. Chapter 2 will analyze two new types of random RF excitations that do not exhibit such artifacts. One type will be denoted as random phase excitation. The RF pulses of this type of excitation have the same flip angles. However, the phase of the RF vector is random (Figure 1.4b). The other type is denoted as random quadrature excitation: The RF vector consists of two orthogonal components that are statistically uncorrelated but identically distributed in probability (Figure 1.4c).

Due to the stochastic nature of the experiment, all quantities estimated from the stochastic input and output of the system should be regarded as random variables, i.e. they are intrinsically stochastic in nature. The input-output cross-correlation, being an estimator of the spectrum, is one such quantity. The variance of the estimator, denoted as systematic noise, is usually non-white and may show up as structural artifacts. The

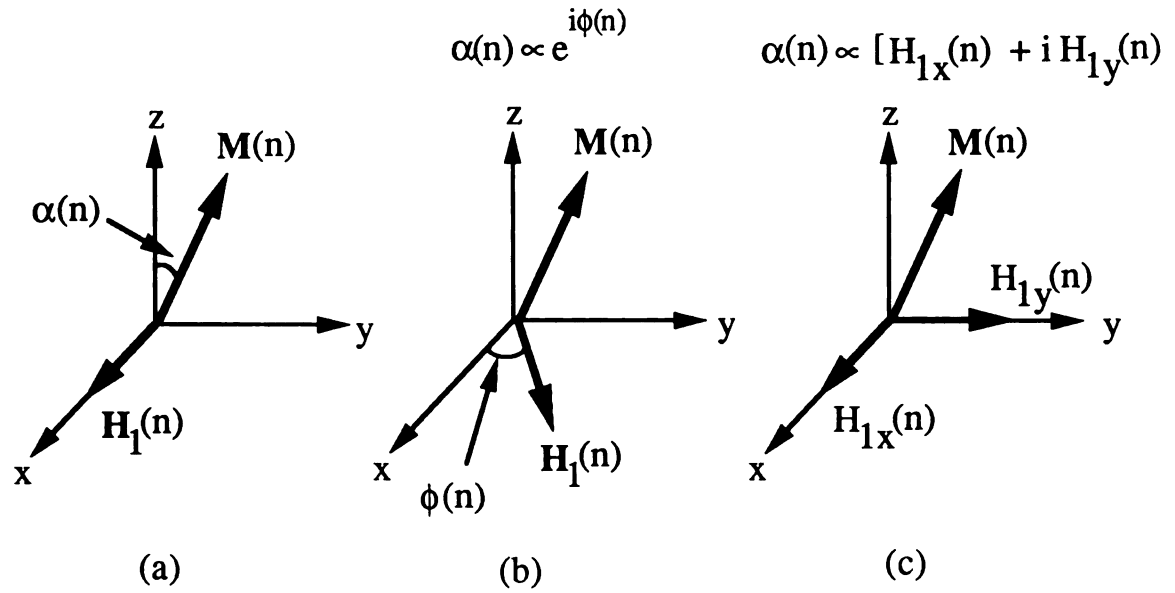

Figure 1.4: Different types of stochastic RF excitation. (a) Random flip angle excitation, (b) Random phase excitation, and (c) Random quadrature excitation. $\mathbf{H}_1(n)$ is the RF vector with components $H_{1x}(n)$ and $H_{1y}(n)$, $\mathbf{M}(n)$ is the magnetization vector.

overall noise level is determined by the sum of systematic noise and measurement noise. It is important to keep the systematic noise level below measurement noise level so that no structural artifact is observable. Chapter 3 is devoted to the analysis of systematic noise. It also includes a detailed account of the nonlinear systematic noise associated with binary MLS excitations reported by Blümich and Ziessow [14].

So far, binary random sequences and discrete Gaussian white noise are the two most popular stochastic sequences to be employed in stochastic NMR experiments. Binary random excitations are popular because they can be approximated by pseudo random binary MLS. Binary MLS has the advantage that it is easy to implement in hardware [8] and it allows the Hadamard transform to be used to speed up the calculation of cross-correlations. Gaussian white noise has good statistical properties that simplify theoretical analysis tremendously. This dissertation will compare the two types of stochastic

sequences in terms of their performance in spectral estimation and systematic noise generation.

1.4 Approaches

The approach taken is shown as a block diagram in Figure 1.5. In the block diagram $\boldsymbol{M}(n) = [M_x(n), M_y(n), M_z(n)]^T$ is the magnetization vector immediately after the n^{th} RF pulse, where the superscript T is the matrix transpose operator. The complex quantity $M_{xy}(n) = M_x(n) + i\, M_y(n)$ is the transverse magnetization. Quadrature detection gives a signal proportional to $M_{xy}(n)$. From the Bloch equation, a stochastic difference equation describing the pulse-to-pulse behavior of $\boldsymbol{M}(n)$ is derived. Instead of solving this stochastic difference equation, it is combined with the excitation sequence $\alpha(n)$ to give a deterministic difference equation describing the cross-correlation of $\boldsymbol{M}(n)$ and $\alpha(n)$, which can then be solved to obtain the input-output cross-correlation. The Fourier transform of the cross-correlation gives an estimate of the spectrum. The estimate can be used to study the saturation effects as the excitation power is increased.

From the stochastic difference equation an equation of the covariance matrix of $\boldsymbol{M}(n)$ can be obtained. This equation is a set of six simultaneous equations with six unknowns which are the variances and covariances of $M_x(n)$, $M_y(n)$ and $M_z(n)$. The average signal power is the sum of the variances of $M_x(n)$ and $M_y(n)$. A plot of the average signal power will show the excitation power level that will give the maximum S/N ratio. The stochastic difference equation can also be turned into a difference equation for the auto-correlation matrix of the magnetization vector $\boldsymbol{M}(n)$. The sum of the first two diagonal elements of the auto-correlation matrix is the auto-correlation of the transverse magnetization. The Fourier transform of this sum gives the signal power spectrum. The first section of the next chapter will be an analysis for a generalized stochastic RF excitation. The results of the generalized analysis will be made specific in the subsequent three

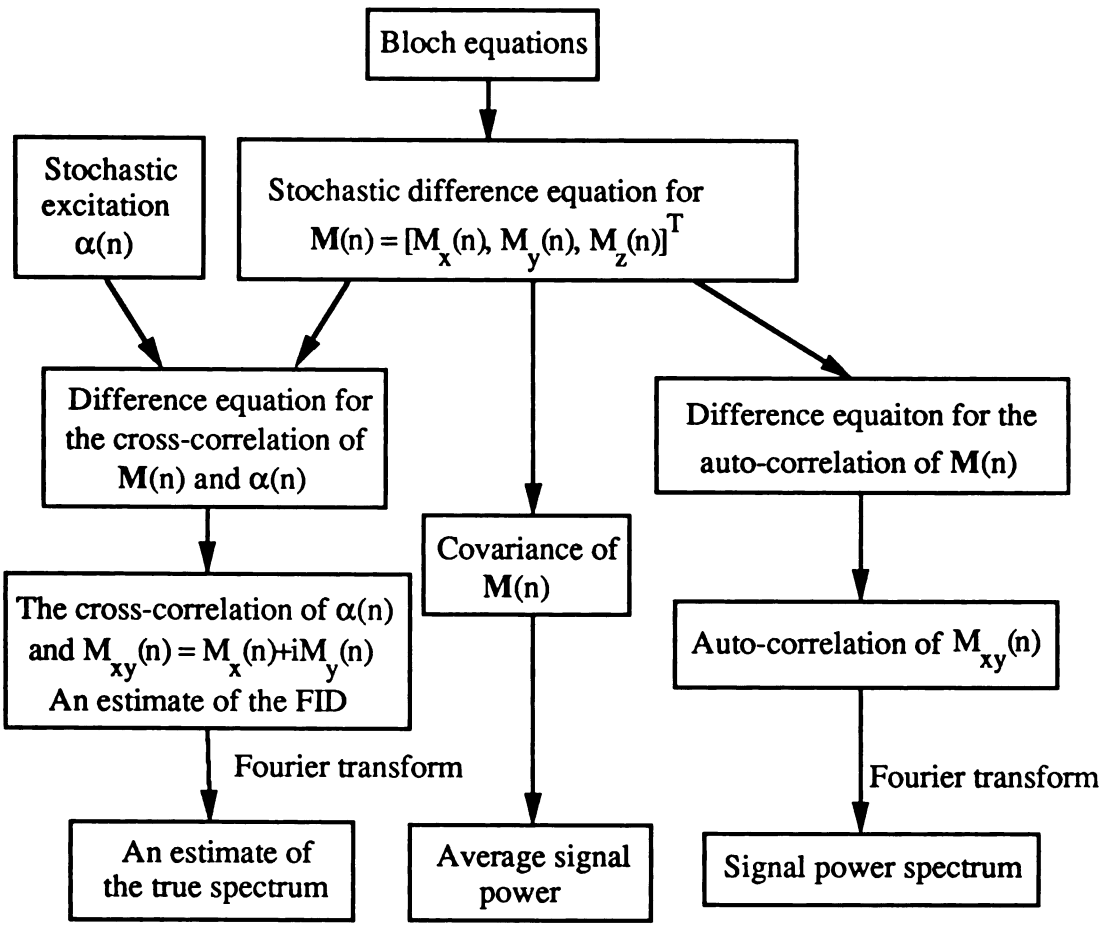

Figure 1.5: Approach taken for the theoretical analysis.

sections each of which will be devoted to one of the three types of stochastic excitations shown in Figure 1.4.

Theoretical prediction of the systematic noise is a formidable task. Analytical results for only the cases of random flip angle excitation with Gaussian white noise and random quadrature excitation with random binary sequences are presented here. Most of the results for systematic noise analysis will be obtained by Monte Carlo simulations. Pseudo-random number generators for MLS and Gaussian white noise described in [8] will be used to simulate the random RF excitation. The transverse magnetization after each pseudo-random RF pulse is calculated from the stochastic difference equation. This

pseudo-random output signal together with the theoretical results obtained in Chapter 2 is used to calculate the systematic noise. All the Monte Carlo simulations are performed on a Cray-XMP in the Lawrence Livermore Laboratory.

1.5 Assumptions

The major assumption made in this analysis is that spins are isolated so that the Bloch equations are applicable, thus the results are valid only for one spin systems. Derivation of explicit expressions describing the stochastic responses and reconstructed spectra is made possible by the assumption of wide-sense stationary excitation sequences on a stationary NMR spin system. A stationary spin system here means that the spins do not experience a change in spin characteristics, e.g. T_1, T_2 and resonance offset, during the experiment. Such a change of characteristics may be caused by motions of the sample in the presence of a magnetic field gradient, application of a time varying gradient or a fluctuation in the static magnetic field, etc.. A stochastic sequence $x(n)$ is said to be wide-sense stationary if it possesses finite second moments and its auto-correlation $\langle x(n)x^*(m)\rangle$ is a function only of the absolute difference $|n-m|$. A variety of algorithms are available to generate pseudo-random sequences that are wide-sense stationary [24].

Another major assumption regarding data reconstruction is the assumption of ergodicity. The calculations of input-output cross-correlation, average signal power and signal power spectrum all involve taking the expectation of stochastic sequences. The expectation can be obtained by ensemble averaging. In terms of the stochastic NMR experiment, this means repeating the experiment many times and taking the average of the results from each run. However, there is a waiting period at the beginning of the experiment for the average magnetization to acquire a steady state. The data collected in this period cannot be used in the reconstruction. This loss of experiment time can

be avoided by replacing the ensemble averaging by time averaging. For example, the auto-correlation of the stochastic process $x(n)$ is approximated by a finite sum over the time index n:

$$\langle x(n)\, x^*(n-m)\rangle \approx \frac{1}{N}\sum_{n=0}^{N-1} x(n)\, x^*(n-m). \tag{1.4}$$

The process $x(n)$ is said to be ergodic if the approximation becomes an equality when N approaches infinity. Unfortunately, it is very difficult to show that a process is ergodic. However, computer simulated and experimental results for the stochastic NMR experiments with wide-sense stationary excitations using time averaging show excellent agreement with theory obtained by expectation. This means that the ergodic assumption is not totally unjustified. The choice of N will determine the systematic noise level and it is discussed in chapter 3.

The duration of each RF pulse is assumed to be short compared to the relaxation time constants, T_1 and T_2. This assumption allows the effects of each RF pulse to be represented by a simple multiplication of the magnetization vector with a rotation matrix. This condition is usually satisfied for the observable spins in *in vivo* NMR studies. Also, the RF pulses are assumed to be sufficiently short that off resonance dephase of the magnetization is insignificant during the RF pulses.

Chapter 2

Theoretical Analysis

2.1 Discrete Formulation for Generalized Excitation

Consider the stochastic experiment in Figure 1.3. The sample is excited by an RF pulse every T_R seconds. One signal data point is sampled right after the pulse. With the assumption of isolated spins the analysis need concentrate on only one spin species with relaxation parameters T_1 and T_2 and equilibrium magnetization M_e. Assume that the RF vector lies only in the transverse plane and it is proportional to the excitation sequence $\boldsymbol{\alpha}(n) = [\alpha_x(n),\ \alpha_y(n),\ 0]^T$. Without loss of generality, $\boldsymbol{\alpha}(n)$ will be regarded as the RF vector. The average power of $\boldsymbol{\alpha}(n)$ will be treated as the average RF power. Furthermore, it is assumed to be an ergodic and wide-sense stationary stochastic sequence with mean $\boldsymbol{\mu}_\alpha = [\mu_x, \mu_y, 0]^T$ and auto-covariance

$$\langle [\boldsymbol{\alpha}(n) - \boldsymbol{\mu}_\alpha]\,[\boldsymbol{\alpha}(m) - \boldsymbol{\mu}_\alpha]^T \rangle = \boldsymbol{C}_\alpha\, \delta_{nm}, \tag{2.1}$$

where $\boldsymbol{C}_\alpha$ is the covariance matrix of $\boldsymbol{\alpha}(n)$ and δ_{nm} is the Kronecker delta function. The sum of the diagonal elements of $\boldsymbol{C}_\alpha$ is the average random excitation power and is denoted as

$$\alpha^2 = \langle (\alpha_x(n) - \mu_x)^2 + (\alpha_y(n) - \mu_y)^2 \rangle. \tag{2.2}$$

With the right choice of constant of proportionality α can be regarded as the root mean square (RMS) flip angle. The unit of α is radians in all the calculations. However, it is usually referred to in the text in degrees.

Assume that the RF pulse duration is short compared with the relaxation time constants T_1 and T_2. The Bloch equations can now be solved for the magnetization vector as it varies from one RF pulse to the next. The effects of the n^{th} RF pulse can be summarized by a rotation matrix $\boldsymbol{R}_\alpha(n)$ which is a function of $\boldsymbol{\alpha}(n)$. Denote the amount of interpulse dephase of the transverse magnetization as θ. It is determined by resonance offset, chemical shift, field inhomogeneities, applied magnetic field gradient, etc.. For the rest of this analysis we assume that resonance offset is the only source of interpulse dephase. For a spin ν Hz above resonance, θ is then given by

$$\theta = 2\pi\nu T_R \tag{2.3}$$

and the effect of the interpulse dephase is summarized by the matrix

$$\boldsymbol{R}_\theta = \begin{bmatrix} E_2\cos\theta & E_2\sin\theta & 0 \\ -E_2\sin\theta & E_2\cos\theta & 0 \\ 0 & 0 & E_1 \end{bmatrix},$$

where $E_1 = e^{-T_R/T_1}$ and $E_2 = e^{-T_R/T_2}$. The pulse-to-pulse trajectory of the magnetization vector is described by the following stochastic vector difference equation

$$\boldsymbol{M}(n) = \boldsymbol{R}_\alpha(n)\,[\boldsymbol{R}_\theta\,\boldsymbol{M}(n-1) + \boldsymbol{C}], \tag{2.4}$$

where $\boldsymbol{C}$ is a constant vector given by

$$\boldsymbol{C} = \begin{bmatrix} 0 \\ 0 \\ M_e(1-E_1) \end{bmatrix} \tag{2.5}$$

and M_e is the equilibrium magnetization of the sample in the static main field.

The matrix $\boldsymbol{R}_\theta$ has eigenvalues with magnitudes smaller than one. This fact together with Equation 2.1 imply that the mean $\langle \boldsymbol{M}(n) \rangle$ and the covariance $\langle \boldsymbol{M}(n)\,\boldsymbol{M}^T(n) \rangle$ will approach steady state values for large enough n. The magnetization vector $\boldsymbol{M}(n)$

becomes a wide-sense stationary stochastic sequence. In addition, Equations 2.1 and 2.4 imply that $\boldsymbol{R}_\alpha(n)$ and $\boldsymbol{M}(m)$ are uncorrelated for all m less than n. Taking expectation on both sides of Equation 2.4 and rearranging terms gives

$$\boldsymbol{\mu}_M = (\boldsymbol{I} - \boldsymbol{\mu}_R \boldsymbol{R}_\theta)^{-1} \boldsymbol{\mu}_R \boldsymbol{C}, \tag{2.6}$$

where $\boldsymbol{\mu}_M = \langle \boldsymbol{M}(n) \rangle$, $\boldsymbol{\mu}_R = \langle \boldsymbol{R}_\alpha(n) \rangle$ and I is the 3x3 identity matrix.

The first order input-output cross-covariance $k_1(m)$ is an estimate of the free induction decay (FID). It is defined as the cross-covariance of the complex input $\alpha_{xy}(n) = [\alpha_x(n) + i\,\alpha_y(n)]$ with the complex transverse magnetization $M_{xy}(n)$

$$\begin{aligned} k_1(m) &= \frac{1}{\alpha^2} \langle (M_{xy}(n) - \langle M_{xy}(n) \rangle) (\alpha_{xy}(n-m) - \langle \alpha_{xy}(n-m) \rangle)^* \rangle \\ &= \frac{1}{\alpha^2} \boldsymbol{B}^\dagger [\langle \boldsymbol{M}(n)\, \boldsymbol{\alpha}^T(n-m) \rangle - \boldsymbol{\mu}_M\, \boldsymbol{\mu}_\alpha^T]\, \boldsymbol{B}, \end{aligned} \tag{2.7}$$

where $\boldsymbol{B} = [1, \ -i, \ 0]^T$ and the superscript $\dagger$ is the complex conjugate transpose operator. $k_1(m)$ is independent of n because both the input and the output sequences are wide-sense stationary. When m is less than zero, $\boldsymbol{\alpha}(n-m)$ and $\boldsymbol{M}(n)$ are uncorrelated and so $\langle \boldsymbol{M}(n)\, \boldsymbol{\alpha}^T(n-m) \rangle = \langle \boldsymbol{M}(n) \rangle \langle \boldsymbol{\alpha}(n-m) \rangle^T$, i.e., $k_1(m) = 0$. This is expected since the spin system is a causal system. For m bigger than zero, Equation 2.4 gives

$$\begin{aligned} &\langle \boldsymbol{M}(n)\, \boldsymbol{\alpha}^T(n-m) \rangle - \boldsymbol{\mu}_M\, \boldsymbol{\mu}_\alpha^T \\ &= \boldsymbol{\mu}_R \boldsymbol{R}_\theta [\langle \boldsymbol{M}(n-1)\, \boldsymbol{\alpha}^T(n-m) \rangle - \boldsymbol{\mu}_M\, \boldsymbol{\mu}_\alpha^T] \\ &= \boldsymbol{\mu}_R \boldsymbol{R}_\theta [\langle \boldsymbol{M}(n-1)\, \boldsymbol{\alpha}^T((n-1)-(m-1)) \rangle - \boldsymbol{\mu}_M\, \boldsymbol{\mu}_\alpha^T] \\ &= \boldsymbol{\mu}_R \boldsymbol{R}_\theta [\langle \boldsymbol{M}(n)\, \boldsymbol{\alpha}^T(n-(m-1)) \rangle - \boldsymbol{\mu}_M\, \boldsymbol{\mu}_\alpha^T], \end{aligned} \tag{2.8}$$

where we have used the fact that $\langle \boldsymbol{M}(n)\, \boldsymbol{\alpha}^T(n-m) \rangle$ is wide-sense stationary. This is now an ordinary deterministic difference equation for $\langle \boldsymbol{M}(n)\, \boldsymbol{\alpha}^T(n-m) \rangle - \boldsymbol{\mu}_M\, \boldsymbol{\mu}_\alpha^T$ with index m. The solution is

$$\langle \boldsymbol{M}(n)\, \boldsymbol{\alpha}^T(n-m) \rangle - \boldsymbol{\mu}_M\, \boldsymbol{\mu}_\alpha^T = (\boldsymbol{\mu}_R \boldsymbol{R}_\theta)^m [\langle \boldsymbol{M}(n)\, \boldsymbol{\alpha}^T(n) \rangle - \boldsymbol{\mu}_M\, \boldsymbol{\mu}_\alpha^T]. \tag{2.9}$$

Necessarily, Equation 2.9 reduces to an identity when $m = 0$. Combining Equations 2.7 and 2.9 gives

$$k_1(m) = \frac{1}{\alpha^2}\, \boldsymbol{B}^\dagger\, (\boldsymbol{\mu}_R\, \boldsymbol{R}_\theta)^m\, \boldsymbol{A}\, \boldsymbol{B}, \tag{2.10}$$

where

$$\boldsymbol{A} = \langle \boldsymbol{M}(n)\, \boldsymbol{\alpha}^T(n) \rangle - \boldsymbol{\mu}_M\, \boldsymbol{\mu}_\alpha^T. \tag{2.11}$$

The $\mathcal{Z}$-transform of $k_1(m)$ is defined as

$$\mathcal{Z}\{k_1\}(z) = \sum_{m=0}^{\infty} k_1(m)\, z^{-m}. \tag{2.12}$$

The summation is not performed over negative m since $k_1(m)$ is zero for negative m. The product $\boldsymbol{R}_\alpha(n)\, \boldsymbol{R}_\theta$ represents rotations and relaxation of the magnetization vector so its eigenvalues are less than one and $(\boldsymbol{\mu}_R\, \boldsymbol{R}_\theta)^m$ approaches zero as m approaches infinity. Substituting $k_1(m)$ from Equation 2.10 into Equation 2.12, the $\mathcal{Z}$-transform of $k_1(m)$ is given by

$$\begin{aligned} \mathcal{Z}\{k_1\}(z) &= \frac{1}{\alpha^2} \boldsymbol{B}^\dagger \sum_{m=0}^{\infty} (\boldsymbol{\mu}_R \boldsymbol{R}_\theta)^m z^{-m}\, \boldsymbol{A}\, \boldsymbol{B} \\ &= \frac{1}{\alpha^2} \boldsymbol{B}^\dagger\, (\boldsymbol{I} - \boldsymbol{\mu}_R\, \boldsymbol{R}_\theta\, z^{-1})^{-1}\, \boldsymbol{A}\, \boldsymbol{B}. \end{aligned} \tag{2.13}$$

An estimate of the spectrum is given by the inverse Fourier transform of $k_1(m)$, which can be obtained by evaluating the $\mathcal{Z}$-transform of $k_1(m)$ on the unit circle of the complex $\mathcal{Z}$-plane:

$$K_1(n) = \mathcal{Z}\{k_1\}(e^{-i2n\pi/L}) \tag{2.14}$$

where L is the total number of data points in the spectrum. $L = 2\pi/\Delta\omega$. One complex data point is sampled every T_R seconds, therefore, the maximum bandwidth that can be resolved is $2\pi/T_R$ Hz and so the spectral resolution is

$$\Delta\omega = \frac{2\pi}{T_R L}. \tag{2.15}$$

This implies that if S/N ratio is allowable, we can obtain arbitrarily fine resolution by picking arbitrarily large L. The L points of the reconstructed spectrum will cover the frequency domain from -$1/2T_R$ Hz to $1/2T_R$ Hz. In order to make the analysis independent of L, define a continuous frequency variable $\omega = n\Delta\omega$ so that Equation 2.14 can be rewritten as

$$K_1(\omega) = \frac{1}{\alpha^2} \boldsymbol{B}^\dagger \left(\boldsymbol{I} - \boldsymbol{\mu}_R \boldsymbol{R}_\theta \, e^{i\omega T_R}\right)^{-1} \boldsymbol{A}\, \boldsymbol{B}. \tag{2.16}$$

This is the description of the reconstructed spectrum for a general excitation sequence $\boldsymbol{\alpha}(n)$.

The average signal power is defined as

$$\begin{aligned} P &= \langle M_x^2(n) + M_y^2(n) \rangle \\ &= \boldsymbol{B}^\dagger \langle \boldsymbol{M}(n)\, \boldsymbol{M}^T(n) \rangle \, \boldsymbol{B} \\ &= \boldsymbol{B}^\dagger \langle \boldsymbol{M}\, \boldsymbol{M}^T \rangle \, \boldsymbol{B}. \end{aligned} \tag{2.17}$$

The signal correlation matrix, $\langle \boldsymbol{M}\, \boldsymbol{M}^T \rangle$, is independent of n because $\boldsymbol{M}(n)$ is wide-sense stationary. From Equation 2.4 $\langle \boldsymbol{M}\, \boldsymbol{M}^T \rangle$ is given by the solution of the matrix equation

$$\begin{aligned} \langle \boldsymbol{M}\, \boldsymbol{M}^T \rangle &= \langle \boldsymbol{R}_\alpha(n)\, \boldsymbol{R}_\theta \langle \boldsymbol{M}\, \boldsymbol{M}^T \rangle \, \boldsymbol{R}_\theta^T \, \boldsymbol{R}_\alpha^T(n) \rangle + \langle \boldsymbol{R}_\alpha(n)\, \boldsymbol{R}_\theta \, \boldsymbol{\mu}_M \, \boldsymbol{C}^T \, \boldsymbol{R}_\alpha^T(n) \rangle \\ &\quad + \langle \boldsymbol{R}_\alpha(n)\, \boldsymbol{C}\, \boldsymbol{\mu}_M^T \, \boldsymbol{R}_\theta^T \, \boldsymbol{R}_\alpha^T(n) \rangle + \langle \boldsymbol{R}_\alpha(n)\, \boldsymbol{C}\, \boldsymbol{C}^T \, \boldsymbol{R}_\alpha^T(n) \rangle, \end{aligned} \tag{2.18}$$

which is a set of six simultaneous equations with six unknowns.

The covariance of the complex signal M_{xy} is defined as

$$\begin{aligned} r(m) &= \langle [M_{xy}(n) - \langle M_{xy}(n) \rangle] \, [M_{xy}(n-m) - \langle M_{xy}(n-m) \rangle]^* \rangle \\ &= \boldsymbol{B}^\dagger \left[\langle \boldsymbol{M}(n)\, \boldsymbol{M}^T(n-m) \rangle - \boldsymbol{\mu}_M \, \boldsymbol{\mu}_M^T \right] \boldsymbol{B}. \end{aligned} \tag{2.19}$$

For $m \geq 0$, multiplying both sides of equation Equation 2.4 with $\boldsymbol{M}^T(n-m)$, taking expectation and then subtracting away $\boldsymbol{\mu}_M \, \boldsymbol{\mu}_M^T$ gives

$$\langle \boldsymbol{M}(n) \boldsymbol{M}^T(n-m) \rangle - \boldsymbol{\mu}_M \, \boldsymbol{\mu}_M^T$$

$$
\begin{aligned}
&= \boldsymbol{\mu}_R \boldsymbol{R}_\theta [\langle \boldsymbol{M}(n-1)\, \boldsymbol{M}^T(n-m)\rangle - \boldsymbol{\mu}_M\, \boldsymbol{\mu}_\alpha^T] \\
&= \boldsymbol{\mu}_R \boldsymbol{R}_\theta [\langle \boldsymbol{M}(n-1)\, \boldsymbol{M}^T((n-1)-(m-1))\rangle - \boldsymbol{\mu}_M\, \boldsymbol{\mu}_\alpha^T] \\
&= \boldsymbol{\mu}_R \boldsymbol{R}_\theta [\langle \boldsymbol{M}(n)\, \boldsymbol{M}^T(n-(m-1))\rangle - \boldsymbol{\mu}_M\, \boldsymbol{\mu}_\alpha^T]. \qquad (2.20)
\end{aligned}
$$

Once again, an ordinary deterministic difference equation is obtained. The solution is

$$
\langle \boldsymbol{M}(n)\boldsymbol{M}^T(n-m)\rangle - \boldsymbol{\mu}_M\, \boldsymbol{\mu}_M^T = (\boldsymbol{\mu}_R \boldsymbol{R}_\theta)^m [\langle \boldsymbol{M}\, \boldsymbol{M}^T\rangle - \boldsymbol{\mu}_M\, \boldsymbol{\mu}_M^T]. \qquad (2.21)
$$

Similarly, for $m \leq 0$,

$$
\langle \boldsymbol{M}(n)\boldsymbol{M}^T(n-m)\rangle - \boldsymbol{\mu}_M\, \boldsymbol{\mu}_M^T = [\langle \boldsymbol{M}\, \boldsymbol{M}^T\rangle - \boldsymbol{\mu}_M\, \boldsymbol{\mu}_M^T](\boldsymbol{\mu}_R^T \boldsymbol{R}_\theta^T)^{-m}. \qquad (2.22)
$$

The $\mathcal{Z}$-transform of $r(m)$ is then given by

$$
\begin{aligned}
\mathcal{Z}\{r\}(z) &= \sum_{m=-\infty}^{\infty} r(m)\, z^{-m} \\
&= \boldsymbol{B}^\dagger [(\boldsymbol{I} - \boldsymbol{\mu}_R \boldsymbol{R}_\theta\, z^{-1})^{-1} (\langle \boldsymbol{M}\, \boldsymbol{M}^T\rangle - \boldsymbol{\mu}_M\, \boldsymbol{\mu}_M^T) \\
&\quad + (\langle \boldsymbol{M}\, \boldsymbol{M}^T\rangle - \boldsymbol{\mu}_M\, \boldsymbol{\mu}_M^T)(\boldsymbol{I} - \boldsymbol{\mu}_R^T \boldsymbol{R}_\theta^T\, z)^{-1} \\
&\quad - (\langle \boldsymbol{M}\, \boldsymbol{M}^T\rangle - \boldsymbol{\mu}_M\, \boldsymbol{\mu}_M^T)]\, \boldsymbol{B}. \qquad (2.23)
\end{aligned}
$$

The power spectrum is the $\mathcal{Z}$-transform of $r(m)$ evaluated on the unit circle of the complex $\mathcal{Z}$-plane:

$$
\begin{aligned}
S(\omega) &= \mathcal{Z}\{r\}(e^{-i\omega T_R}) \\
&= \boldsymbol{B}^\dagger [(\boldsymbol{I} - \boldsymbol{\mu}_R \boldsymbol{R}_\theta\, e^{i\omega T_R})^{-1} (\langle \boldsymbol{M}\, \boldsymbol{M}^T\rangle - \boldsymbol{\mu}_M\, \boldsymbol{\mu}_M^T) \\
&\quad + (\langle \boldsymbol{M}\, \boldsymbol{M}^T\rangle - \boldsymbol{\mu}_M\, \boldsymbol{\mu}_M^T)(\boldsymbol{I} - \boldsymbol{\mu}_R^T \boldsymbol{R}_\theta^T\, e^{-i\omega T_R})^{-1} \\
&\quad - (\langle \boldsymbol{M}\, \boldsymbol{M}^T\rangle - \boldsymbol{\mu}_M\, \boldsymbol{\mu}_M^T)]\, \boldsymbol{B}. \qquad (2.24)
\end{aligned}
$$

2.2 Random Flip Angle Excitation

In this section, we assume that the RF excitation vector lies only along the x-axis of the rotating frame (Figure 1.4a). The excitation vector $\boldsymbol{\alpha}(n)$ has only one non-zero component, $\alpha_x(n)$, satisfying the following two conditions:

1. From Equations 2.1 and 2.2, $\alpha_x(n)$ represents the random flip angles of the RF pulses with a mean square value of α^2 and

$$\langle [\alpha_x(n) - \mu_x][\alpha_x(m) - \mu_x] \rangle = \alpha^2 \delta_{nm}.$$

2. $\alpha_x(n)$ has an even probability density function, i.e., positive and negative flip angles are equally likely. This implies that the mean of $\alpha_x(n)$, μ_x, is zero. The effects of excitations with non-zero mean will be investigated in a later section.

The matrix $\boldsymbol{R}_\alpha(n)$ is simply

$$\boldsymbol{R}_\alpha(n) = \begin{bmatrix} 1 & 0 & 0 \\ 0 & \cos\alpha_x(n) & \sin\alpha_x(n) \\ 0 & -\sin\alpha_x(n) & \cos\alpha_x(n) \end{bmatrix},$$

which represents a rotation of the magnetization vector about the x-axis of the rotating frame for $\alpha_x(n)$ degrees. The probability density function of $\alpha_x(n)$ is assumed to be even, so $\langle \sin\alpha_x(n) \rangle = 0$ and $\langle \cos\alpha_x(n) \rangle = \varphi_\alpha(1)$ where $\varphi_\alpha(t) = \langle e^{i\alpha_x(n)t} \rangle$ is the characteristic function of the random variable $\alpha_x(n)$. The characteristic function of a Gaussian white noise satisfying the above conditions is $\varphi_\alpha(t) = e^{-\alpha^2 t^2/2}$. A random binary sequence taking on two values, α and $-\alpha$, each with probability 1/2 will also satisfy the above conditions. Its characteristic function is $\varphi_\alpha(t) = \cos(\alpha t)$.

The mean of the rotation matrix $\boldsymbol{R}_\alpha(n)$ is

$$\boldsymbol{\mu}_R = \begin{bmatrix} 1 & 0 & 0 \\ 0 & \varphi_\alpha(1) & 0 \\ 0 & 0 & \varphi_\alpha(1) \end{bmatrix}. \tag{2.25}$$

Equation 2.6 gives the mean magnetization vector

$$\boldsymbol{\mu}_M = \frac{M_e(1 - E_1)\varphi_\alpha(1)}{1 - E_1\varphi_\alpha(1)} \begin{bmatrix} 0 \\ 0 \\ 1 \end{bmatrix}. \tag{2.26}$$

The matrix $\boldsymbol{A}$ from Equation 2.11 is

$$\boldsymbol{A} = \frac{-M_e(1-E_1)\,\dot{\varphi}_\alpha(1)}{1-E_1\,\varphi_\alpha(1)} \begin{bmatrix} 0 & 0 & 0 \\ 1 & 0 & 0 \\ 0 & 0 & 0 \end{bmatrix}, \tag{2.27}$$

where $\dot{\varphi}_\alpha(1)$ is the first derivative of $\varphi_\alpha(t)$ evaluated at $t = 1$. Equation 2.16 can now be evaluated to give an estimate of the spectrum

$$K_1(\omega) = \frac{-i\,M_e(1-E_1)\dot{\varphi}_\alpha(1)}{\alpha^2[1-E_1\,\varphi_\alpha(1)]} \frac{1-E_2\,e^{i(\theta+\omega T_R)}}{D(\omega)} \tag{2.28}$$

where

$$D(\omega) = 1 - E_2\cos\theta\,[1+\varphi_\alpha(1)]\,e^{i\omega T_R} + E_2^2\,\varphi_\alpha(1)\,e^{2i\omega T_R}.$$

The first part of the right side of Equation 2.28 is dependent on T_1 and the excitation power but independent of ω and T_2. Define the second part as

$$F(\omega) = \frac{1-E_2\,e^{i(\theta+\omega T_R)}}{D(\omega)}. \tag{2.29}$$

$F(\omega)$ has only T_2 dependence but no T_1 dependence. The function $F(\omega)$ is periodic with a period of $2\pi/T_R$ rad/sec, or $1/T_R$ Hz. Integrating $F(\omega)$ over one period gives $2\pi/T_R$ which is independent of T_2 and the excitation power. Therefore, the integrated line intensity is purely determined by T_1, T_R and the excitation power. The line shape is determined only by T_2, T_R, θ and the excitation power. In conventional FT-NMR with T_R comparable to T_1, the integrated spectral intensity is also determined by T_1, T_R and the excitation power, but the line shape is independent of θ, i.e., independent of resonance offset. Figure 2.1a shows the line shape (the absorption part) of $K_1(\omega)$ for Gaussian white noise excitations with different RMS flip angles, i.e. with different excitation power. Figure 2.1b is a plot of the corresponding integrated spectral intensity as a function of the RMS flip angle. The plot is normalized by the integrated spectral intensity at $\alpha = 0°$. This is made possible by the fact that $K_1(\omega)$ is well defined even when $\alpha = 0°$. Figure 2.2 shows the shape of lines at different resonance offset frequencies. These plots show the following saturation characteristics:

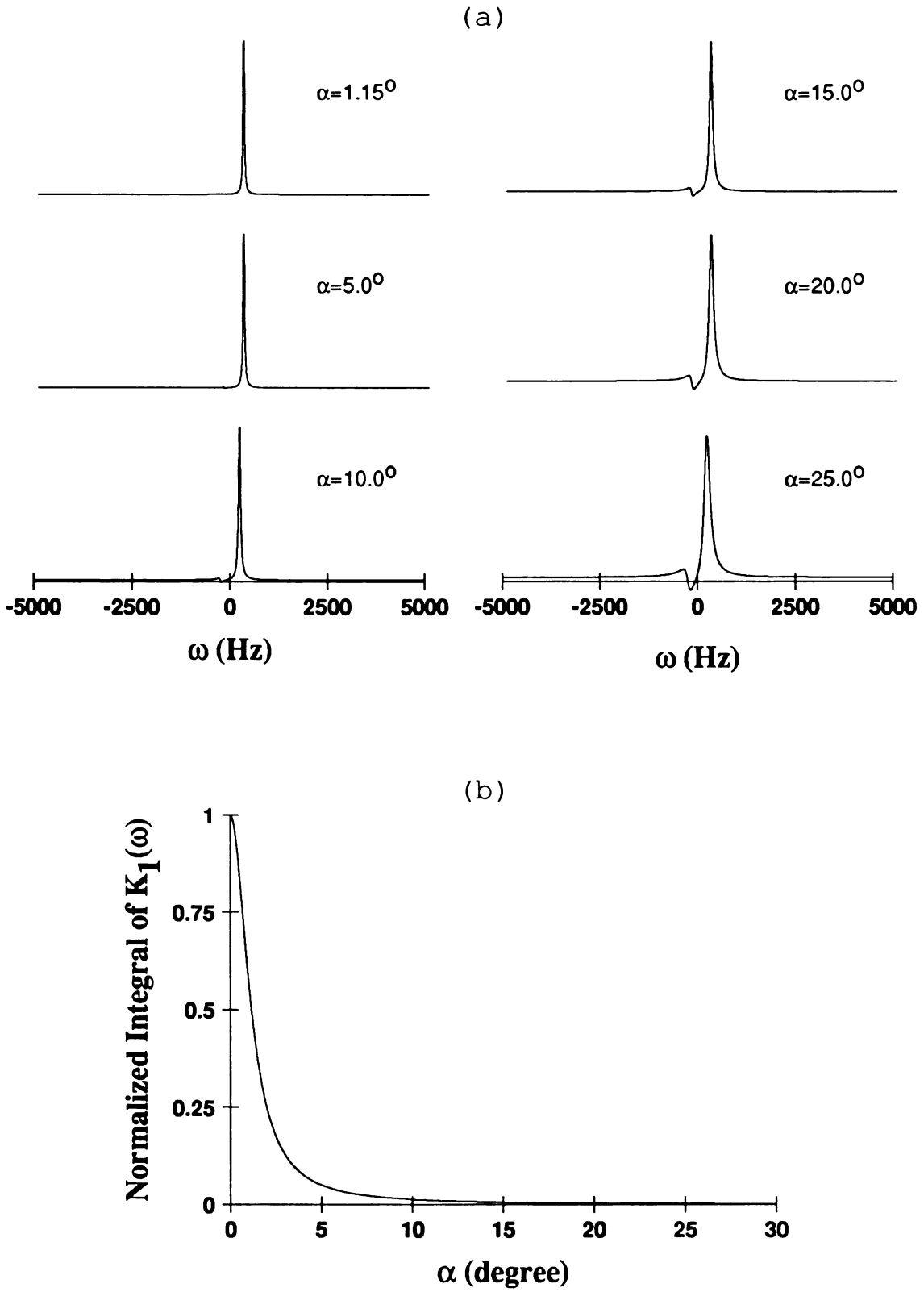

Figure 2.1: $K_1(\omega)$ for random flip angle excitation with Gaussian white noise. (a) Line shape (absorption part) and (b) integrated line intensity normalized by the value at $\alpha = 0°$. $T_1 = 0.5$s, $T_2 = 10$ms, $T_R = 0.1$ms and $\nu = 250$Hz.

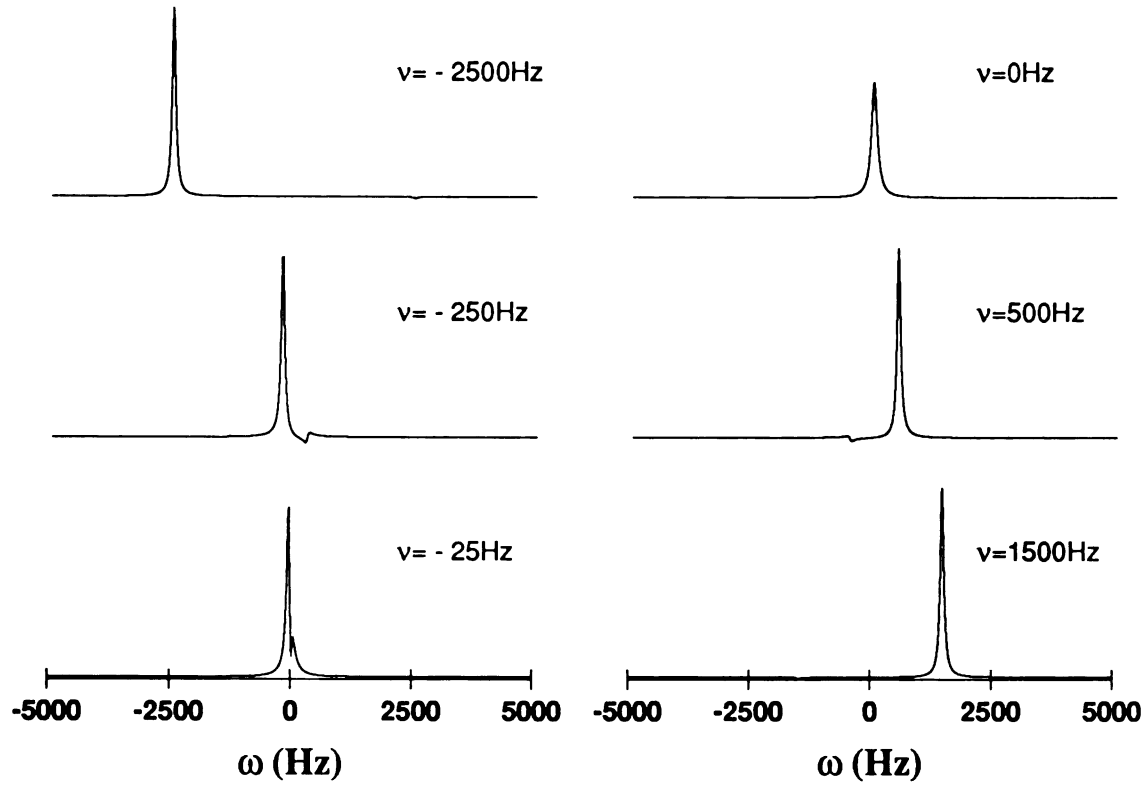

Figure 2.2: Line shape of $K_1(\omega)$ with different resonance offset frequencies. The excitation is Gaussian white noise random flip angle excitation with $\alpha = 15°$. $T_1 = 0.5$s, $T_2 = 10$ms and $T_R = 0.1$ms. All the plots are on the same vertical scale.

- At low excitation power the line shape resembles a Lorentzian line.
- Line width (measured at half height) increases as the excitation power is increased.
- Line distortion appears at the negative of the resonance offset frequency as the excitation power is increased.
- Integrated line intensity decreases rapidly as the excitation power is increased.
- The line response across the spectrum is non-uniform. A line at resonance has a width at half height different from those for lines off resonance.

To understand the saturation characteristics, consider the line shape function $F(\omega)$ defined in Equation 2.29. For both the Gaussian white noise sequence and the random

binary sequence, $\varphi_\alpha(1)$ approaches unity as the excitation power α^2 approaches zero. $F(\omega)$ then reduces to

$$F(\omega) = \frac{1}{1 - E_2\, e^{i(\omega T_R - \theta)}} \tag{2.30}$$

which is roughly a Lorentzian line with line width $1/\pi T_2$ Hz. A Lorentzian line with the same line width is

$$\frac{1}{1 - i(\omega - \theta/T_R)T_2}.$$

Figure 2.3 shows that the only difference between $F(\omega)$ and the Lorentzian line is a slightly larger baseline in $F(\omega)$. The larger baseline is a consequence of aliasing due to under sampling. The narrower $F(\omega)$ is relative to the total bandwidth $1/T_R$, the smaller the baseline would be. This is usually the case in spectroscopy. Therefore, any line in the form of $F(\omega)$ will be referred to as a Lorentzian line in this dissertation. With the assumption that the interpulse dephase is only caused by the resonance offset, $\theta = 2\pi\nu T_R$, the line is centered at ν Hz. The reconstructed spectrum at low excitation power, e.g. the line with $\alpha = 1.15°$ in Figure 2.1, resembles the one obtained by a conventional FT-NMR.

As the excitation power is increased, $\varphi_\alpha(1)$ decreases from unity. The line shape becomes dependent on the the resonance offset, ν. Figure 2.2 shows the shape of the absorption part of $K_1(\omega)$ for lines at different resonance offsets. When the line is at resonance, i.e. $\theta = 0$, $F(\omega)$ reduces to

$$F(\omega) = \frac{1}{1 - E_2\, \varphi_\alpha(1)\, e^{i\omega T_R}} \tag{2.31}$$

which is also a Lorentzian line centered at the origin. The line width in Hertz is now increased to

$$\frac{1}{\pi T_2} - \frac{1}{\pi T_R} \log \varphi_\alpha(1). \tag{2.32}$$

For lines not at resonance, $F(\omega)$ cannot be simplified. At $\omega = -\theta/T_R$, the numerator of $F(\omega)$ reduces to $(1 - E_2)$. In general T_R is much smaller than T_2, as a result E_2 is very close to unity and $F(\omega)$ vanishes at $\omega = -\theta/T_R$, the negative of the resonance offset.

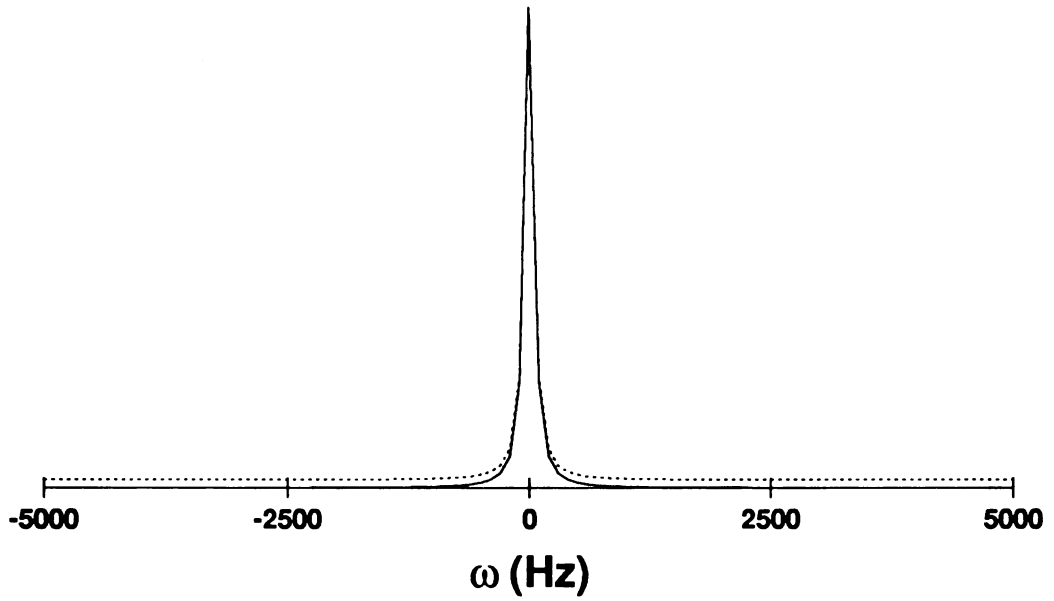

Figure 2.3: A comparison of the line shape of $(1 - E_2 e^{i\omega T_R})^{-1}$ (dotted line) with a Lorentzian line with the same line width (solid line).

This creates a notch artifact for lines with a resonance offset which is small relative to the line width (Figure 2.2). When the resonance offset is large relative to the line width and such that

$$\cos\theta < \frac{2\sqrt{\varphi_\alpha(1)}}{1+\varphi_\alpha(1)}, \tag{2.33}$$

the notch artifact becomes less significant. However, the line shape is now given by

$$F(\omega) \propto \frac{1}{1 - E_2\sqrt{\varphi_\alpha(1)}\, e^{i(\omega T_R - \theta')}} \tag{2.34}$$

where

$$\theta' = \cos^{-1}\left[\cos\theta \frac{1+\varphi_\alpha(1)}{2\sqrt{\varphi_\alpha(1)}}\right].$$

The line is Lorentzian centered at a new resonance offset $\nu' = \theta'/2\pi T_R$. The line width *in* Hertz is

$$\frac{1}{\pi T_2} - \frac{1}{2\pi T_R}\log\varphi_\alpha(1), \tag{2.35}$$

which means that the line broadening is half that of the line at resonance. Consequently, the line height is about twice that at resonance (Figure 2.2). For Gaussian white noise

excitation and random binary excitation, the function $\varphi_\alpha(1)$ is smaller than unity for $\alpha < 90°$ and is a monotonically decreasing function of α. Equations 2.32 and 2.35 then shows that the line width at half height increases as α is increased, i.e. as the excitation power in increased.

The results above explain the discrepancy between Bartholdi *et al*'s results [10] and Knight & Kaiser's [12] results. Bartholdi *et al* analyzed the experiment with continuous Gaussian white noise excitation. However, they did it only for spins at resonance. They obtained a Lorentzian line with a line broadening of $\sigma^2/2\pi$ Hz, where σ^2 is the excitation power per unit time. In the analysis above, a Gaussian white noise excitation has $\varphi_\alpha(1) = e^{-\alpha^2/2}$. Assume T_R to be very small and define $\sigma^2 = \alpha^2/T_R$. Equation 2.32 then gives the same line broadening for spins at resonance. Knight and Kaiser also did a continuous excitation analysis, but with a totally different approach. They did the analysis in a laboratory frame, where each spin has a resonance offset frequency of its Larmor precession frequency. They obtained a small line shift and a line broadening of $\sigma^2/4\pi$ Hz. For spins off resonance, Equation 2.35 gives the same line broadening and Equation 2.34 also predicts a line shift. The results of the two groups of researchers are different halves of the complete solution.

For the analysis of the average signal power write $\langle \boldsymbol{M}\, \boldsymbol{M}^T \rangle$ as

$$\langle \boldsymbol{M}\, \boldsymbol{M}^T \rangle = \begin{bmatrix} r_{xx} & r_{xy} & r_{xz} \\ r_{xy} & r_{yy} & r_{yz} \\ r_{xz} & r_{yz} & r_{zz} \end{bmatrix}.$$

The individual components are obtained by solving Equation 2.18:

$$r_{xx} = M_e^2(1-E_1)^2 \frac{1+E_1\varphi_\alpha(1)}{1-E_1\varphi_\alpha(1)} \frac{E_2^2 \sin^2\theta(1-\varphi_\alpha(2))(1+E_2^2\varphi_\alpha(1))}{2Q}, \quad (2.36)$$

$$r_{xy} = M_e^2(1-E_1)^2 \frac{1+E_1\varphi_\alpha(1)}{1-E_1\varphi_\alpha(1)} \frac{E_2^2(1-E_2^2)\sin\theta\cos\theta\,\varphi_\alpha(1)(1-\varphi_\alpha(2))}{2Q} \quad (2.37)$$

$$r_{yy} = M_e^2(1-E_1)^2 \frac{1+E_1\varphi_\alpha(1)}{1-E_1\varphi_\alpha(1)}$$

$$\times \frac{(1-\varphi_\alpha(2))(1-E_2^2\cos^2\theta - E_2^2\cos 2\theta\,\varphi_\alpha(1) + E_2^4\cos^2\theta\,\varphi_\alpha(1))}{2Q} \tag{2.38}$$

and

$$r_{xz} = r_{yz} = 0 \tag{2.39}$$

where

$$\begin{aligned} Q &= (1-E_2^2)(1-E_2^2\cos 2\theta\,\varphi_\alpha(1))[1-\frac{1}{2}(E_1^2+E_2^2)(1+\varphi_\alpha(2)) + E_1^2E_2^2\,\varphi_\alpha(2)] \\ &\quad +2E_2^2(1-E_2^2)\sin^2\theta(1+E_2^2\,\varphi_\alpha(1))[\frac{1}{2}(1+\varphi_\alpha(2)) - E_1^2\,\varphi_\alpha(2)] \\ &\quad +\frac{1}{2}E_2^2(1-E_1^2)\sin^2\theta(1-\varphi_\alpha(2))(1+E_2^2\,\varphi_\alpha(1)). \end{aligned} \tag{2.40}$$

The expression for r_{zz} is not shown since it is not required for later analysis. The average signal power is given by $P = r_{xx} + r_{yy}$.

Figure 2.4a is a plot of the average signal power as a function of the RMS flip angle α of a Gaussian white noise excitation. It has a peak at 1.15°. This means that the S/N ratio is at a maximum when the excitation sequence has a RMS flip angle of 1.15°. Notice that the S/N ratio is independent of the spectral resolution, as pointed out in the introduction. Denote the RMS flip angle that gives the maximum S/N ratio as α_{max}. Figure 2.4b shows that α_{max} is approximately the Ernst angle, $\cos^{-1}(e^{-T_R/T_1})$. The Ernst angle is the flip angle that gives the maximum signal in a conventional FT-NMR experiment that consists of one RF excitation every T_R seconds. The peak RF power is proportional to the square of the RF field strength, i.e., square of the flip angle. A conventional FT-NMR experiment with $T_R = 100$ms will have an Ernst angle of 35° for the same spin system. Therefore, the peak power required for the stochastic experiment is roughly three orders of magnitude smaller than that for the conventional FT-NMR experiment.

In many cases T_R is much shorter than T_1, so α_{max} will be less than 10° and $\varphi_\alpha(1)$ very close to unity. The notch artifact is usually insignificant at this low level of excitation. However, for T_2 large such that the natural line width, $1/\pi T_2$, is small compared with the line broadening, $\log\varphi_\alpha(1)/\pi T_R$, at $\alpha = \alpha_{max}$, the difference in line broadening

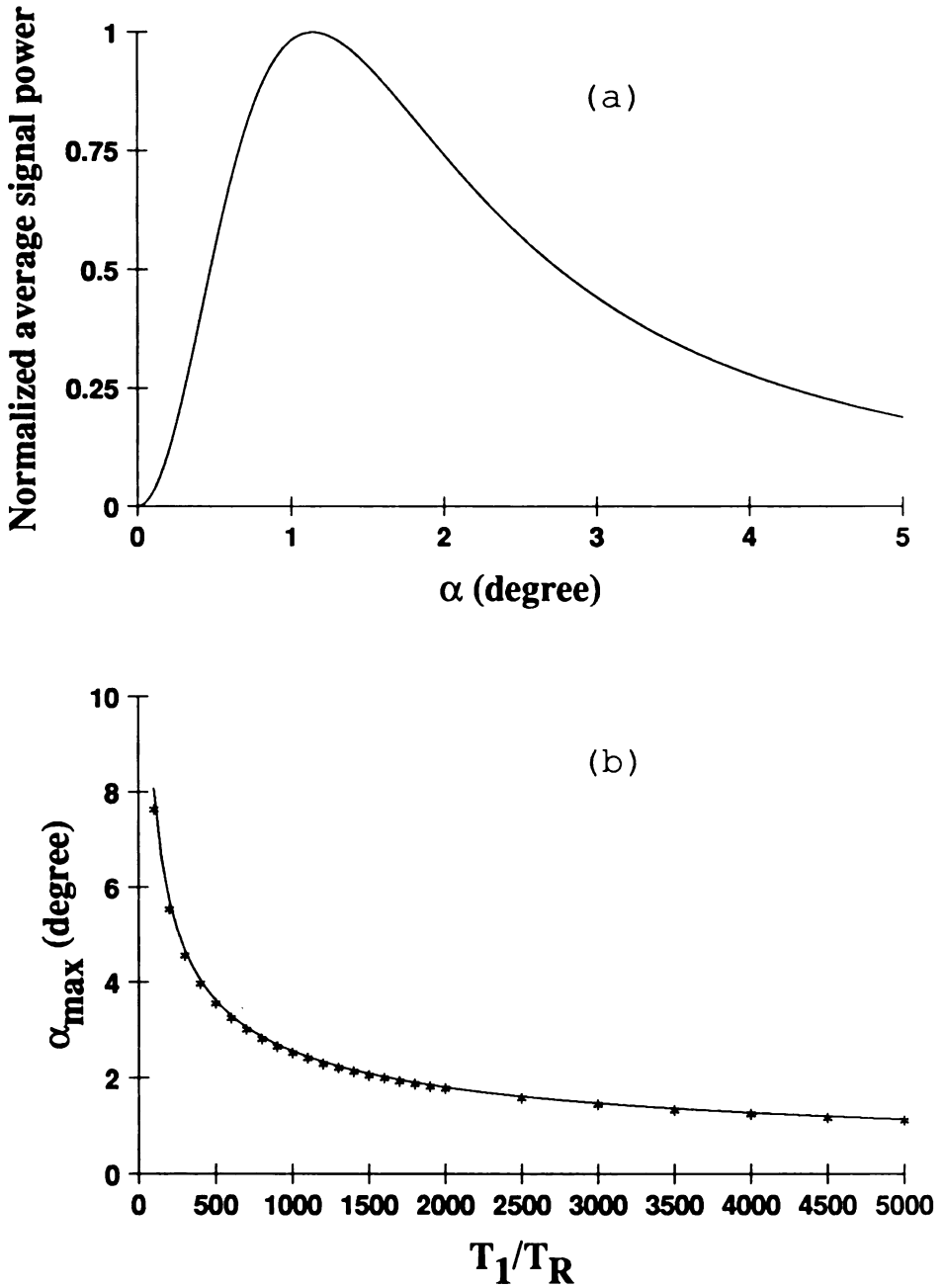

Figure 2.4: Random flip angle excitation with Gaussian white noise. (a) Average signal power versus the RMS flip angle. (b) α_{max} versus T_1/T_R. The symbol * represents theoretical values and the solid line is $\cos^{-1}(e^{-T_R/T_1})$. $T_1 = 0.5$sec, $T_2 = 10$ms, $T_R = 0.1$ms and $\nu = 250$Hz.

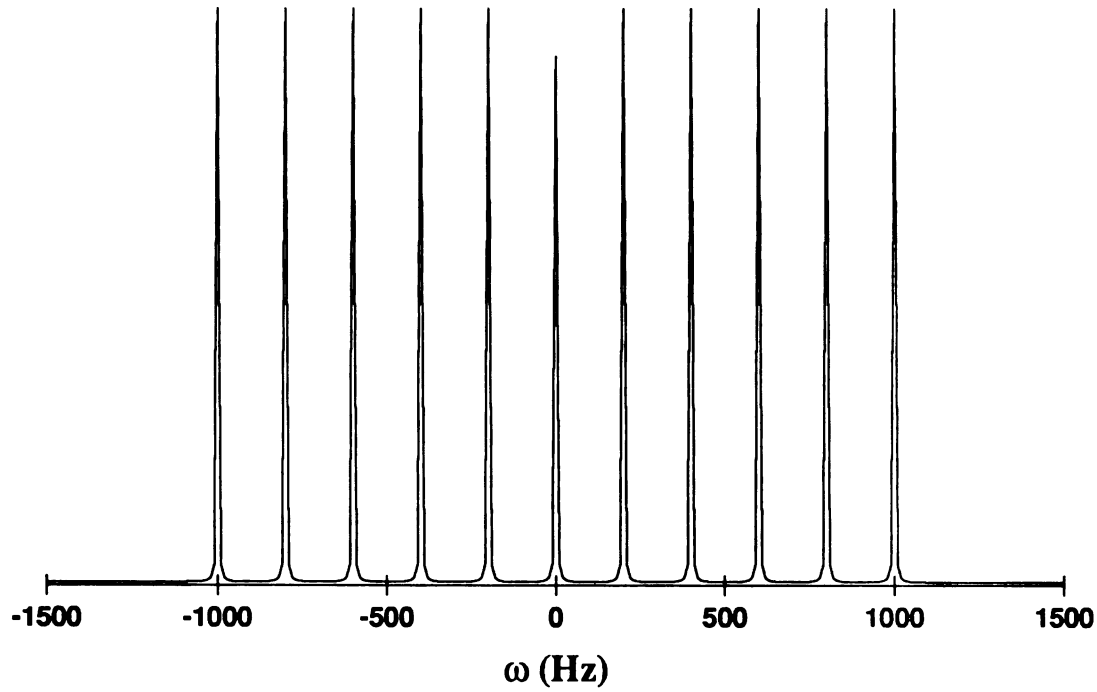

Figure 2.5: Non-uniform response of $K_1(\omega)$ across the spectrum for Gaussian white noise random flip angle excitation. Eleven spins equally spaced across the spectrum. $T_1 = 0.5$sec, $T_2 = 100$ms, $T_R = 0.1$ms and $\alpha = \alpha_{max} = 1.15°$.

between on resonance and off resonance lines may still be large. This is demonstrated in Figure 2.5. To minimize this non-uniform response, the excitation level must be dropped below α_{max}. This results in a loss of S/N ratio.

To evaluate the signal power spectrum as an estimate of the spectrum Equations 2.23 and 2.24 are made specific for random flip angle excitation to give

$$S(\omega) = \frac{P - E_2 e^{i(\theta+\omega T_R)}[r_{xx}\varphi_\alpha(1) + r_{yy} + ir_{xy}(1-\varphi_\alpha(1))]}{D(\omega)} + \frac{P - E_2 e^{-i(\theta+\omega T_R)}[r_{xx}\varphi_\alpha(1) + r_{yy} - ir_{xy}(1-\varphi_\alpha(1))]}{D(\omega)^*} - P. \quad (2.41)$$

The power spectrum shown in Figure 2.6a closely resembles the absorption part of $K_1(\omega)$ (Figure 2.1a) at low excitation power. At higher excitation power, it has much less notch artifact. An advantage of using the spectral density as an estimate of the real spectrum is that it is calculated from the signal sequence only, so that the excitation se-

quence $\alpha(n)$ need not be stored or regenerated. However, as shown in Figure 2.6b, the response is still non-uniform across the spectrum. It will be shown in later section that the non-uniform response can be eliminated with a better excitation scheme.

So far only results for Gaussian white noise excitations have been considered. The dependence of $K_1(\omega)$, P and $S(\omega)$ on the type of excitation that is used is embedded in $\varphi_\alpha(1)$, $\varphi_\alpha(2)$ and $\dot{\varphi}_\alpha(1)$. Power series expansion shows that the differences in these functions between Gaussian white noise excitation and random binary excitation are

$$\Delta\varphi_\alpha(1) = \frac{\alpha^4}{12}\left(1 - \frac{7\alpha^2}{30} + \cdots\right),$$

$$\Delta\varphi_\alpha(2) = \frac{4\alpha^4}{3}\left(1 - \frac{14\alpha^2}{15} + \cdots\right) \text{ and}$$

$$\Delta\dot{\varphi}_\alpha(1) = \frac{\alpha^4}{3}\left(1 - \frac{7\alpha^2}{20} + \cdots\right)$$

where $\Delta\varphi_\alpha(t) =$ Gaussian $\varphi_\alpha(t) -$ Binary $\varphi_\alpha(t)$. For $\alpha = \alpha_{max} < 0.175$ rad $(= 10°)$ the fractional differences, $\Delta\varphi_\alpha(1)/\varphi_\alpha(1)$, $\Delta\varphi_\alpha(2)/\varphi_\alpha(2)$ and $\Delta\dot{\varphi}_\alpha(1)/\dot{\varphi}_\alpha(1)$, are negligible. This means that the response to Gaussian white noise excitation and random binary excitation will be almost identical. This is desirable since random binary sequence can be approximated by binary maximum length sequences (MLS) which will be discussed in later sections.

2.3 Wiener Series Analysis

The functional relationship between the stimulus and response of a linear system follows the principle of superposition. The response of the linear system to an arbitrary excitation can be reconstructed from the impulse response using the convolution integral (Equation 1.1). However, every physical system is in some sense nonlinear, for which the principle of superposition does not hold. The impulse response of a nonlinear

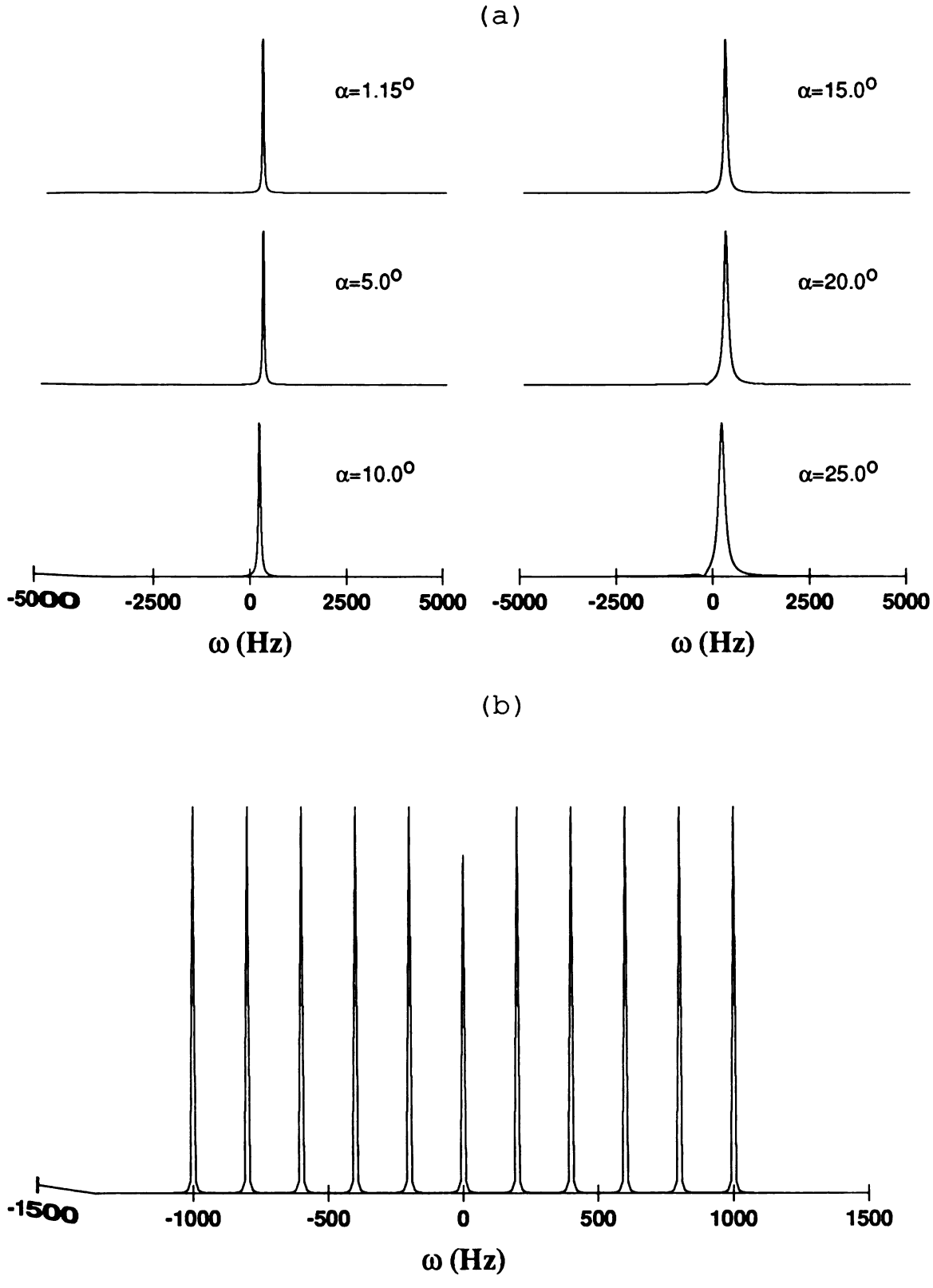

Figure 2.6: Power spectrum $S(\omega)$ for Gaussian white noise random flip angle excitation. $T_1 = 0.5$s and $T_R = 0.1$ms. (a) $S(\omega)$ with different RMS flip angles. $\nu = 250$Hz and $T_2 = 10$ms. (b) $S(\omega)$ for 11 equally spaced spins. $\alpha = 1.15°$ and $T_2 = 100$ms.

system provides little clue to the system response to any excitation other than the impulse. The NMR spin system is a nonlinear system. The Bloch equations are nonlinear with respect to the RF excitation. A single hard pulse excites only the linear component which is the FID. Nonlinear components appear in the magnetization response when the system is excited by more than one pulse in succession or by continuous excitation. The stochastic NMR experiment consists of a train of RF excitation pulses and therefore exhibits nonlinear magnetization response. The nonlinear transverse magnetization response $M_{xy}(n) = M_x(n) + i\, M_y(n)$ can be represented by a Volterra series expansion [7]:

$$M_{xy}(n) = \sum_{j=0}^{\infty} H_j[\alpha_x(n)] \tag{2.42}$$

where $H_0[\alpha_x(n)] = h_0$ is a constant and

$$H_j[\alpha_x(n)] = \sum_{m_1=-\infty}^{\infty} \cdots \sum_{m_j=-\infty}^{\infty} h_j(m_1, \cdots, m_j)\alpha_x(n-m_1)\cdots\alpha_x(n-m_j).$$

The Volterra series is a generalization of the Taylor series of a function of multiple arguments. The functional $H_j[\alpha_x(n)]$ is called the j^{th} order Volterra functional and the function h_j is the j^{th} order Volterra kernel. The H_j term summaries the j^{th} order nonlinearity of the response. It is a j^{th} order convolution of the input with the j^{th} order Volterra kernel. The linear kernel, $h_1(m)$, is the FID obtained by a single pulse FT-NMR experiment. However, there is no easy way to estimate the Volterra kernels from the signals obtained by the stochastic experiment, not even for $h_1(m)$. Blümich and Ziessow [13,14] used a heuristic ansatz for the Volterra kernels to describe the noise-like spectral distortion resulting from a binary MLS excitation. They attributed this distortion to linear Hadamard processing of the nonlinear spin response. In the following discussion, we will show that the spectral distortion in $K_1(\omega)$ is also due to a linear processing of the nonlinear magnetization response.

As mentioned above, the impulse response of a nonlinear system provides little clue to the system response to any other type of excitation. It appears that the only way to

characterize the stochastic experiment is to study the nonlinear magnetization response for a great variety of deterministic excitation sequences. This can be accomplished efficiently by a Gaussian white noise sequence since, given enough time, there is a finite probability that any given deterministic excitation sequence can be represented arbitrarily closely by some sample of the white noise sequence. Therefore, the spin system is subjected to infinite possible deterministic excitations. This is the basic principle of Wiener series analysis [7]. For the following analysis assume random flip angle excitation by Gaussian white noise as discussed in the previous section. The Wiener series expansion of the magnetization response is defined as

$$M_{xy}(n) = \sum_{j=0}^{\infty} G_j[k_j; \alpha_x(n)] \tag{2.43}$$

where $G_j[k_j; \alpha_x(n)]$ is the j^{th} order Wiener functional and k_j is the j^{th} order Wiener kernel. The difference between the Volterra series expansion and the Wiener series expansion is that the set of Wiener functionals $\{G_j\}$ is required to be a complete set of orthogonal functionals in the sense that

$$\langle G_j[k_j; \alpha_x(n)]\, H_m[\alpha_x(n)] \rangle = 0 \tag{2.44}$$

for any Volterra functional $H_m[\alpha_x(n)]$ of order $m < j$, while the set of Volterra functionals $\{H_j\}$ is not. The j^{th} order Wiener functional is also required to be a Volterra series with the highest order of nonlinearity being the j^{th} order, i.e. $G_j[k_j; \alpha_x(n)]$ can be written as

$$\begin{aligned} G_j[k_j; \alpha_x(n)] = & \sum_{m_1=-\infty}^{\infty} \cdots \sum_{m_j=-\infty}^{\infty} k_j(m_1, \cdots, m_j)\alpha_x(n-m_1)\cdots\alpha_x(n-m_j) \\ & + \sum_{l=0}^{j-1} \left[\sum_{m_1=-\infty}^{\infty} \cdots \sum_{m_l=-\infty}^{\infty} k_{l(j)}(m_1, \cdots, m_l)\alpha_x(n-m_1)\cdots\alpha_x(n-m_l) \right], \end{aligned} \tag{2.45}$$

where $k_{l(j)}$ is called a derived Wiener kernel because the orthogonality requirement forces it to be zero when $(j-l)$ is odd and

$$k_{j-2m(j)}(m_1, \cdots, m_{j-2m}) = \frac{(-1)^m j! \alpha^{2m}}{(j-2m)! m! 2^m}$$

$$\sum_{n_1=-\infty}^{\infty} \cdots \sum_{n_m=-\infty}^{\infty} k_j(n_1, n_1, \cdots, n_m, n_m, m_1, \ldots, m_{j-2m}) \tag{2.46}$$

when $j - l = 2m$. The orthogonality requirement then allows the Wiener kernels to be calculated by multi-dimensional input-output cross-correlation

$$k_j(m_1, \cdots, m_j) = \frac{1}{j!\alpha^{2j}} \left\langle \left\{ M_{xy}(n) - \sum_{l=0}^{j-1} G_l[k_l; \alpha_x(n)] \right\} \alpha_x(n - m_1) \cdots \alpha_x(n - m_j) \right\rangle \tag{2.47}$$

since the product $\alpha_x(n - m_1) \cdots \alpha_x(n - m_j)$ is a j^{th} order Volterra functional. For $j = 1$, the first order Wiener kernel reduces to the input-output cross-correlation defined in Equation 2.7.

According to Equation 2.45, each Wiener functional $G_j[k_j; \alpha_x(n)]$ with order $j > 1$ may have a non-zero linear component $k_{1(j)}(m)$. The overall linear component $h_1(m)$, the first order Volterra kernel, must be the sum of $k_1(m)$ and all the first order derived kernels, $k_{1(j)}(m)$. For even j, $k_{1(j)}(m) \equiv 0$, consequently,

$$h_1(m) = k_1(m) + k_{1(3)}(m) + k_{1(5)}(m) + \cdots \ . \tag{2.48}$$

From Equation 2.28 the Fourier transform of the first order Wiener kernel for the random flip angle excitation is

$$K_1(\omega) = \frac{i\, M_e(1 - E_1)\, e^{-\alpha^2/2}}{1 - E_1\, e^{-\alpha^2/2}} \frac{1 - E_2\, e^{i(\theta + \omega T_R)}}{D(\omega)} \tag{2.49}$$

where $D(\omega)$ is given by

$$D(\omega) = 1 - E_2 \cos\theta (1 + e^{-\alpha^2/2})\, e^{i\omega T_R} + E_2^2\, e^{-\alpha^2/2}\, e^{2i\omega T_R}.$$

The derivations for the derived kernels are long and tedious (see Appendix A). Only $k_{1(3)}(m)$ and $k_{1(5)}(m)$ have been derived. The Fourier transforms of the derived kernels are

$$K_{1(3)}(\omega) = \frac{\alpha^2 K_1(\omega)}{2} \left[Y(\omega) + \frac{E_1 e^{-\alpha^2/2}}{1 - E_1 e^{-\alpha^2/2}} \right] \tag{2.50}$$

and

$$K_{1(5)}(\omega) = \frac{\alpha^4 K_1(\omega)}{8}$$
$$\left\{ Y(\omega) \left[2Y(\omega) - \frac{1 - 3E_1 e^{-\alpha^2/2}}{1 - E_1 e^{-\alpha^2/2}} \right] + E_1 e^{-\alpha^2/2} \frac{1 + E_1 e^{-\alpha^2/2}}{(1 - E_1 e^{-\alpha^2/2})^2} \right\} \quad (2.51)$$

where

$$Y(\omega) = \frac{1 - E_2 \cos\theta \, e^{i\omega T_R}}{D(\omega)}.$$

The above expressions show that $k_{1(j)}$ is proportional to α^{j-1}. Therefore, when the excitation power is vanishingly small, $h_1(m) = k_1(m) =$ FID. As the excitation power is increased, the magnetization response becomes increasingly nonlinear as the contributions to $h_1(m)$ from the first order derived kernels increase: $k_1(m)$ becomes a less accurate description of the FID. The discrepancy between $h_1(m)$ and $k_1(m)$ is manifested as a notch artifact and non-uniform spectral response.

The line shape of $K_{1(3)}(\omega)$ is shown in Figure 2.7. Compared with $K_1(\omega)$ in Figure 2.1a, $K_{1(3)}(\omega)$ has a narrower line width and less notch artifact. The line shape of $K_{1(5)}(\omega)$, as shown in Figure 2.8, is quite different from that of $K_1(\omega)$. The sum of $K_1(\omega)$, $K_{1(3)}(\omega)$ and $K_{1(5)}(\omega)$ in Figure 2.9 is Lorentzian at low excitation power level. At higher excitation power level the sum has a narrower line width and less notch artifact than $K_1(\omega)$ in Figure 2.1. It may not be a perfect reconstruction of an ideal Lorentzian line shape at high excitation power level, however, the sum is definitely a more faithful estimate than $K_1(\omega)$.

The Wiener series analysis is a tool to provide a better understanding of the source of the saturation behavior. It shows that the first order input-output cross-correlation is inadequate in estimating the true FID when there are significant nonlinear components in the magnetization response. Other first order derived kernels must be included. Figure 2.5 shows that such compensation is necessary even when $\alpha = \alpha_{max}$, i.e. when the magnetization response gives a maximum S/N ratio. However, the next two sections will show that compensation is not necessary when the RF phase is random.

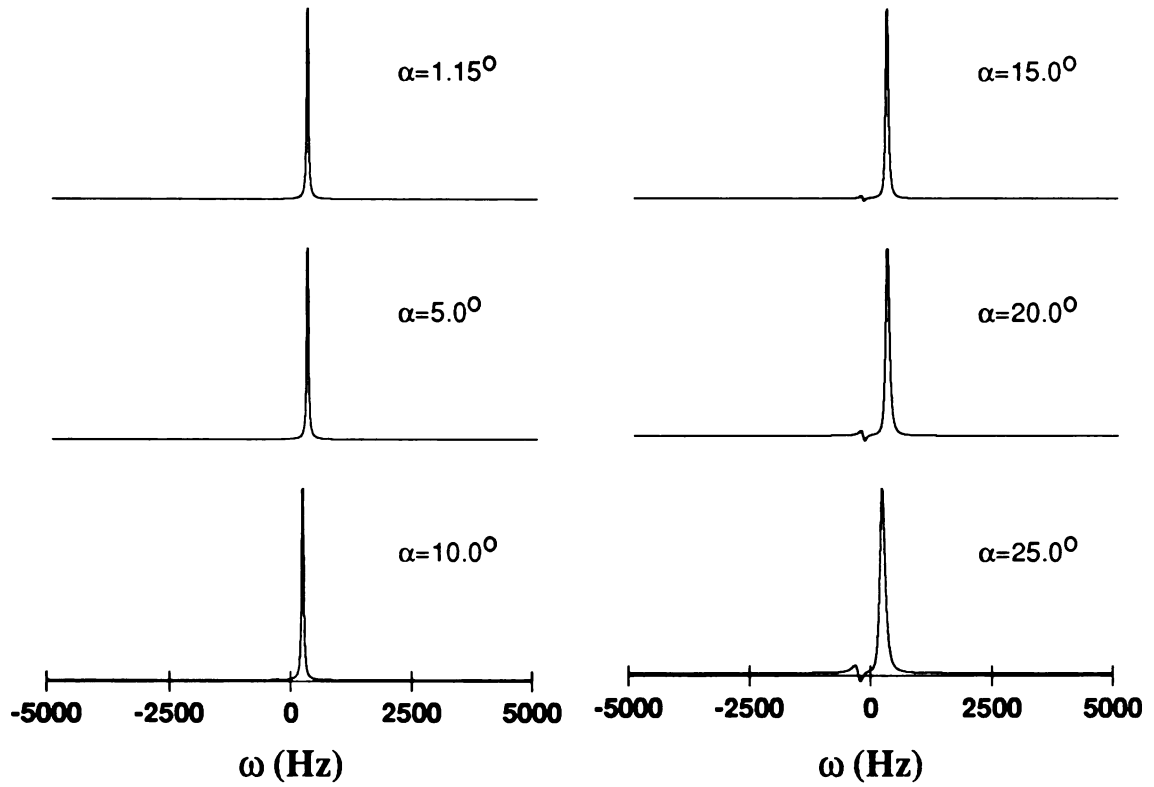

Figure 2.7: Line shape of $K_{1(3)}(\omega)$ for random flip angle excitation with Gaussian white noise. $T_1 = 0.5$s, $T_2 = 10$ms, $T_R = 0.1$ms and $\nu = 250$Hz.

2.4 Random Phase Excitation

In this section, assume that the RF vector has a fixed flip angle α, however, the RF phase is a random variable, $\phi(n)$, uniformly distributed from $-\pi$ to π (Figure 1.4b). Furthermore, $\phi(n)$ is assumed to be time uncorrelated:

$$\langle \phi(n)\, \phi(m) \rangle = \frac{\pi^2}{3} \delta_{nm}. \tag{2.52}$$

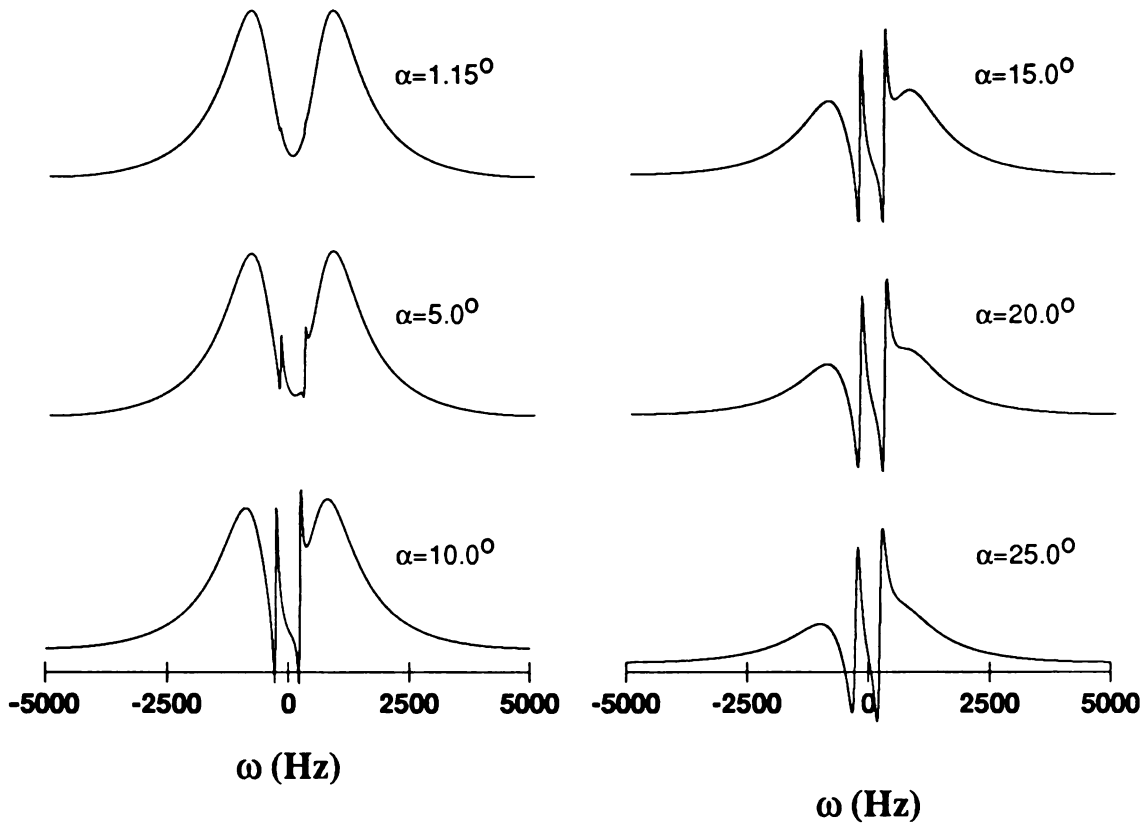

Figure 2.8: Line shape of $K_{1(5)}(\omega)$ for random flip angle excitation with Gaussian white noise. $T_1 = 0.5$s, $T_2 = 10$ms, $T_R = 0.1$ms and $\nu = 250$Hz.

The excitation sequence $\boldsymbol{\alpha}(n)$ is then given by

$$\boldsymbol{\alpha}(n) = \begin{bmatrix} \alpha \cos\phi(n) \\ \alpha \sin\phi(n) \\ 0 \end{bmatrix} \tag{2.53}$$

which has a zero mean and satisfies equation 2.1 with

$$\boldsymbol{C}_\alpha = \begin{bmatrix} \frac{\alpha^2}{2} & 0 & 0 \\ 0 & \frac{\alpha^2}{2} & 0 \\ 0 & 0 & 0 \end{bmatrix}. \tag{2.54}$$

The average excitation power is $\langle \boldsymbol{\alpha}^T(n)\,\boldsymbol{\alpha}(n) \rangle = \alpha^2$.

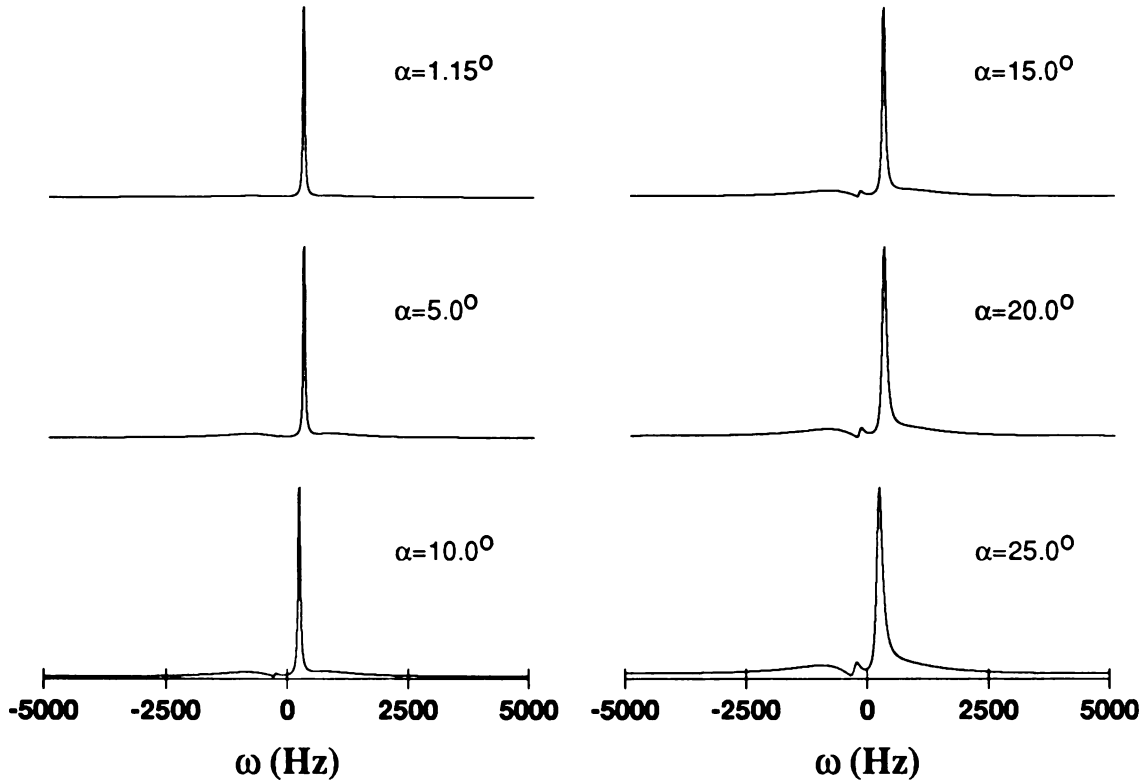

Figure 2.9: Line shape of $K_1(\omega) + K_{1(3)}(\omega) + K_{1(5)}(\omega)$ for random flip angle excitation with Gaussian white noise. $T_1 = 0.5$s, $T_2 = 10$ms, $T_R = 0.1$ms and $\nu = 250$Hz.

With the assumption of hard pulses, the RF rotation matrix $\boldsymbol{R}_\alpha(n)$ is

$$
\begin{aligned}
&\boldsymbol{R}_\alpha(n) \\
&= \begin{bmatrix} \cos\phi(n) & -\sin\phi(n) & 0 \\ \sin\phi(n) & \cos\phi(n) & 0 \\ 0 & 0 & 1 \end{bmatrix} \begin{bmatrix} 1 & 0 & 0 \\ 0 & \cos\alpha & \sin\alpha \\ 0 & -\sin\alpha & \cos\alpha \end{bmatrix} \begin{bmatrix} \cos\phi(n) & \sin\phi(n) & 0 \\ -\sin\phi(n) & \cos\phi(n) & 0 \\ 0 & 0 & 1 \end{bmatrix} \\
&= \begin{bmatrix} \cos^2\phi(n) + \sin^2\phi(n)\cos\alpha & \cos\phi(n)\sin\phi(n)(1-\cos\alpha) & -\sin\phi(n)\sin\alpha \\ \cos\phi(n)\sin\phi(n)(1-\cos\alpha) & \sin^2\phi(n) + \cos^2\phi(n)\cos\alpha & \cos\phi(n)\sin\alpha \\ \sin\phi(n)\sin\alpha & -\cos\phi(n)\sin\alpha & \cos\alpha \end{bmatrix}
\end{aligned}
\tag{2.55}
$$

which has a mean

$$\boldsymbol{\mu}_R = \begin{bmatrix} \cos^2\frac{\alpha}{2} & 0 & 0 \\ 0 & \cos^2\frac{\alpha}{2} & 0 \\ 0 & 0 & \cos\alpha \end{bmatrix}. \tag{2.56}$$

Equation 2.6 then gives the mean magnetization

$$\boldsymbol{\mu}_M = \frac{M_e\,(1-E_1)\,\cos\alpha}{1-E_1\cos\alpha} \begin{bmatrix} 0 \\ 0 \\ 1 \end{bmatrix}. \tag{2.57}$$

Combining Equations 2.4, 2.11 and 2.57 gives

$$\boldsymbol{A} = \frac{M_e\,(1-E_1)\,\alpha\,\sin\alpha}{2(1-E_1\cos\alpha)} \begin{bmatrix} 0 & -1 & 0 \\ 1 & 0 & 0 \\ 0 & 0 & 0 \end{bmatrix}. \tag{2.58}$$

Equation 2.16 then gives $K_1(\omega)$, the estimate of the real spectrum,

$$K_1(\omega) = \frac{i\,M_e\,(1-E_1)\,\sin\alpha}{\alpha(1-E_1\cos\alpha)} \; \frac{1}{1-E_2\cos^2\frac{\alpha}{2}\,e^{i(\omega T_R-\theta)}}. \tag{2.59}$$

Notice that $K_1(\omega)$ has only 1 pole at $\omega = \theta/T_R = 2\pi\nu$, which is the resonance offset of the spin. This means that the line is Lorentzian centered at the expected resonance offset. The only deviation in line shape from that obtained by a conventional FT-NMR experiment with long interpulse delay is the line width:

$$\frac{1}{\pi T_2} - \frac{1}{\pi T_R}\log\cos^2\frac{\alpha}{2}.$$

The second term is a line broadening which increases with the excitation power. It is important to notice that the line height and line shape are independent of θ. The interpulse dephase θ determines only the line location. Figure 2.10 shows plots of the line shape and the integrated line intensity of $K_1(\omega)$ for different flip angles. Notice that line broadening is the only spectral distortion as the flip angle is increased.

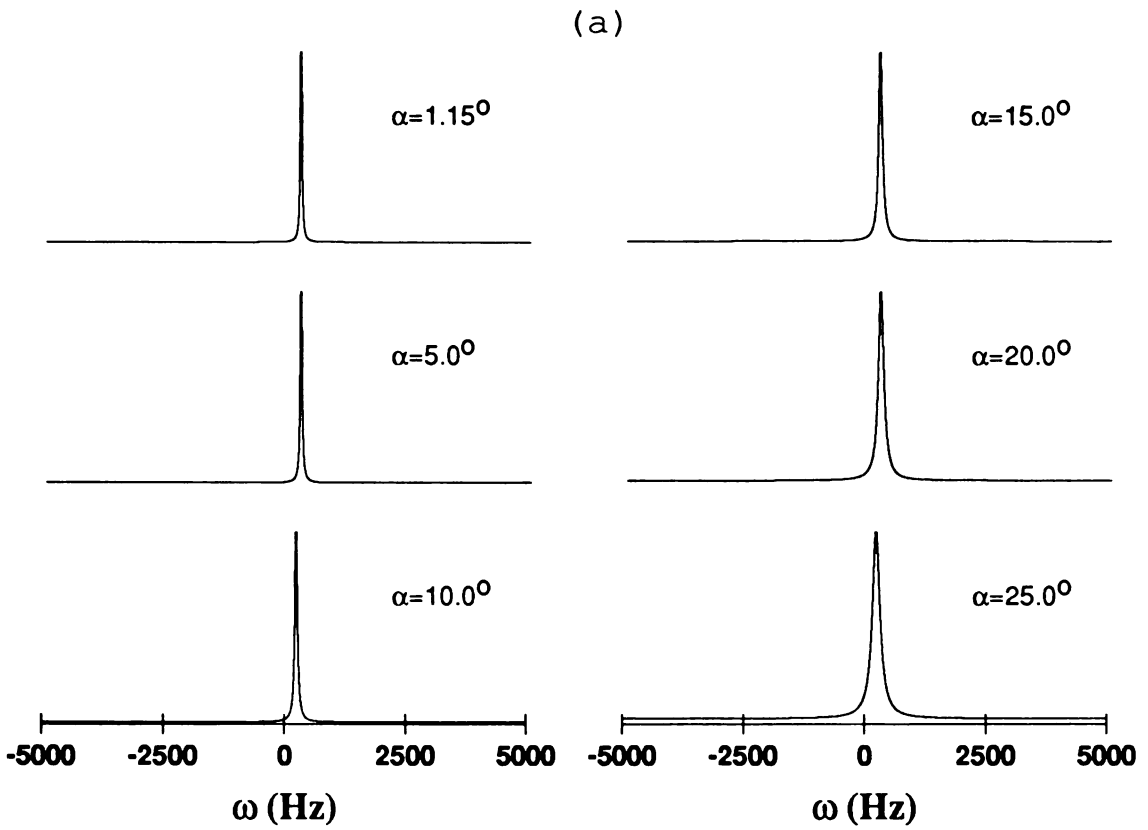

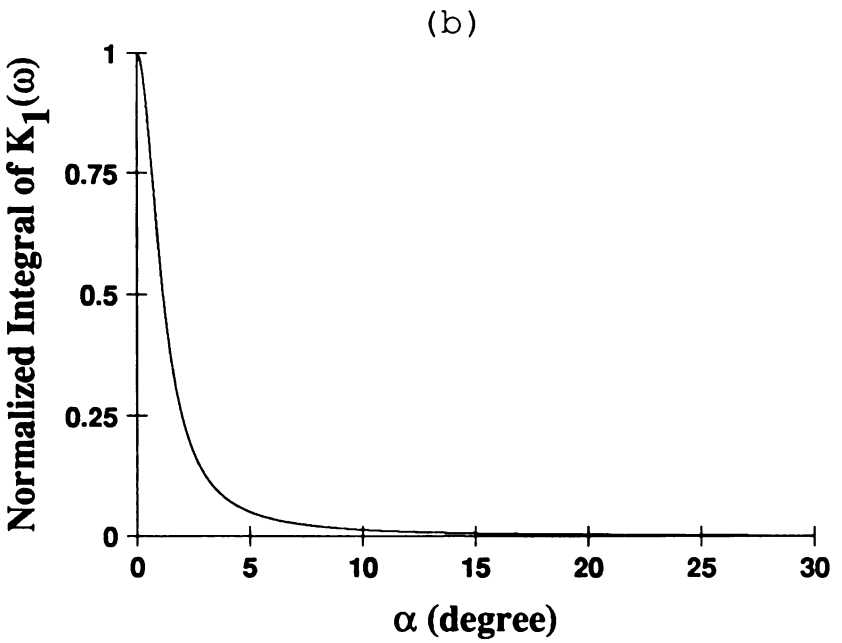

Figure 2.10: $K_1(\omega)$ for random phase excitation. (a) Line shape (absorption part) and (b) integrated line intensity normalized by the value at $\alpha = 0°$. $T_1 = 0.5$s, $T_2 = 10$ms, $T_R = 0.1$ms and $\nu = 250$Hz.

The probability distribution of $\phi(n)$ is not necessarily continuous. One possible discrete distribution is for $\phi(n)$ to take on the values, $\pm 45°$ and $\pm 135°$, each with a probability of 1/4. This can be implemented easily by using two independent binary maximum length sequences. The outputs of the MLS generators combined to give four possible outcomes that are equally likely to occur. This quaternary output is then used to select the four possible RF phases.

Solving Equation 2.18 gives

$$\langle \boldsymbol{M}\,\boldsymbol{M}^T \rangle = \frac{M_e^2(1-E_1)^2}{1-\frac{1}{2}E_2^2(1+\cos^2\alpha)-E_1^2\cos^2\alpha+E_1^2E_2^2(1-\frac{3}{2}\sin^2\alpha)} \times\frac{1+E_1\cos\alpha}{1-E_1\cos\alpha}\begin{bmatrix} \frac{1}{2}\sin^2\alpha & 0 & 0 \\ 0 & \frac{1}{2}\sin^2\alpha & 0 \\ 0 & 0 & \cos^2\alpha-E_2^2(1-\frac{3}{2}\sin^2\alpha) \end{bmatrix}. \tag{2.60}$$

The average signal power is the sum of the first two diagonal elements

$$P=\frac{M_e^2(1-E_1)^2\sin^2\alpha}{1-\frac{1}{2}E_2^2(1+\cos^2\alpha)-E_1^2\cos^2\alpha+E_1^2E_2^2(1-\frac{3}{2}\sin^2\alpha)}\,\frac{1+E_1\cos\alpha}{1-E_1\cos\alpha}. \tag{2.61}$$

Notice that the average signal power P is not a function of the interpulse dephase θ. This further shows that the experimental response is uniform across the spectrum. Figure 2.11a is an example plot of the average signal power as a function of the flip angle α. The plot is almost identical to that for the random flip angle excitation (Figure 2.4a). The peak is at $\alpha_{max} = 1.15°$, which gives the maximum S/N ratio. Therefore, as discussed earlier, the peak power requirement for this type of excitation is usually orders of magnitude smaller than that for a conventional FT-NMR experiment. Figure 2.11b shows, once again, that α_{max} is approximately the Ernst angle, $\cos^{-1}(e^{-T_R/T_1})$.

The signal power spectrum can be obtained by combining Equations 2.24 and 2.60:

$$\begin{aligned} S(\omega) &= 2P\,\mathcal{R}e\left\{\frac{1}{1-E_2\cos^2\frac{\alpha}{2}\,e^{i(\omega T_R-\theta)}}\right\}-P \\ &= \frac{(1-E_2^2\cos^4\frac{\alpha}{2})P}{1-2E_2\cos^2\frac{\alpha}{2}\cos(\omega T_R-\theta)+E_2^2\cos^4\frac{\alpha}{2}}, \end{aligned} \tag{2.62}$$

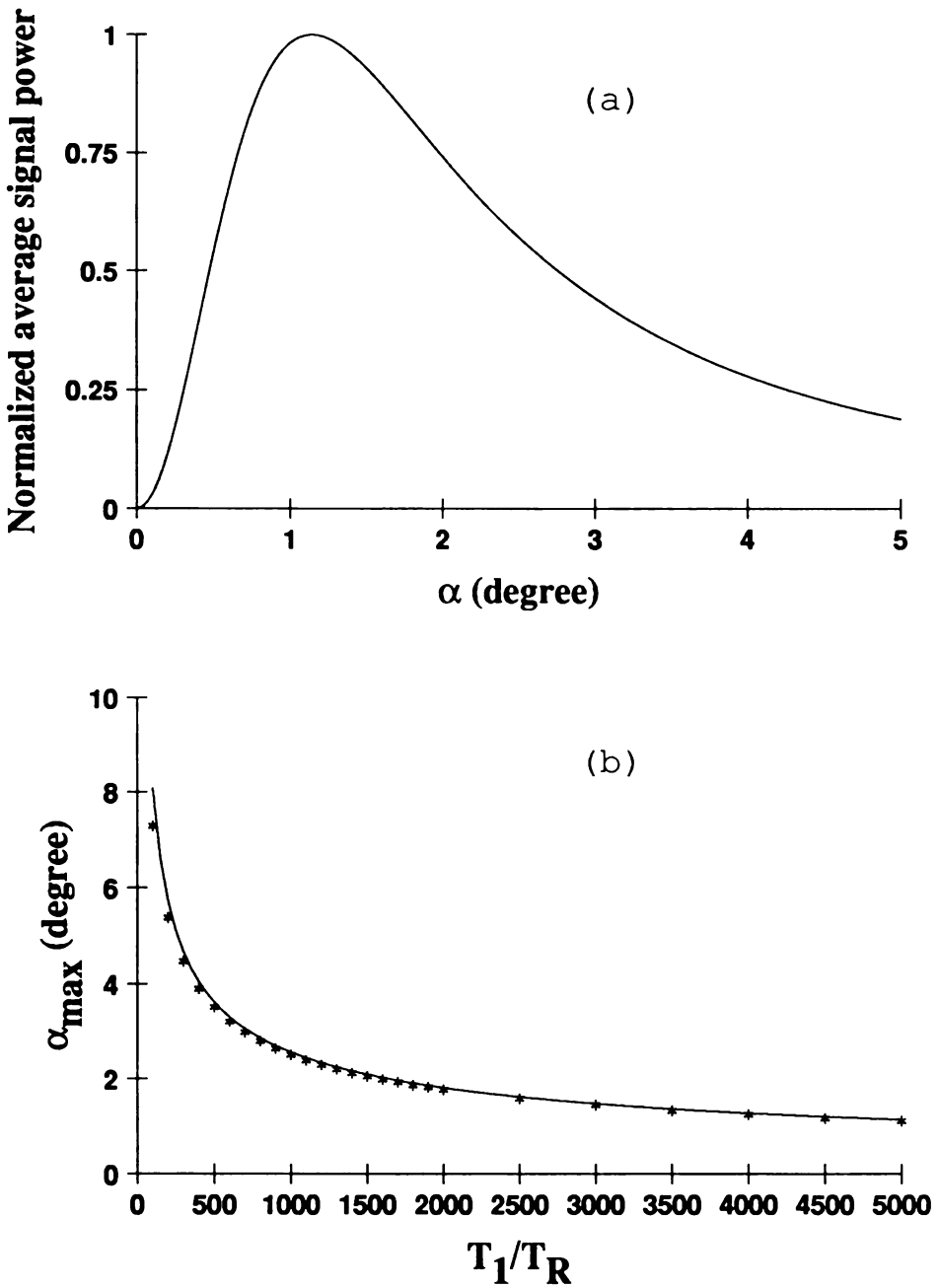

Figure 2.11: Random phase excitation. (a) Average signal power versus the flip angle. (b) α_{max} versus T_1/T_R. The symbol * represents theoretical values and the solid line is $\cos^{-1}(e^{-T_R/T_1})$. $T_1 = 0.5$sec, $T_2 = 10$ms, $T_R = 0.1$ms and $\nu = 250$Hz.

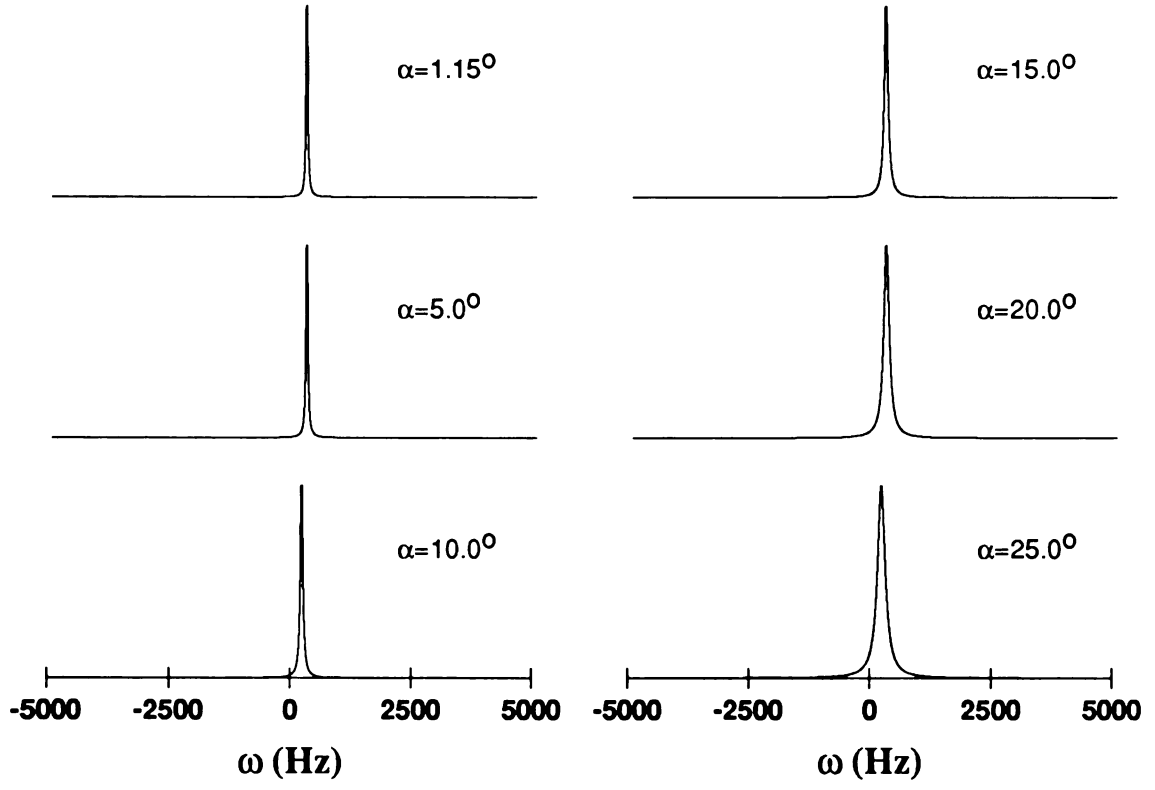

Figure 2.12: Power spectrum $S(\omega)$ for random phase excitation with different flip angles. $T_1 = 0.5$s, $T_2 = 10$ms, $T_R = 0.1$ms and $\nu = 250$Hz.

where Re$\{\}$ means the real part of the complex quantity inside the braces. Comparing $S(\omega)$ with $K_1(\omega)$ in Equation 2.59, it is obvious that $S(\omega)$ closely resembles the real part of $K_1(\omega)$, as demonstrated in Figures 2.10 and 2.12. Therefore, the signal power spectrum is also an accurate estimator of the real spectrum. The advantage of using the power spectrum is that it is calculated from the signal sequence only.

2.5 Random Quadrature Excitation

In this section, assume that the RF vector has two orthogonal components which are random but identically distributed and statistically independent (Figure 1.4c). Denote the excitation sequence as $\alpha(n) = [\alpha_x(n), \alpha_y(n), 0]^T$. The two components, $\alpha_x(n)$ and

$\alpha_y(n)$, are statistically independent and identically distributed. They must also satisfy the following two conditions:

1. $\alpha_x(n)$ and $\alpha_y(n)$ are time uncorrelated:

$$\langle [\alpha_j(n) - \mu_j][\alpha_j(m) - \mu_j] \rangle = \frac{\alpha^2}{2} \delta_{nm}$$

where $j = x$ or y and α^2 is the average excitation power.

2. $\alpha_x(n)$ and $\alpha_y(n)$ each have an even probability density function. This implies that the mean values, μ_x and μ_y, are zero.

The covariance matrix for $\boldsymbol{\alpha}(n)$ is the same as that for the random phase excitation in Equation 2.54. Define the RF magnitude and phase, respectively, as

$$\beta(n) = \sqrt{\alpha_x^2(n) + \alpha_y^2(n)}$$

and

$$\phi(n) = \tan^{-1}\left[\frac{\alpha_y(n)}{\alpha_x(n)}\right].$$

With the assumption of hard pulses, the RF rotation matrix $\boldsymbol{R}_\alpha(n)$ is

$$\begin{aligned}
&\boldsymbol{R}_\alpha(n) \\
&= \begin{bmatrix} \cos\phi(n) & -\sin\phi(n) & 0 \\ \sin\phi(n) & \cos\phi(n) & 0 \\ 0 & 0 & 1 \end{bmatrix} \begin{bmatrix} 1 & 0 & 0 \\ 0 & \cos\beta(n) & \sin\beta(n) \\ 0 & -\sin\beta(n) & \cos\beta(n) \end{bmatrix} \begin{bmatrix} \cos\phi(n) & \sin\phi(n) & 0 \\ -\sin\phi(n) & \cos\phi(n) & 0 \\ 0 & 0 & 1 \end{bmatrix} \\
&= \begin{bmatrix} \cos^2\phi(n) + \sin^2\phi(n)\cos\beta(n) & \cos\phi(n)\sin\phi(n)(1-\cos\beta(n)) & -\sin\phi(n)\sin\beta(n) \\ \cos\phi(n)\sin\phi(n)(1-\cos\beta(n)) & \sin^2\phi(n) + \cos^2\phi(n)\cos\beta(n) & \cos\phi(n)\sin\beta(n) \\ \sin\phi(n)\sin\beta(n) & -\cos\phi(n)\sin\beta(n) & \cos\beta(n) \end{bmatrix}
\end{aligned} \tag{2.63}$$

which has a mean

$$\boldsymbol{\mu}_R = \begin{bmatrix} \mu_1 & 0 & 0 \\ 0 & \mu_1 & 0 \\ 0 & 0 & \mu_2 \end{bmatrix} \tag{2.64}$$

where

$$\mu_1 = \langle \cos^2 \phi(n) + \sin^2 \phi(n) \cos \beta(n) \rangle = \langle \sin^2 \phi(n) + \cos^2 \phi(n) \cos \beta(n) \rangle \tag{2.65}$$

and

$$\mu_2 = \langle \cos \beta(n) \rangle. \tag{2.66}$$

Equation 2.6 gives the mean magnetization

$$\boldsymbol{\mu}_M = \frac{M_e (1 - E_1)\mu_2}{1 - E_1 \mu_2} \begin{bmatrix} 0 \\ 0 \\ 1 \end{bmatrix}. \tag{2.67}$$

Combining Equations 2.4, 2.11 and 2.67 gives

$$\boldsymbol{A} = \frac{M_e (1 - E_1)\mu_3}{1 - E_1 \mu_2} \begin{bmatrix} 0 & -1 & 0 \\ 1 & 0 & 0 \\ 0 & 0 & 0 \end{bmatrix} \tag{2.68}$$

where

$$\mu_3 = \langle \alpha_x(n) \cos \phi(n) \sin \beta(n) \rangle = \langle \alpha_y(n) \sin \phi(n) \sin \beta(n) \rangle. \tag{2.69}$$

Equation [2.16] then gives $K_1(\omega)$, the estimate of the real spectrum,

$$K_1(\omega) = \frac{i M_e (1 - E_1)\mu_3}{\alpha^2 (1 - E_1 \mu_2)} \frac{1}{1 - E_2 \mu_1 e^{i(\omega T_R - \theta)}}. \tag{2.70}$$

As for the random phase excitation, $K_1(\omega)$ has a Lorentzian line at the expected resonance offset. Line broadening is the only spectral distortion as the excitation power is increased. The line width is given by

$$\frac{1}{\pi T_2} - \frac{1}{\pi T_R} \log \mu_1,$$

where the second term is the line broadening. The line height and line shape are independent of θ, which means that the $K_1(\omega)$ response is uniform across the spectrum.

Solving Equation 2.18 and 2.24 gives

$$P = M_e^2 (1 - E_1)^2 \frac{1 + E_1\mu_2}{1 - E_1\mu_2} \frac{2p_3}{1 - E_2^2(p_1 + p_2) - E_1^2 p_4 + E_1^2 E_2^2 (p_2 p_4 + p_2 p_4 - 2p_3^2)} \tag{2.71}$$

and

$$\begin{aligned} S(\omega) &= 2P\,\mathcal{R}e\left\{\frac{1}{1 - E_2\mu_1\, e^{i(\omega T_R - \theta)}}\right\} - P \\ &= \frac{(1 - E_2^2\mu_1^2)P}{1 - 2E_2\mu_1 \cos(\omega T_R - \theta) + E_2^2\mu_1^2} \end{aligned} \tag{2.72}$$

where

$$\begin{aligned} p_1 &= \langle[\cos^2\phi(n) + \sin^2\phi(n)\,\cos\beta(n)]^2\rangle = \langle[\sin^2\phi(n) + \cos^2\phi(n)\,\cos\beta(n)]^2\rangle, \\ p_2 &= \langle\cos^2\phi(n)\,\sin^2\phi(n)\,[1 - \cos\beta(n)]^2\rangle, \\ p_3 &= \langle\sin^2\phi(n)\,\sin^2\beta(n)\rangle \quad \text{and} \\ p_4 &= \langle\cos^2\beta(n)\rangle. \end{aligned}$$

When $\alpha_x(n)$ and $\alpha_y(n)$ are zero mean Gaussian white noise,

$$\begin{aligned} \mu_1 &= 1 - g(\frac{\alpha^2}{4}), \\ \mu_2 &= 1 - 2\,g(\frac{\alpha^2}{4}), \\ \mu_3 &= \frac{\alpha^2}{4} + (1 - \frac{\alpha^2}{2})\,g(\frac{\alpha^2}{4}), \\ p_1 &= 1 - \frac{1}{2}\,g(\frac{\alpha^2}{4}) - \frac{3}{8}\,g(2\alpha^2), \\ p_2 &= \frac{1}{2}\,g(\frac{\alpha^2}{4}) - \frac{1}{8}\,g(2\alpha^2), \\ p_3 &= \frac{1}{3}\,g(2\alpha^2), \\ p_4 &= 1 - g(2\alpha^2), \end{aligned}$$

where

$$g(x) = x\,e^{-x}\,{}_1F_1(\frac{1}{2}, \frac{3}{2}; x)$$

and ${}_1F_1$ is a degenerate hypergeometric function [25] defined as

$$ {}_1F_1(a,b;x) = 1 + \frac{a}{b}\frac{x}{1!} + \frac{a(a+1)}{b(b+1)}\frac{x^2}{2!} + \frac{a(a+1)(a+2)}{b(b+1)(b+2)}\frac{x^3}{3!} + \cdots \ . $$

The resemblance of $K_1(\omega)$, P and $S(\omega)$ for the random phase excitation and those for the random quadrature excitation is quite obvious. The plots of $K_1(\omega)$, P and $S(\omega)$ are shown in Figures 2.13, 2.14 and 2.15, respectively. The discussions in previous section regarding line shape, line distortion, optimum excitation power, etc. also apply here. In fact, if $\alpha_x(n)$ and $\alpha_y(n)$ are random binary sequences taking on the two values, $\pm\alpha/\sqrt{2}$ with equal probability, the random quadrature excitation becomes a random phase excitation with flip angle α.

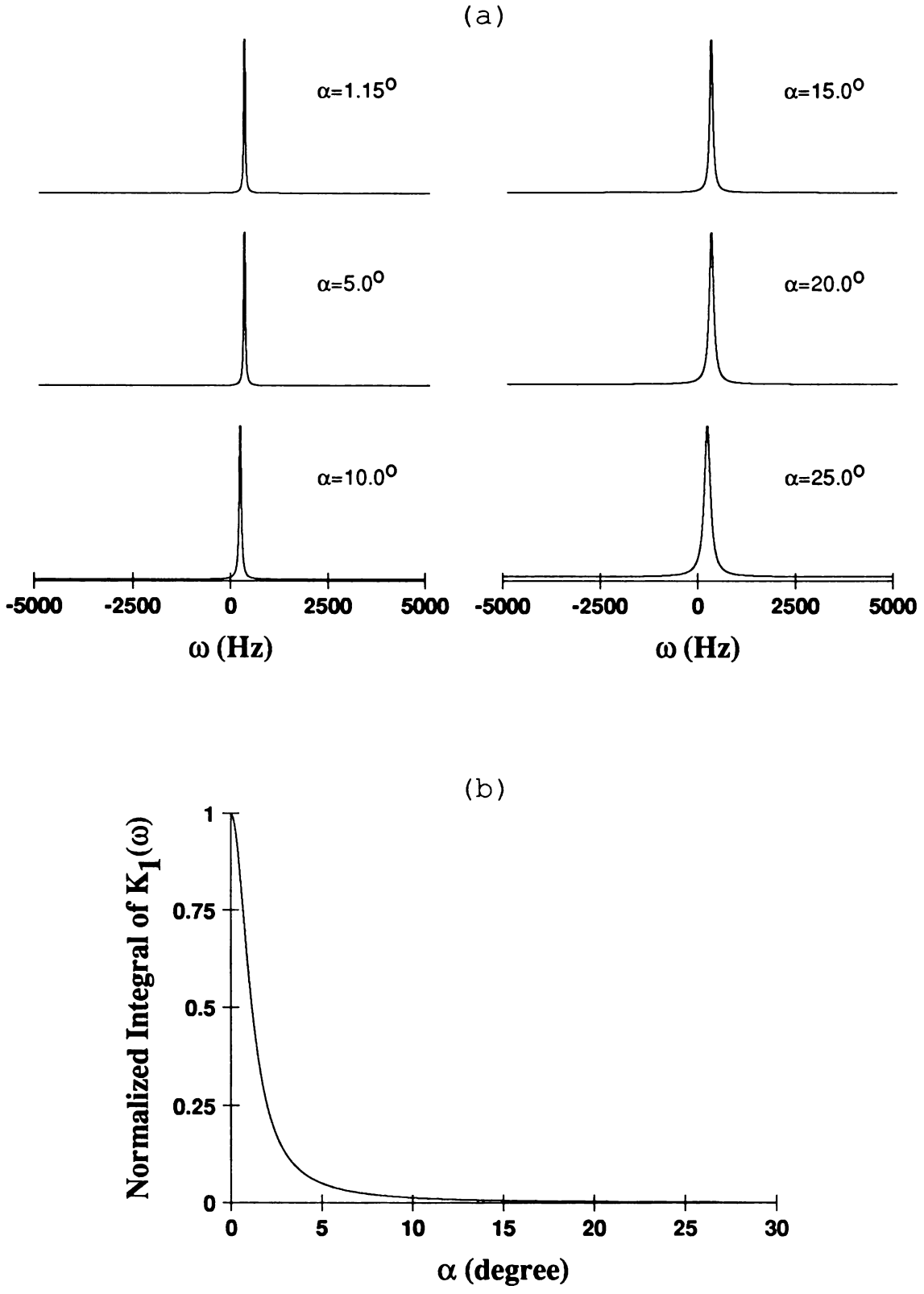

Figure 2.13: $K_1(\omega)$ for random quadrature excitation with Gaussian white noise. (a) Line shape (absorption part) and (b) integrated line intensity normalized by the value at $\alpha = 0°$. $T_1 = 0.5$s, $T_2 = 10$ms, $T_R = 0.1$ms and $\nu = 250$Hz.

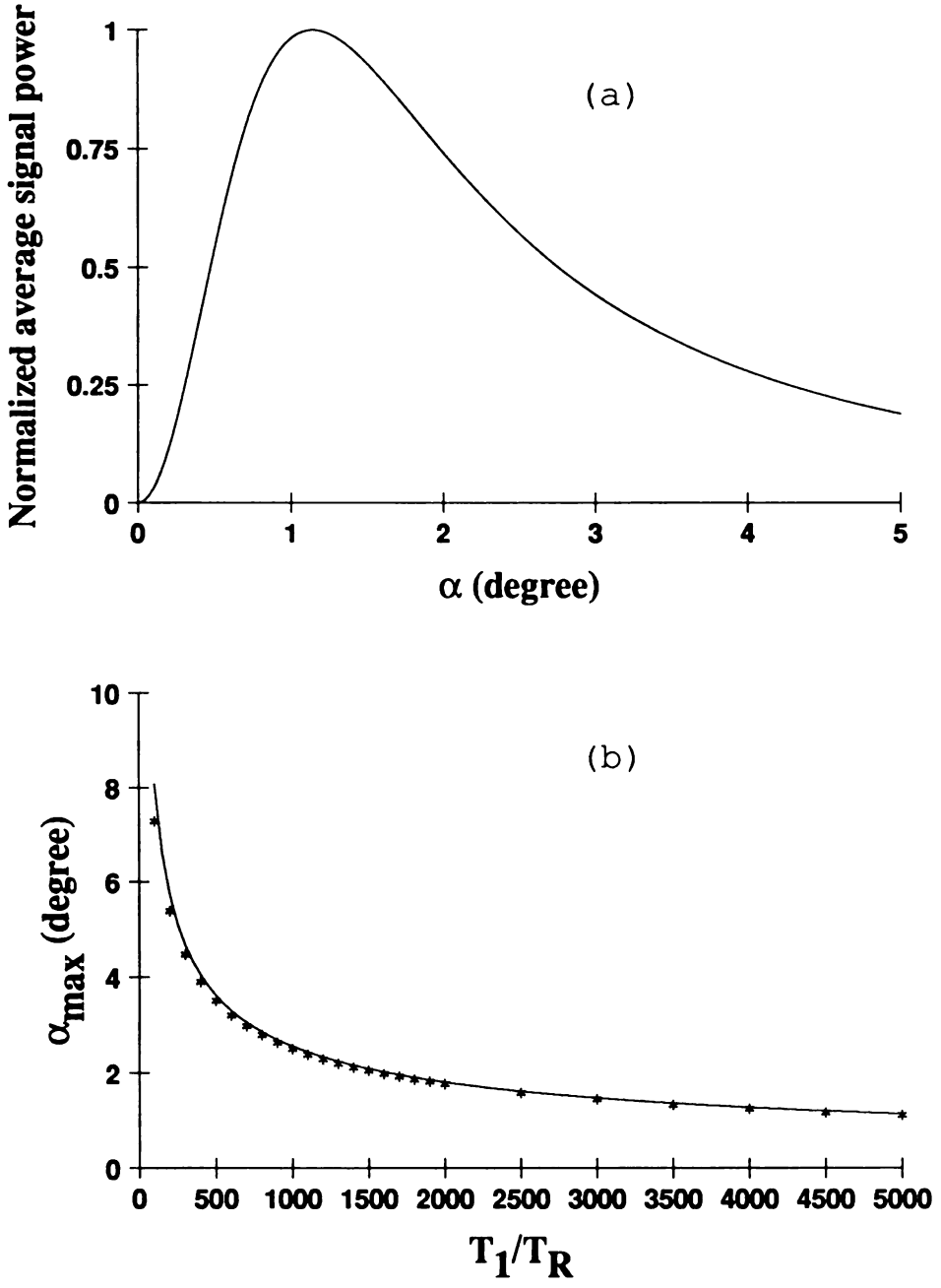

Figure 2.14: Random quadrature excitation with Gaussian white noise. (a) Average signal power versus the flip angle. (b) α_{max} versus T_1/T_R. The symbol * represents theoretical values and the solid line is $\cos^{-1}(e^{-T_R/T_1})$. $T_1 = 0.5$sec, $T_2 = 10$ms, $T_R = 0.1$ms and $\nu = 250$Hz.

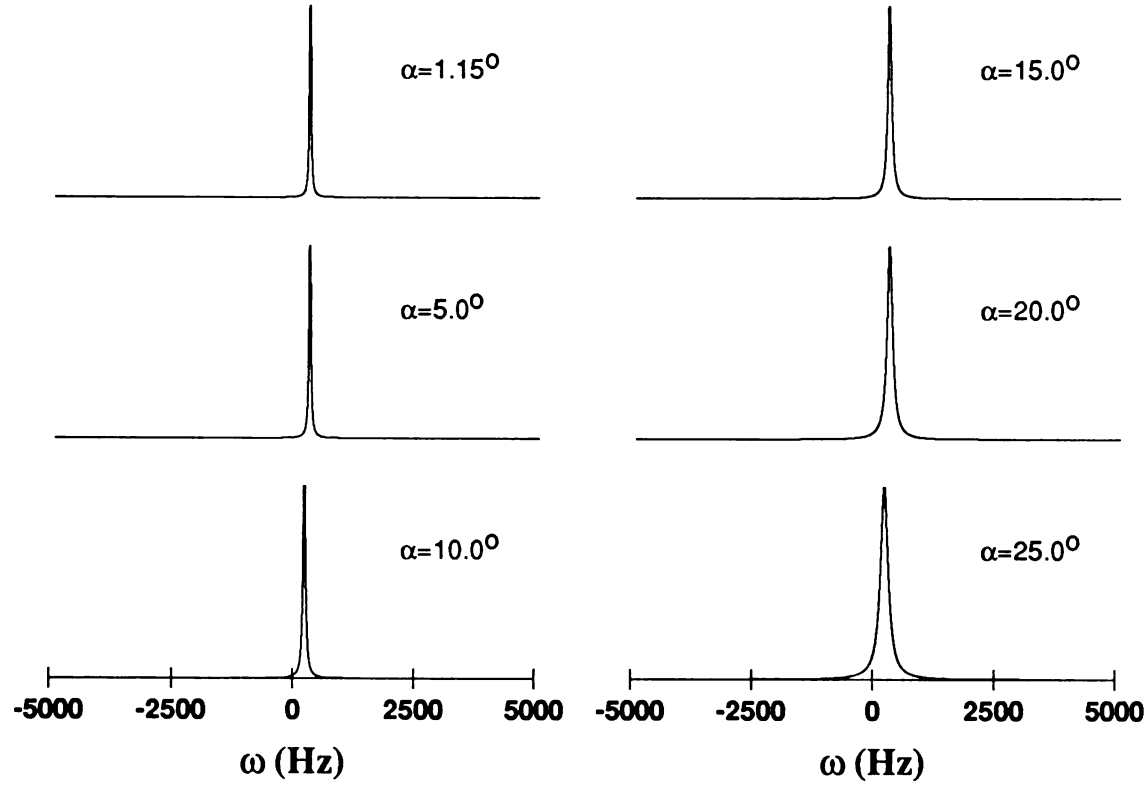

Figure 2.15: Power spectrum $S(\omega)$ for random quadrature excitation with Gaussian white noise. $T_1 = 0.5$s, $T_2 = 10$ms, $T_R = 0.1$ms and $\nu = 250$Hz.

2.6 Excitations with Non-zero Mean Sequences

All three types of excitation discussed in previous sections assume that the excitation sequence $\alpha(n)$ has zero mean. However, in practice, an imperfect RF transmitter or RF amplifier may introduce an offset to the amplitude or the phase of the RF pulses. Distortions may results from such undesirable offsets. The effects of non-zero mean excitation will be discussed in this section.

At low excitation power, the magnetization response is linear. The response to a non-zero mean excitation $\alpha(n)$ will be the sum of the response to the mean component and the response to the zero mean component. This means that the only effect of the mean component is to introduce an output offset. The response to the zero mean component

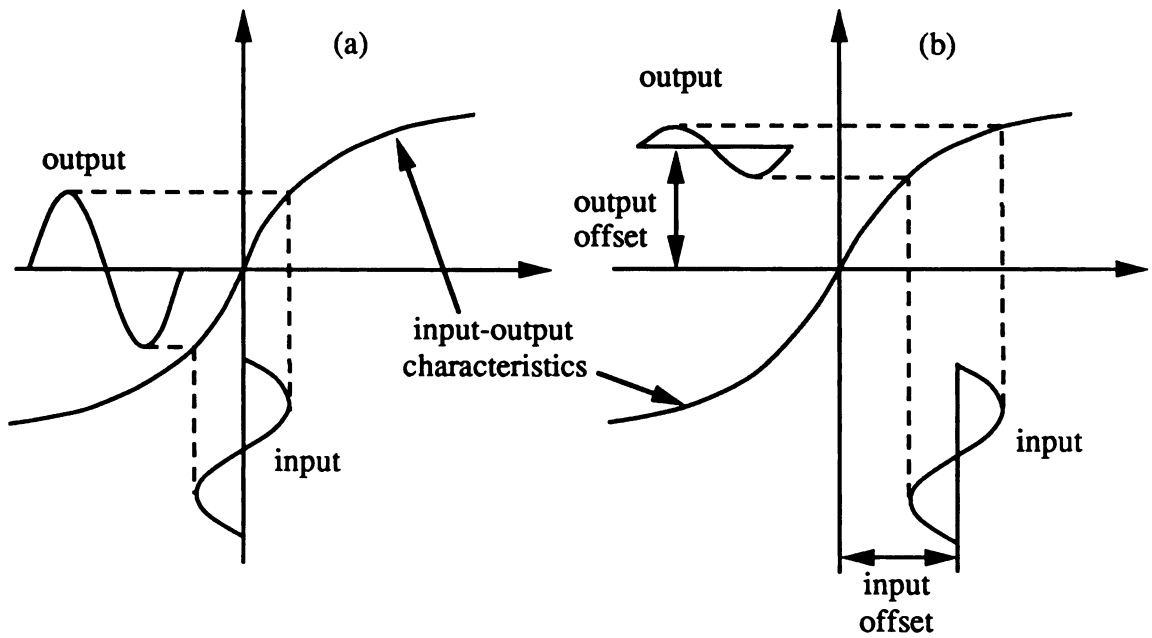

Figure 2.16: Response of a nonlinear system. (a) Zero mean excitation. (b) Non-zero mean excitation.

remains the same. When the excitation power is high, the magnetization response is nonlinear. Figure 2.16 demonstrates that the response of a nonlinear system to a non-zero mean input not only has an output offset, but may also have a distorted response to the zero-mean component.

A phase offset in the RF transmitter has no effect on the stochastic experiment because $\alpha(n)$ remains zero mean (Equation 2.53). This will be the case as long as $\phi(n)$ is distributed uniformly over a range of 2π radians, because the expectations of products of $\cos\phi(n)$ and $\sin\phi(n)$ to arbitrary powers remain the same even when $\phi(n)$ has a non-zero mean.

An amplitude offset in the RF transmitter or the RF amplifier will give a flip angle offset resulting in an excitation sequence $\alpha(n)$ with a non-zero mean. The non-zero mean excitation will move the spin system towards a more nonlinear regime (analo-

gous to Figure 2.16b). Consider the extreme situation where $\alpha(n) = \mu$ is non-random. Both the random flip angle excitation and the random quadrature excitation become a constant flip angle excitation, i.e. the well known steady state free precession (SSFP) experiment [1]. Let $\alpha(n) = [\mu_x, 0, 0]^T$. Then

$$\boldsymbol{R}_\alpha(n) = \boldsymbol{\mu}_R = \begin{bmatrix} 1 & 0 & 0 \\ 0 & \cos\mu_x & \sin\mu_x \\ 0 & -\sin\mu_x & \cos\mu_x \end{bmatrix}. \tag{2.73}$$

The magnetization vector acquires a steady state value $\boldsymbol{\mu}_M$ which is given by Equation 2.6:

$$\begin{aligned} \boldsymbol{\mu}_M &= \frac{M_e(1-E_1)}{(1-E_2\cos\theta)(1-E_1\cos\mu_x) - E_2(E_2-\cos\theta)(E_1-\cos\mu_x)} \\ &\quad \times \begin{bmatrix} E_2\sin\mu_x\sin\theta \\ E_2\sin\mu_x(1-E_2\cos\theta) \\ \cos\mu_x - E_2\cos\theta(1+\cos\mu_x) + E_2^2) \end{bmatrix}. \end{aligned} \tag{2.74}$$

The steady state signal power is

$$\begin{aligned} P &= \boldsymbol{B}^\dagger \boldsymbol{\mu}_M \boldsymbol{\mu}_M^T \boldsymbol{B} \\ &= \frac{M_e^2(1-E_1)^2\sin^2\mu_x(1-2E_2\cos\theta+E_2^2)}{(1-E_2\cos\theta)(1-E_1\cos\mu_x) - E_2(E_2-\cos\theta)(E_1-\cos\mu_x)}. \end{aligned} \tag{2.75}$$

This equation shows that the steady state signal power is a function of the interpulse dephase θ, i.e. a function of the resonance offset (Figure 2.17). It means that the steady state response will not be uniform across the spectrum.

When a random component is added, $\alpha(n) = [\alpha_x(n) + \mu_x, 0, 0]^T$, the experiment becomes a random angle excitation. The mean magnetization vector $\boldsymbol{\mu}_M$ will acquire a value very similar to the steady state value, i.e., the spin system is shifted towards undesirable operating conditions. The reconstructed $K_1(\omega)$ will have a non-uniform response across the spectrum. This is verified by an analysis similar to Section 2.2 but

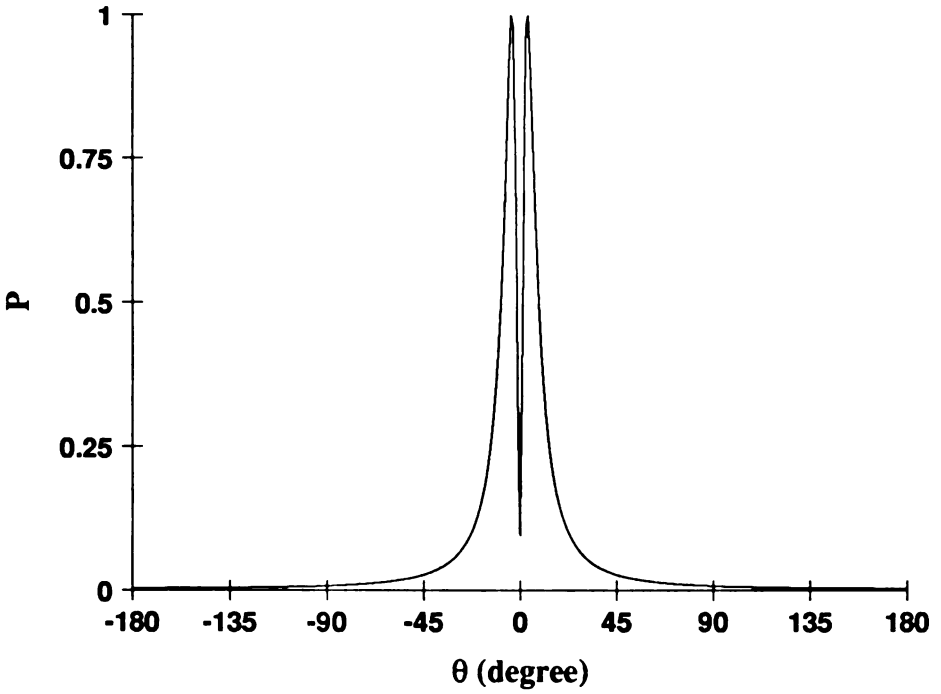

Figure 2.17: Steady state signal power as a function of the interpulse dephase. $T_1 = 0.5$s, $T_2 = 10$ms, $T_R = 0.1$ms and $\mu_x = 1.15°$.

with a non-zero mean $\alpha(n)$ defined above. The mean magnetization vector is

$$\begin{aligned}
\boldsymbol{\mu}_M &= \begin{bmatrix} \mu_{Mx} \\ \mu_{My} \\ \mu_{Mz} \end{bmatrix} \\
&= \frac{M_e(1-E_1)\varphi_\alpha(1)}{(1-E_2\cos\theta)(1-E_1\cos\mu_x\varphi_\alpha(1)) - E_2\varphi_\alpha(1)(E_2-\cos\theta)(E_1\varphi_\alpha(1)-\cos\mu_x)} \\
&\quad \times \begin{bmatrix} E_2\sin\mu_x\sin\theta \\ E_2\sin\mu_x(1-E_2\cos\theta) \\ \cos\mu_x - E_2\cos\theta(\varphi_\alpha(1)+\cos\mu_x) + E_2^2\varphi_\alpha(1) \end{bmatrix}. \qquad (2.76)
\end{aligned}$$

When the random component has zero power $\varphi_\alpha(1) = 1$ and the $\boldsymbol{\mu}_M$ above reduces to the steady state solution in Equation 2.74 as expected. The estimate of the spectrum is

$$K_1(\omega) = \frac{i\dot{\varphi}_\alpha(1)(1-E_2e^{i(\theta+\omega T_R)})}{\varphi_\alpha(1)}$$

$$\times \frac{E_1 \sin \mu_x \varphi_\alpha(1) \mu_{M_y} e^{i\omega T_R} - \mu_{M_x}[1 - E_1 \cos \mu_x \varphi_\alpha(1) e^{i\omega T_R}]}{D(\omega)} \quad (2.77)$$

where

$$\begin{aligned} D(\omega) &= (1 - E_2 \cos\theta\, e^{i\omega T_R})[1 - E_1 \cos \mu_x \varphi_\alpha(1) e^{i\omega T_R}] \\ &\quad - E_2 \varphi_\alpha(1) e^{i\omega T_R}(E_2 e^{i\omega T_R} - \cos\theta)[E_1 \varphi_\alpha(1) e^{i\omega T_R} - \cos \mu_x]. \quad (2.78) \end{aligned}$$

Figure 2.18a shows the line shapes of $K_1(\omega)$ obtained using a random binary excitation with a fixed RMS flip angle of 1.15° but different values of μ_x. The lines exhibit two different artifacts as the mean excitation increases, a notch artifact at zero resonance offset and a mirror image artifact at the negative of the resonance offset of the line. These distortions are analogous to the those caused by the input offset to a nonlinear system shown in Figure 2.16b. Figure 2.18b shows the reconstructed $K_1(\omega)$ for twenty-one lines equally spaced in frequency and centered at zero resonance offset. The line at zero resonance offset disappears due to saturation by the mean excitation. The overall response across the spectrum is highly non-uniform.

A similar analysis has been done for a binary quadrature excitation sequence $\alpha(n) = [\alpha_x(n) + \frac{\mu}{\sqrt{2}}, \alpha_y(n) + \frac{\mu}{\sqrt{2}}, 0]^T$. The expressions for the mean magnetization and $K_1(\omega)$ are too complicated to be shown here (see Appendix B). However, the plots in Figure 2.19 show distortions in the line shapes very similar to those for random binary flip angle excitation in Figure 2.18.

Binary maximum length sequences (MLS) are frequently used to approximate random binary excitations, not only because they are easy to generate but also because the Hadamard transform can be used to calculate the input-output cross-correlation. A n-bit binary MLS generator will produce sequences with a period of $2^n - 1$. In order to use the Hadamard transform, the full length of the sequence must be used. The same sequence can be repeated many times to improve the S/N ratio by coherent signal averaging. This means that the sequence is repeated every $(2^n - 1)T_R$ seconds. One important fact about MLS that takes on the values ± 1 is that the sum of one full period of the sequence is one

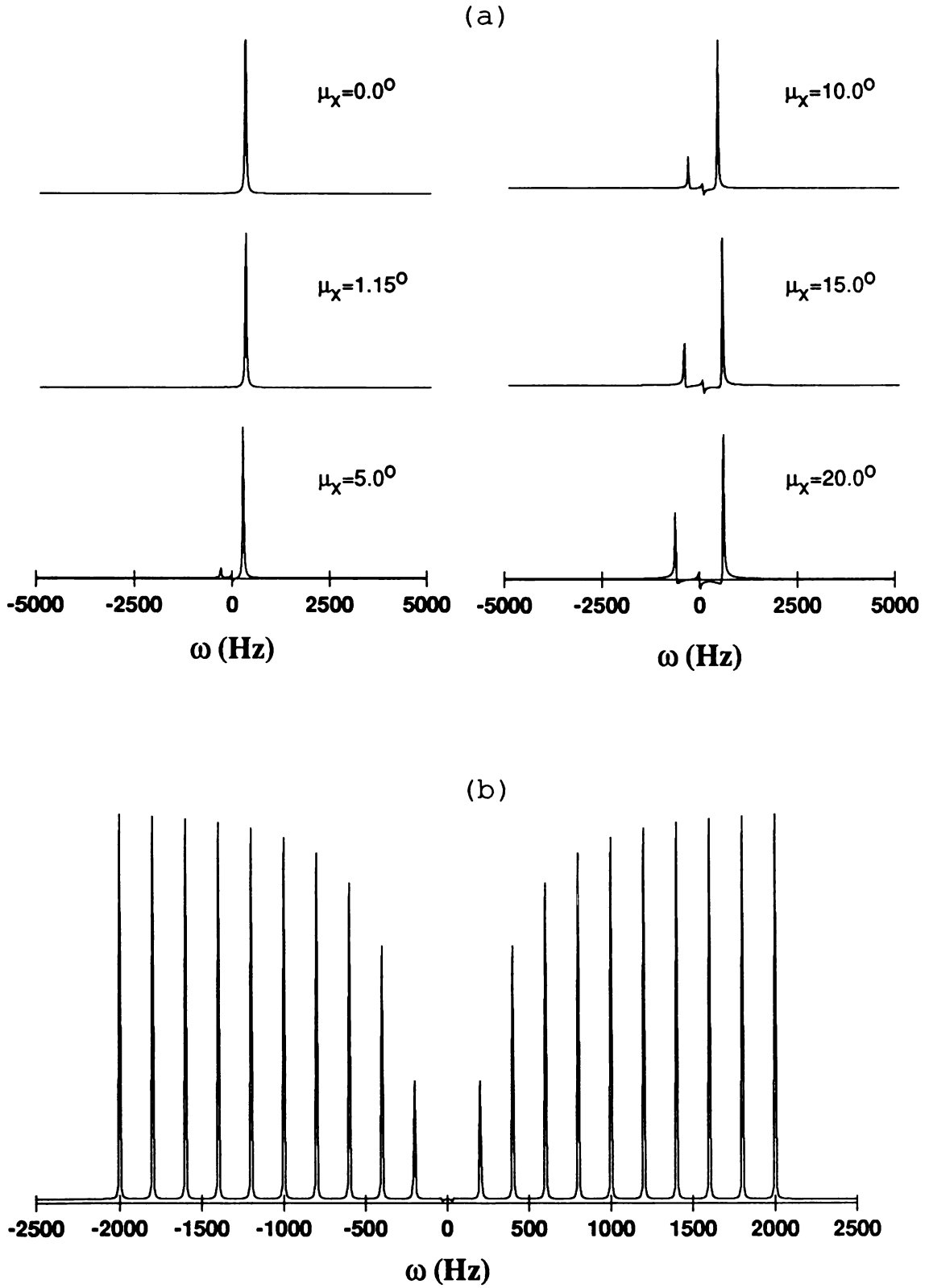

Figure 2.18: Line shapes of $K_1(\omega)$ obtained by random binary flip angle excitations with a non-zero mean. $T_1 = 0.5$s, $T_2 = 10$ms, $T_R = 0.1$ms and RMS flip angle is 1.15°. (a) Lines with different mean flip angles, μ_x. $\nu = 250$Hz. (b) Twenty-one lines at different resonance offsets. $\mu_x = 1.15°$.

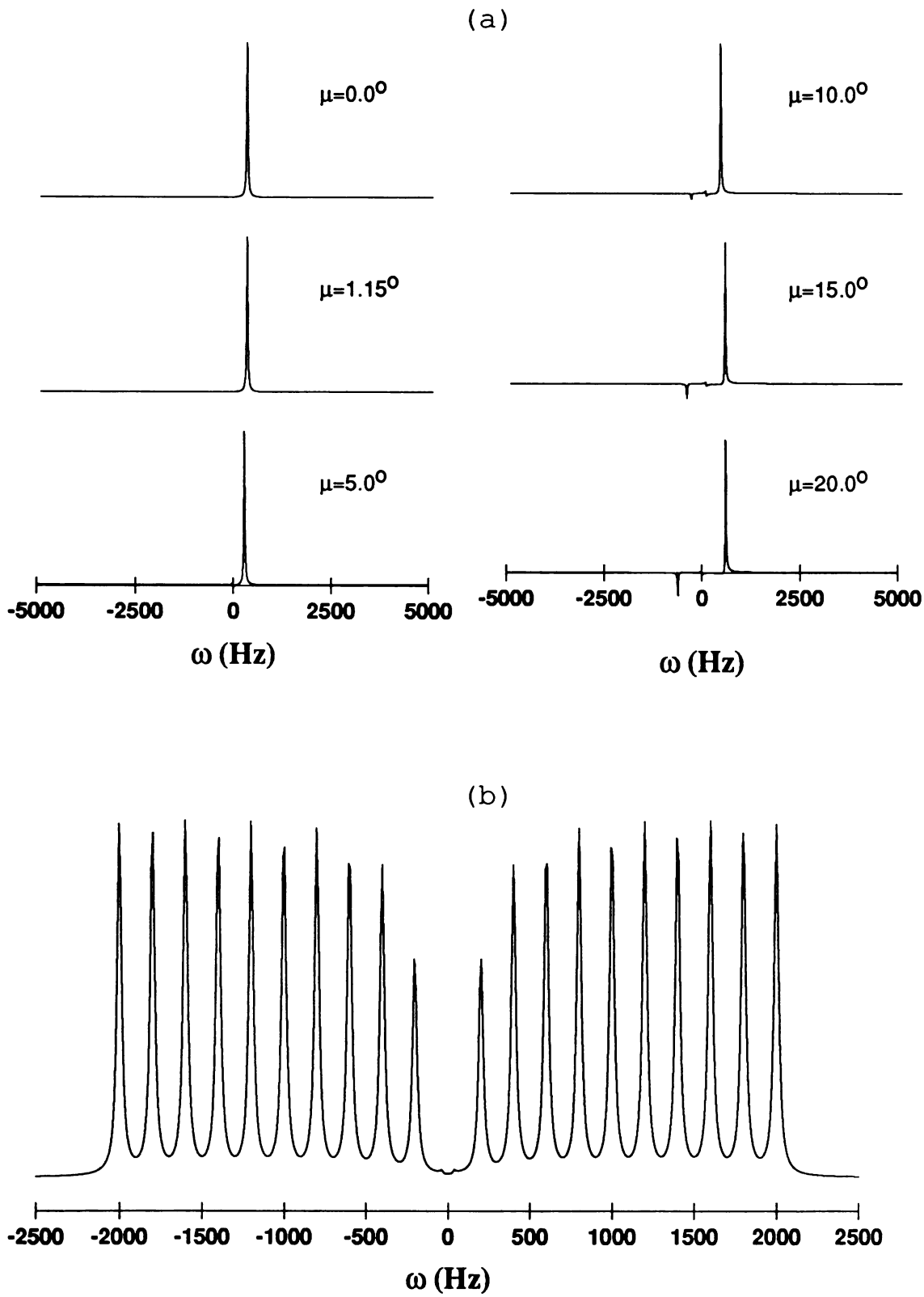

Figure 2.19: Line shapes of $K_1(\omega)$ obtained by random binary quadrature excitations with non-zero means in both components. $T_1 = 0.5$s, $T_2 = 10$ms, $T_R = 0.1$ms and RMS flip angle is 1.15°. (a) Lines with different mean flip angles. $\nu = 250$Hz. (b) Twenty-one lines at different resonance offsets. $\mu = 1.15°$.

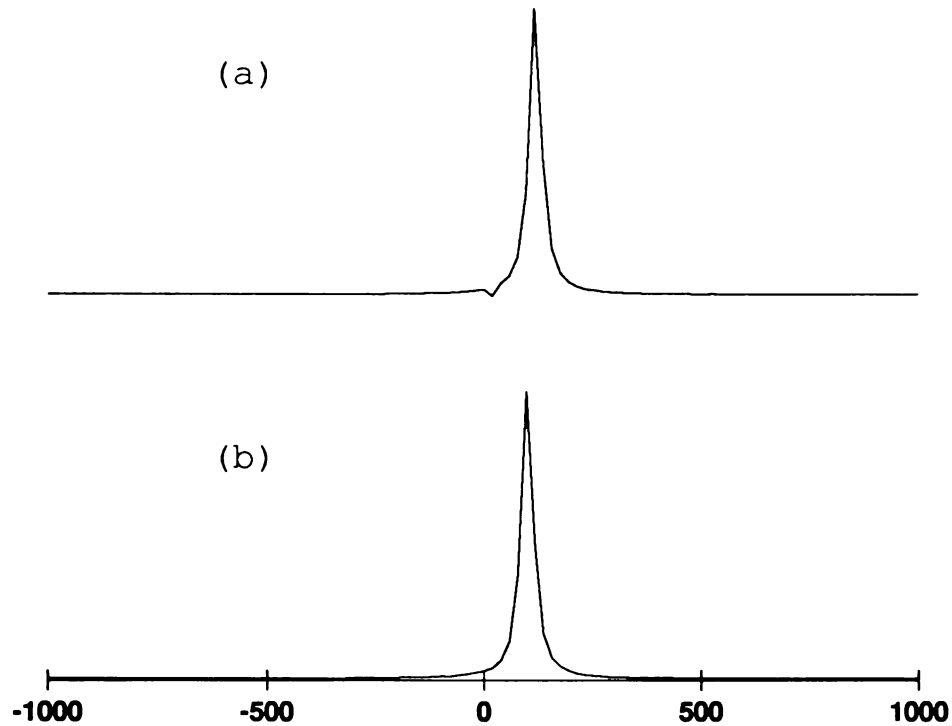

Figure 2.20: Computer simulated line shapes of $K_1(\omega)$ using random flip angle excitation with binary MLS. (a) 9-bit MLS generator. (b) 15-bit MLS generator. $T_1 = 0.5$s, $T_2 = 10$ms, $T_R = 0.1$ms, $\nu = 100$Hz and RMS flip angle $= 1.15°$.

or minus one. This implies that the sample experiences a non-zero mean excitation. If $(2^n - 1)T_R$ is small compared to T_1 and T_2, the effects of exciting with the full period of the MLS repeatedly will be similar to having a non-zero mean random binary excitation. Distortions may appear in the reconstructed spectrum as demonstrated by the computer simulations shown in Figure 2.20. The use of a 9-bit MLS generator results in a notch artifact near zero resonance offset. The artifact does not occur when a 15-bit MLS generator is used. This explains most of the artifacts reported by Chaudhuri [22] since he used only an 8-bit MLS generator.

Chapter 3

Systematic Noise

In the previous chapter, the input-output cross-correlation and the signal power spectrum are defined in terms of the expectation operator of probability theory. In practice, ergodicity is assumed and the expectation operator is approximated by a time average. For example, the cross-correlation of two processes, $x(n)$ and $y(n)$, is estimated by

$$\langle x(n)\, y^*(n-m)\rangle \approx \frac{1}{N}\sum_{n=0}^{N-1} x(n)\, y^*(n-m). \tag{3.1}$$

The approximation becomes an equality only when N approaches infinity, but in reality N is limited. Since the observed $x(n)$ and $y(n)$ are samples of two stochastic processes, the time average defined on the right hand side of the equation above will also be a sample of a stochastic process and in general will have a non-zero variance. This variance will usually appear as colored noise in the time average, and it is referred to as systematic noise. In addition to the systematic noise, the observed $x(n)$ and $y(n)$ also have measurement noise from the sample and the electronic hardware involved in the sampling process. To avoid structural artifacts resulting from the systematic noise, it is necessary to find the right imaging parameters and experimental setup so that the measurement noise is the dominant noise source. The first three sections of this chapter will investigate how the measurement noise and the systematic noise decrease as N is increased. A comparison of Gaussian white noise excitation and MLS excitation will be made in terms of systematic noise generation. In 1982 Blümich and Ziessow [14] showed that high power MLS excitation results in noise-like distortion in the recon-

structed spectra. The last section of this chapter is a detailed analysis of the origin of this noise-like distortion.

3.1 Systematic Noise and Measurement Noise

First consider the case without measurement noise. In the stochastic experiments analyzed in the previous chapter, there are two possible estimators of the real spectrum, $K_1(\omega)$ and $S(\omega)$. They are the Fourier transforms of the input-output cross-covariance and the signal auto-covariance. From Equations 2.7 and 3.1, the time average estimators of the input-output cross-covariance and the signal auto-covariance are, respectively,

$$k_1^N(m) = \frac{1}{N\alpha^2}\boldsymbol{B}^\dagger\left\{\sum_{n=0}^{N-1}[\boldsymbol{M}(n)-\boldsymbol{\mu}_M][\boldsymbol{\alpha}(n-m)-\boldsymbol{\mu}_\alpha]^T\right\}\boldsymbol{B} \tag{3.2}$$

and

$$r^N(m) = \frac{1}{N}\boldsymbol{B}^\dagger\left\{\sum_{n=0}^{N-1}[\boldsymbol{M}(n)-\boldsymbol{\mu}_M][\boldsymbol{M}(n-m)-\boldsymbol{\mu}_M]^T\right\}\boldsymbol{B} \tag{3.3}$$

where the superscript N denotes the dependence on N. It is obvious that $\langle k_1^N(m)\rangle = k_1(m)$ and $\langle r^N(m)\rangle = r(m)$, i.e., they are unbiased estimators. The variances of $k_1^N(m)$ and $r^N(m)$ are defined as

$$Var\{k_1^N(m)\} = \langle|k_1^N(m)|^2\rangle - |k_1(m)|^2 \tag{3.4}$$

and

$$Var\{r^N(m)\} = \langle|r^N(m)|^2\rangle - |r(m)|^2. \tag{3.5}$$

In practice, the data acquired include measurement noise from the sample and electronic hardware. In most cases, the measurement noise is a Gaussian white noise. When representing the transverse magnetization $M_{xy}(n)$, or the signal, as a complex sequence, the measurement noise can be represented as $\mathcal{N}_{xy}(n) = \mathcal{N}_x(n) + i\mathcal{N}_y(n)$ where $\mathcal{N}_x(n)$ and $\mathcal{N}_y(n)$ are independent Gaussian white noises with a variance of $\sigma^2/2$, so that the noise power is σ^2. In general, it is safe to assume that the measurement noise is also independent of the stochastic excitation sequence $\alpha(n)$, and hence independent of the

transverse magnetization. Define the noise vector as $\mathcal{N}(n) = [\mathcal{N}_x(n), \mathcal{N}_y(n), 0]$. An estimator of the input-output cross-covariance which includes the measurement noise is

$$\tilde{k}_1^N(m) = \frac{1}{N\alpha^2} \boldsymbol{B}^\dagger \left\{ \sum_{n=0}^{N-1} [\boldsymbol{M}(n) + \boldsymbol{\mathcal{N}}(n) - \boldsymbol{\mu}_M][\boldsymbol{\alpha}(n-m) - \boldsymbol{\mu}_\alpha]^T \right\} \boldsymbol{B}. \quad (3.6)$$

Since the measurement noise and the excitation sequence are independent, the estimator is unbiased, i.e. $\langle \tilde{k}_1^N(m) \rangle = k_1(m)$. From Equation 3.6, the variance of the estimator is

$$\begin{aligned}
Var\{\tilde{k}_1^N(m)\} &= \langle |\tilde{k}_1^N(m)|^2 \rangle - |k_1(m)|^2 \\
&= \left\langle \left| \frac{1}{N\alpha^2} \boldsymbol{B}^\dagger \left\{ \sum_{n=0}^{N-1} [\boldsymbol{M}(n) - \boldsymbol{\mu}_M][\boldsymbol{\alpha}(n-m) - \boldsymbol{\mu}_\alpha]^T \right\} \boldsymbol{B} \right|^2 \right\rangle \\
&\quad -|k_1(m)|^2 + \left\langle \left| \frac{1}{N\alpha^2} \boldsymbol{B}^\dagger \left\{ \sum_{n=0}^{N-1} \boldsymbol{\mathcal{N}}(n)[\boldsymbol{\alpha}(n-m) - \boldsymbol{\mu}_\alpha]^T \right\} \boldsymbol{B} \right|^2 \right\rangle \\
&= Var\{k_1^N(m)\} + \frac{1}{N^2\alpha^4} \sum_{n=0}^{N-1} \sum_{j=0}^{N-1} \sigma^2 \alpha^2 \delta_{nj} \\
&= Var\{k_1^N(m)\} + \frac{\sigma^2}{N\alpha^2}. \quad (3.7)
\end{aligned}$$

It shows that the total noise power in the estimate of the FID consists of a systematic noise term and a measurement noise term. The systematic noise is generally non-white. To avoid structural artifacts resulting from the systematic noise, it is necessary to find the right experimental setup so that the measurement noise is the dominant noise source. As in conventional FT-NMR, Equation 3.7 shows that the measurement noise term is inversely proportional to the total number of data points, N, used in the reconstruction. It will be shown in the next section that the systematic noise power is also inversely proportional to N, so that increasing N does not change the relative amount of systematic and measurement noise power. Hence, some other means must be sought to make the measurement noise become the dominant noise source.

Similarly, an estimator for the signal auto-covariance with the measurement noise

included is

$$\tilde{r}^N(m) = \frac{1}{N}\boldsymbol{B}^\dagger \left\{ \sum_{n=0}^{N-1} [\boldsymbol{M}(n) + \boldsymbol{\mathcal{N}}(n) - \boldsymbol{\mu}_M][\boldsymbol{M}(n-m) + \boldsymbol{\mathcal{N}}(n-m) - \boldsymbol{\mu}_M]^T \right\} \boldsymbol{B}. \tag{3.8}$$

The mean of this estimator is given by

$$\langle \tilde{r}^N(m) \rangle = \begin{cases} r(m) + \sigma^2 & \text{if } m = 0 \\ r(m) & \text{otherwise.} \end{cases} \tag{3.9}$$

The bias term is a delta function with height σ^2 at $m = 0$. The Fourier transform of $r(m)$ is the signal power spectrum, $S(\omega)$. Since the Fourier transform operator and the expectation operator are commutative, Fourier transform of both sides of the above equation gives

$$\langle \tilde{S}^N(\omega) \rangle = S(\omega) + \sigma^2 \tag{3.10}$$

where $\tilde{S}^N(\omega)$ is a noisy estimator for the signal power spectrum. Therefore, the bias term is just a DC offset in the signal power spectrum. The variance of the noisy estimator for the signal auto-covariance is

$$\begin{aligned} Var\{\tilde{r}^N(m)\} &= \begin{cases} \langle |\tilde{r}^N(m)|^2 \rangle - |r(m) + \sigma^2|^2 & \text{if } m = 0 \\ \langle |\tilde{r}^N(m)|^2 \rangle - |r(m)|^2 & \text{otherwise} \end{cases} \\ &= Var\{r^N(m)\} + \frac{\sigma^2(\sigma^2 + 2P)}{N} \end{aligned} \tag{3.11}$$

where P is the average signal power. Once again, the total noise power consists of a systematic noise term and a measurement noise term.

3.2 Systematic Noise in $k_1^N(m)$

The variance of $k_1^N(m)$, $Var\{k_1^N(m)\}$, can be obtained theoretically using Equations 3.2, 3.4 and the stochastic difference equation (Equation 2.4) for a specific excitation sequence. The steps are laborious, and the results cannot be expressed in simple closed

forms, but can be calculated numerically (see Appendix C). The numerical calculation has been done for random flip angle excitation using Gaussian white noise and random quadrature excitation using random binary sequences. The latter is also a special case of random phase excitation as discussed in the previous chapter. The variance has also been estimated by Monte Carlo simulations (see Chapter 1) for all three types of excitations using Gaussian white noise, or binary maximum length sequences (MLS).

Figure 3.1 shows the theoretically calculated variance of $k_1^N(m)$ with random flip angle excitation using Gaussian white noise for different values of N. For any given N, the variance approaches a constant value as m is increased. The constant value decreases by a factor of two for every doubling of N. This means that the variance is inversely proportional to N. The oscillation at small m has the same frequency as the resonance offset. Figure 3.2 shows the theoretically calculated variance of $k_1^N(m)$ with random quadrature excitation using zero mean random binary sequences for different values of N. The oscillation noted in Figure 3.1 is not present since the variance of $k_1^N(m)$ with random quadrature excitation is actually independent of the resonance offset. Figures 3.3 and 3.4 show comparisons of results obtained by theoretical calculation and Monte Carlo simulations for the two different types of excitations. All figures show good agreement. For the random flip angle excitation the variance of $k_1^N(m)$ behaves differently at small m for lines on- and off-resonance (Figure 3.3), but it approaches to the same constant value.

As shown in Figures 3.1 and 3.2 the variance of $k_1^N(m)$ is a function of m, but it is reasonably flat for a large range of m. Define the systematic noise power as the average variance:

$$\begin{aligned} \text{Systematic Noise Power} &= \frac{1}{M}\sum_{m=0}^{M-1} Var\{k_1^N(m)\} \\ &\xrightarrow{M\to\infty} Var\{k_1^N(\infty)\}, \end{aligned} \tag{3.12}$$

where $Var\{k_1^N(\infty)\}$ is well defined and is inversely proportional to N as shown in

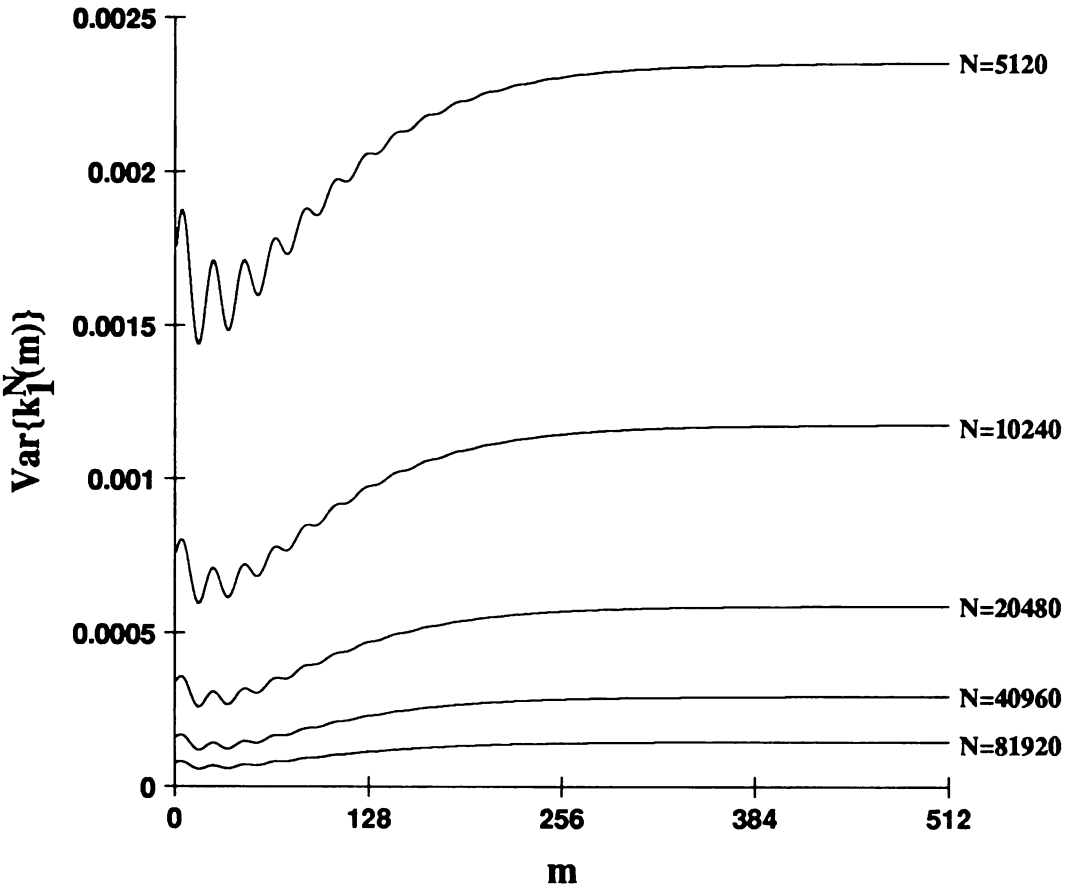

Figure 3.1: Theoretically calculated variance of $k_1^N(m)$ with random flip angle excitation using Gaussian white noise. $T_1 = 0.5$s, $T_2 = 10$ms, $T_R = 0.1$ms, $\nu = 250$Hz and RMS flip angle of 1.15°.

Figures 3.1 and 3.2. From Chapter 2 $K_1(\omega)$ is Lorentzian when the excitation power is low. This implies that $k_1(m)$ is an exponentially decaying sinusoid (Figure 3.5) with an amplitude $|k_1(0)|$. Define the signal-to-systematic-noise ratio as

$$(S/N)_{sn} = \frac{|k_1(0)|^2}{Var\{k_1^N(\infty)\}}, \tag{3.13}$$

where the subscript sn means systematic noise. Figure 3.6 shows a log-log plot of the signal-to-systematic-noise ratio versus N for random phase excitation obtained by Monte Carlo simulations. The plot shows once again that the systematic noise power is inversely proportional to N. Figures 3.7 and 3.8 are corresponding plots for random

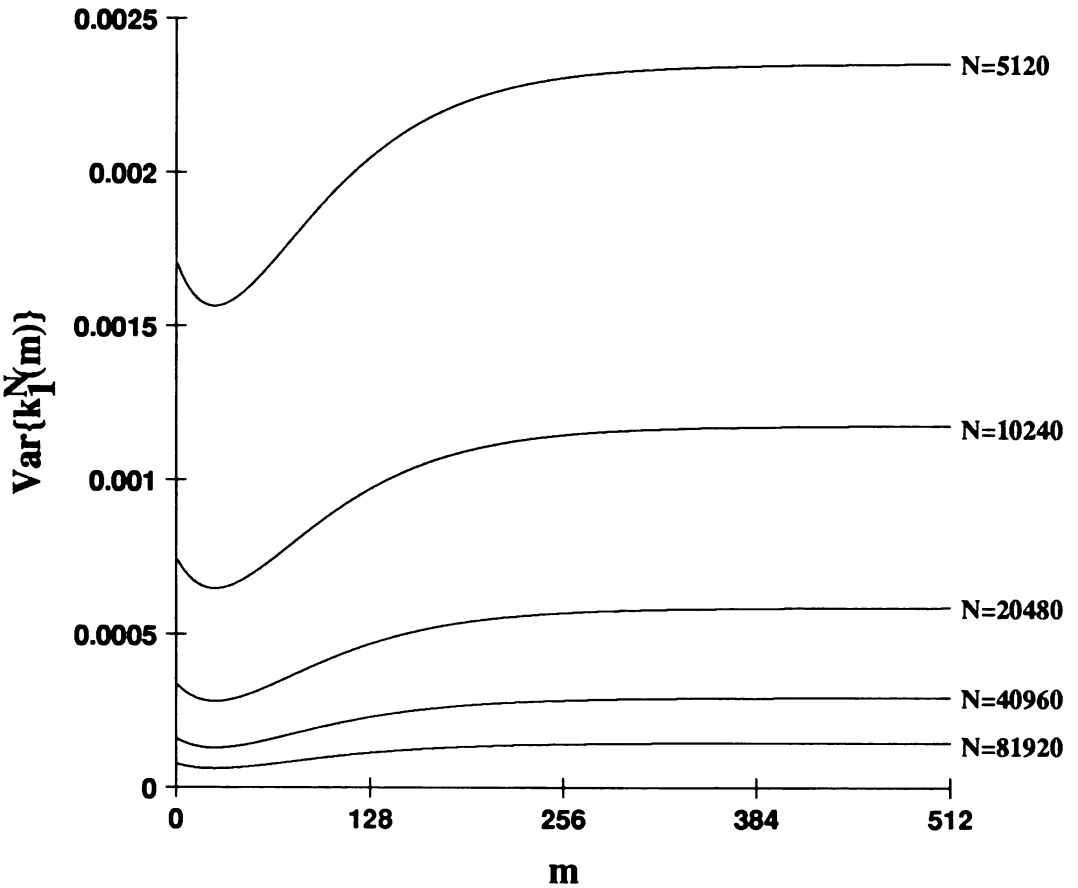

Figure 3.2: Theoretically calculated variance of $k_1^N(m)$ with random quadrature excitation using a zero mean random binary sequence. $T_1 = 0.5$s, $T_2 = 10$ms, $T_R = 0.1$ms, $\nu = 250$Hz and RMS flip angle of 1.15°.

flip angle excitation and random quadrature excitation, but for three different types of excitation sequences. Figures 3.7a and 3.8a are obtained with Gaussian white noise, Figures 3.7b and 3.8b with sub-sequences generated by a 31-bit MLS generator and Figures 3.7c and 3.8c with sub-sequences generated by a 15-bit MLS generator. A sub-sequence here means a small section of the full MLS. The length of the sub-sequences generated by the 31-bit MLS generator is much smaller than $2^{31} - 1$, the period of the generator. Such sub-sequences behave just like random binary sequences, resulting in a plot very similar to that for the Gaussian white noise. However, it is very interesting to notice from Figures 3.7c and 3.8c that the signal-to-systematic-noise ratio does not

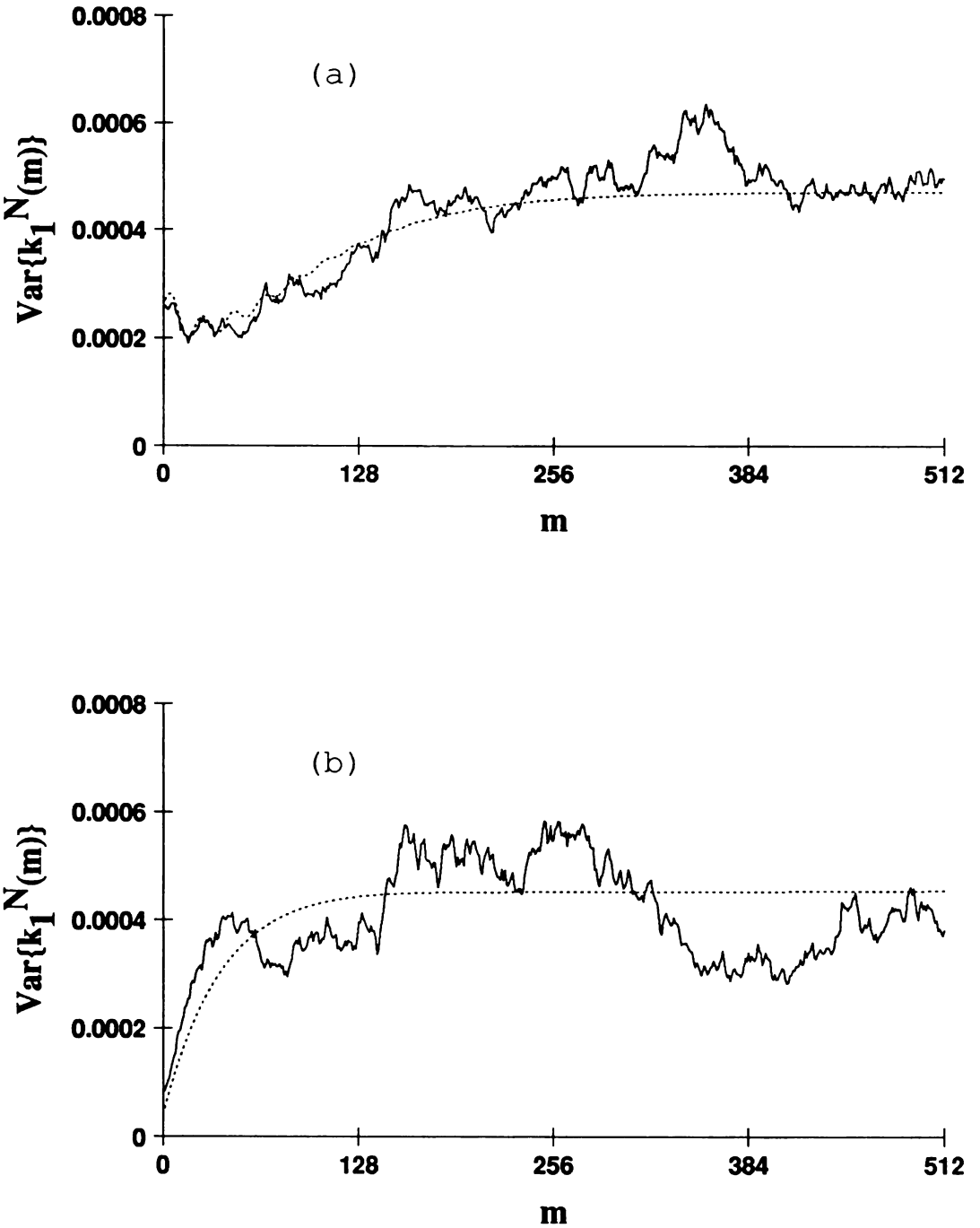

Figure 3.3: Variance of $k_1^N(m)$ with random flip angle excitation using Gaussian white noise. Dotted curve is theoretical calculation, solid curve is Monte Carlo simulation. $T_1 = 0.5$s, $T_2 = 10$ms, $T_R = 0.1$ms, $N = 25600$ and RMS flip angle of 1.15°. (a) $\nu = 250$Hz, (b) $\nu = 0$Hz.

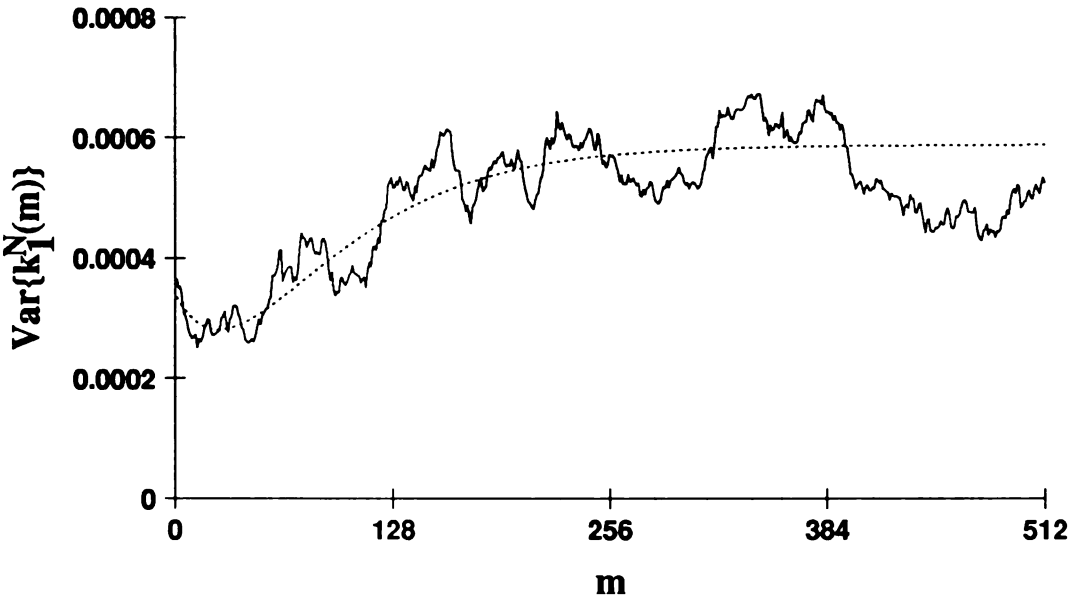

Figure 3.4: Variance $k_1^N(m)$ with random quadrature excitation using a zero mean random binary sequence. Dotted curve is theoretical calculation, solid curve is Monte Carlo simulation. $T_1 = 0.5$s, $T_2 = 10$ms, $T_R = 0.1$ms, $\nu = 250$Hz, $N = 20480$ and RMS flip angle of 1.15°.

follow the $1/N$ behavior whenever N is a multiple of $2^{15} - 1$, the period of the 15-bit generator. The signal-to-systematic-noise ratio for MLS excitation with N equal to a multiple of the period of the MLS is about 20dB higher than that for Gaussian white noise excitation with the same N. Such desirable behavior is a consequence of the autocorrelation of the complete MLS being a delta function with a small negative offset. This is one reason why the Hadamard transform, which applies to the full MLS, is so popular in linear system analysis.

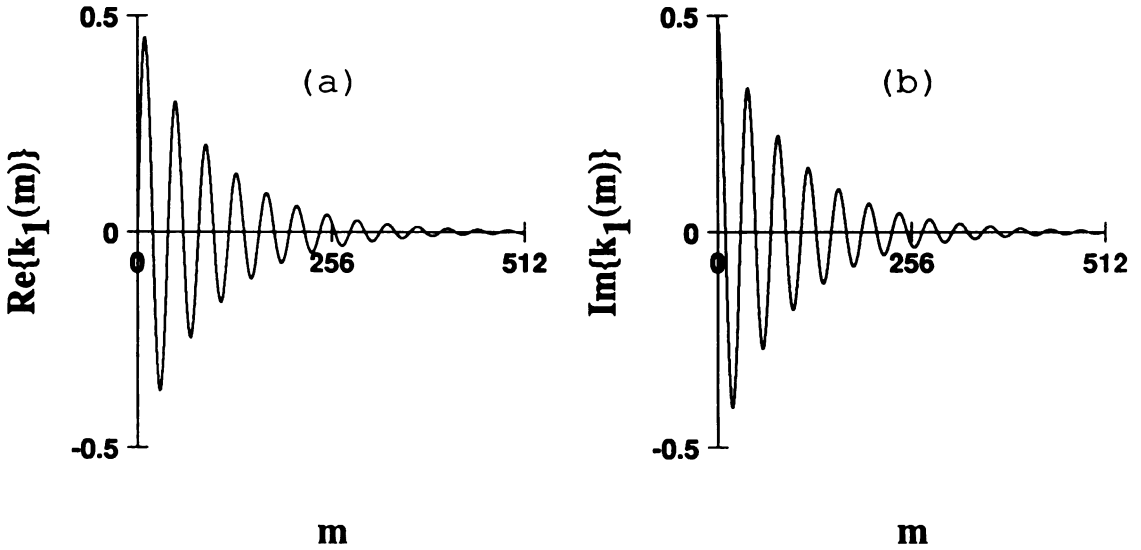

Figure 3.5: (a) Real part and (b) imaginary part of $k_1(m)$ with random flip angle excitation using Gaussian white noise. $T_1 = 0.5$s, $T_2 = 10$ms, $T_R = 0.1$ms, $\nu = 250$Hz, and RMS flip angle of 1.15°.

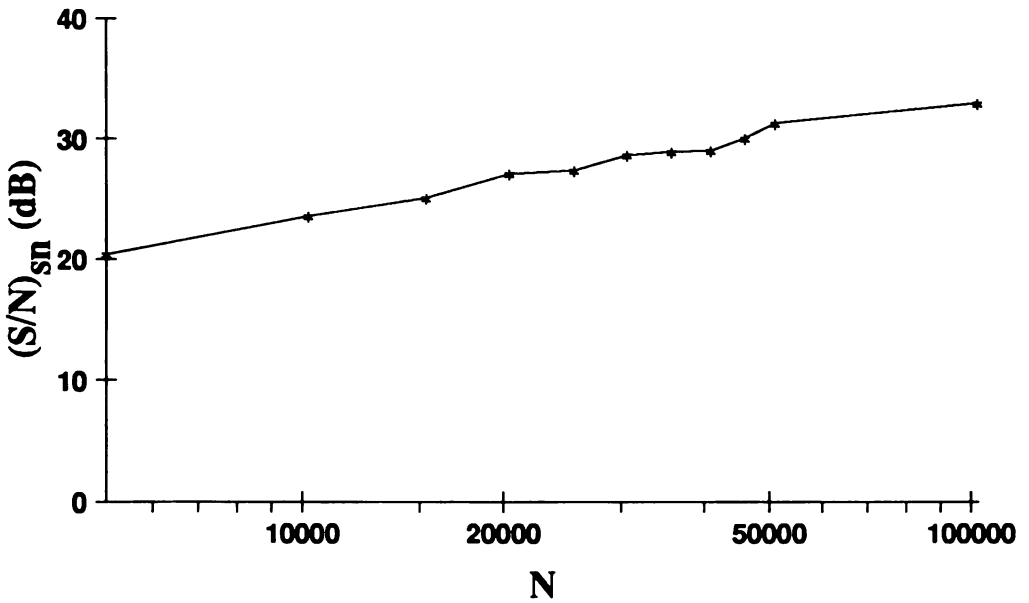

Figure 3.6: Log-log plot of signal-to-systematic-noise ratio of $k_1^N(m)$ versus N, obtained by Monte Carlo simulations with random phase excitations. $T_1 = 0.5$s, $T_2 = 10$ms, $T_R = 0.1$ms, $\nu = 250$Hz, and RMS flip angle of 1.15°.

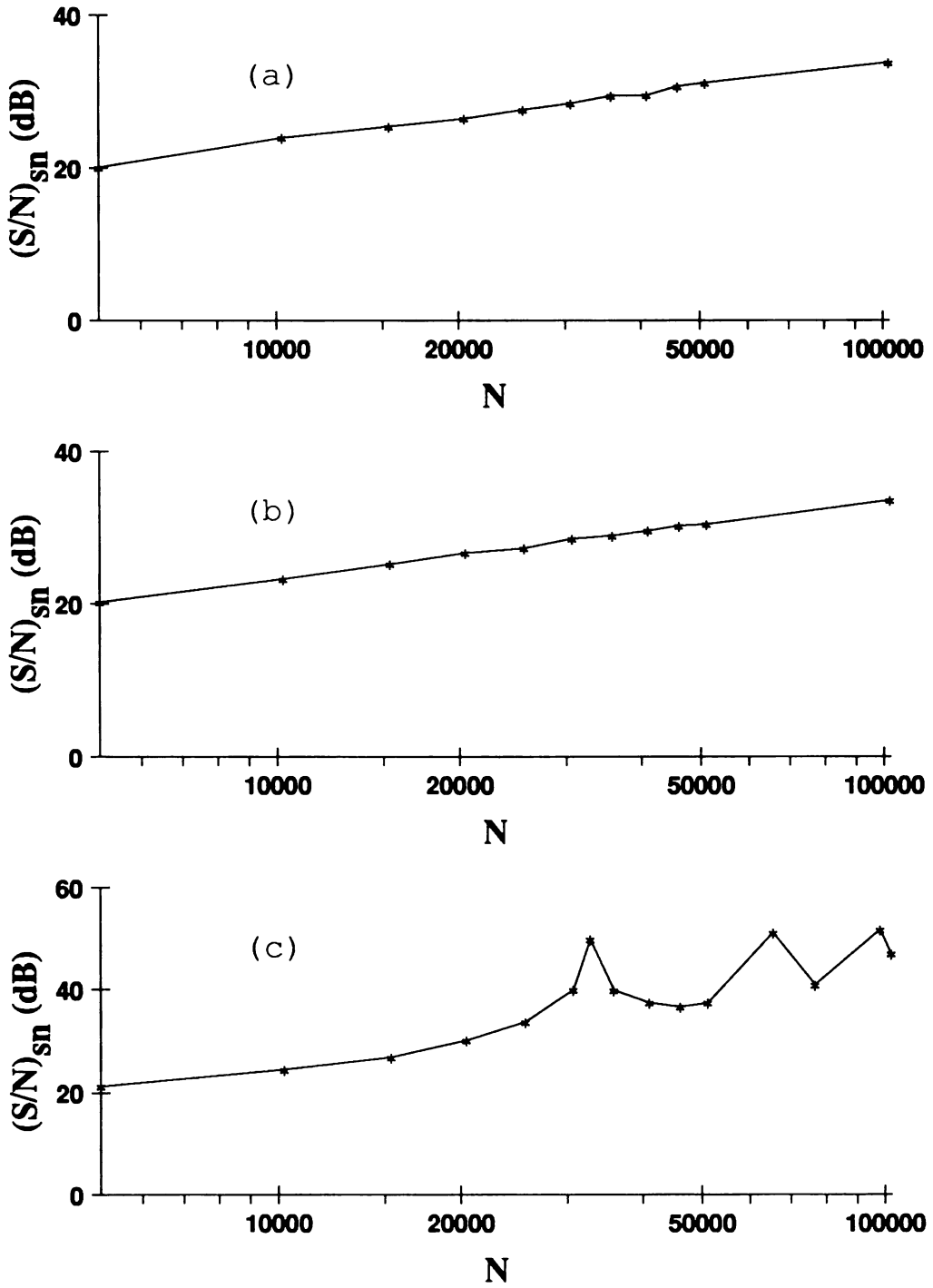

Figure 3.7: Log-log plot of signal-to-systematic-noise ratio of $k_1^N(m)$ versus N, obtained by Monte Carlo simulations with random flip angle excitations. The excitation sequences are (a) Gaussian white noise, (b) 31-bit MLS and (c) 15-bit MLS. $T_1 = 0.5$s, $T_2 = 10$ms, $T_R = 0.1$ms, $\nu = 250$Hz, and RMS flip angle of 1.15°.

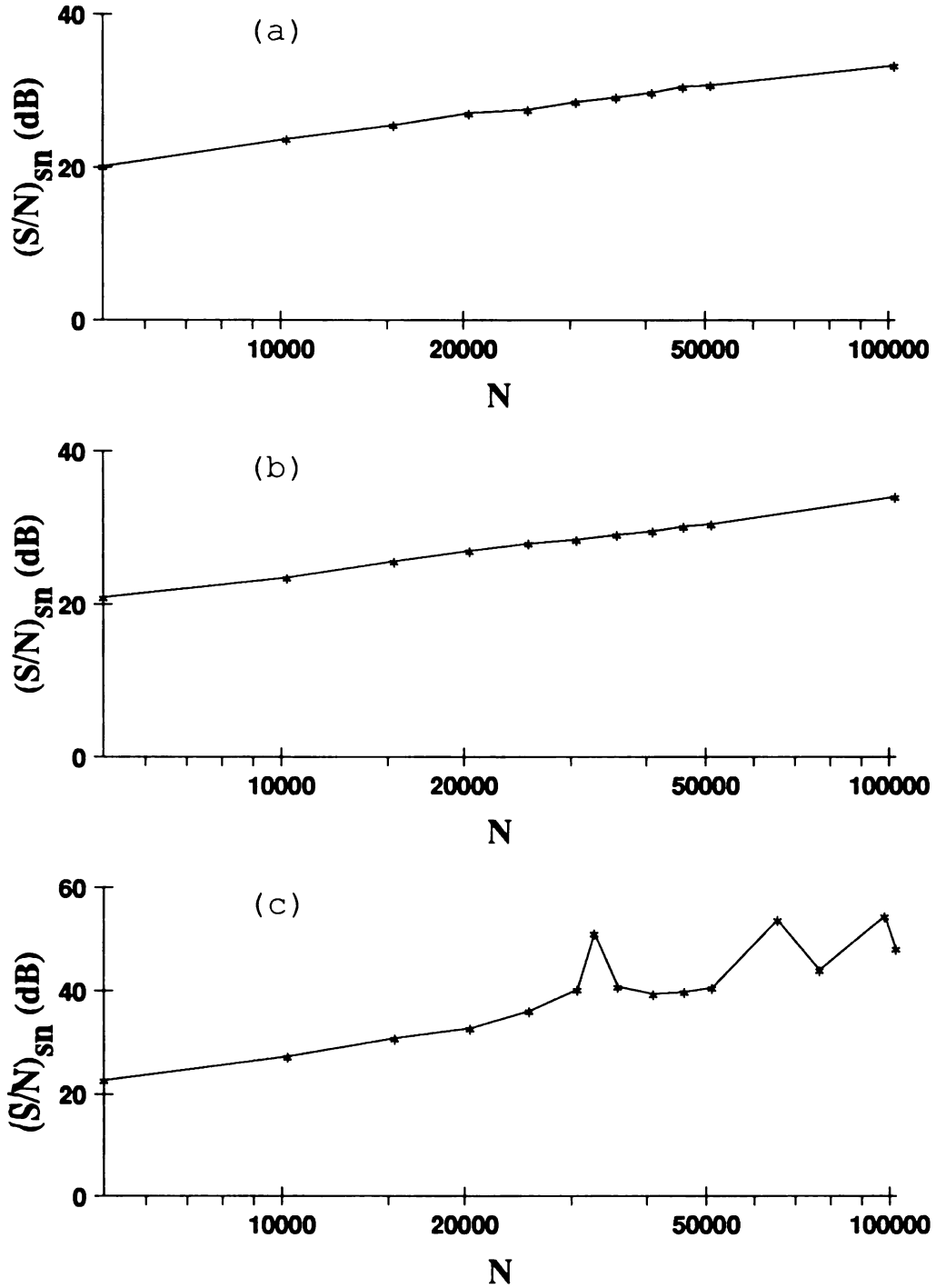

Figure 3.8: Log-log plot of signal-to-systematic-noise ratio of $k_1^N(m)$ versus N, obtained by Monte Carlo simulations with random quadrature excitations. The excitation sequences are (a) Gaussian white noise, (b) 31-bit MLS and (c) 15-bit MLS. $T_1 = 0.5$s, $T_2 = 10$ms, $T_R = 0.1$ms, $\nu = 250$Hz, and RMS flip angle of 1.15°.

3.3 Systematic Noise in $r^N(m)$

Theoretical calculation of the variance of $r^N(m)$ is more formidable than that for the variance of $k_1^N(m)$. Results obtained by Monte Carlo simulations will be presented. Figure 3.9 is a plot of computer simulated $Var\{r^N(m)\}$. As a function of m, it is very similar to $Var\{k_1^N(m)\}$. For $r^N(m)$, define the systematic noise power as the average variance:

$$\begin{aligned} \text{Systematic Noise Power} &= \frac{1}{M}\sum_{m=0}^{M-1} Var\{r^N(m)\} \\ &\xrightarrow{M\to\infty} Var\{r^N(\infty)\}, \end{aligned} \tag{3.14}$$

where $Var\{r^N(\infty)\}$ is well defined. The analysis in the previous chapter showed that the signal power spectrum is very similar to $K_1(\omega)$. This means that the signal auto-covariance function, $r^N(m)$, is very similar to the input-output cross-covariance, $k_1^N(m)$, i.e., $r^N(m)$ should also look like an exponentially decaying sinusoid. The amplitude of this sinusoid is $r^N(0)$ which is real and becomes the average signal power P when N approaches infinity. Therefore, for the signal auto-covariance $r^N(m)$, the signal-to-systematic-noise ratio is defined as

$$(S/N)_{sn} = \frac{P^2}{Var\{r_1^N(\infty)\}}. \tag{3.15}$$

Figures 3.10, 3.11 and 3.12 are log-log plots of the signal-to-systematic-noise ratio versus N for the three different types of excitations obtained by Monte Carlo simulations. They show that the systematic noise power is again inversely proportional to N when the excitation sequence is a Gaussian white noise or a binary sequence generated by a 31-bit MLS generator. Once again, with the 15-bit MLS, the systematic noise power drops significantly when N is a multiple of the period of the MLS. Comparing the corresponding plots (Figures 3.6, 3.7 and 3.8) of signal-to-systematic-noise ratio versus N for $k_1^N(m)$, the signal-to-systematic-noise ratio for $r^N(m)$ is generally about 2dB to 3dB lower than that for $k_1^N(m)$ for a given N and a given type of excitation. When a 15-bit

MLS generator is used and N is a multiple of $2^{15}-1$, the drop is about 6dB lower. This is one disadvantage of using the signal power spectrum to approximate the true spectrum.

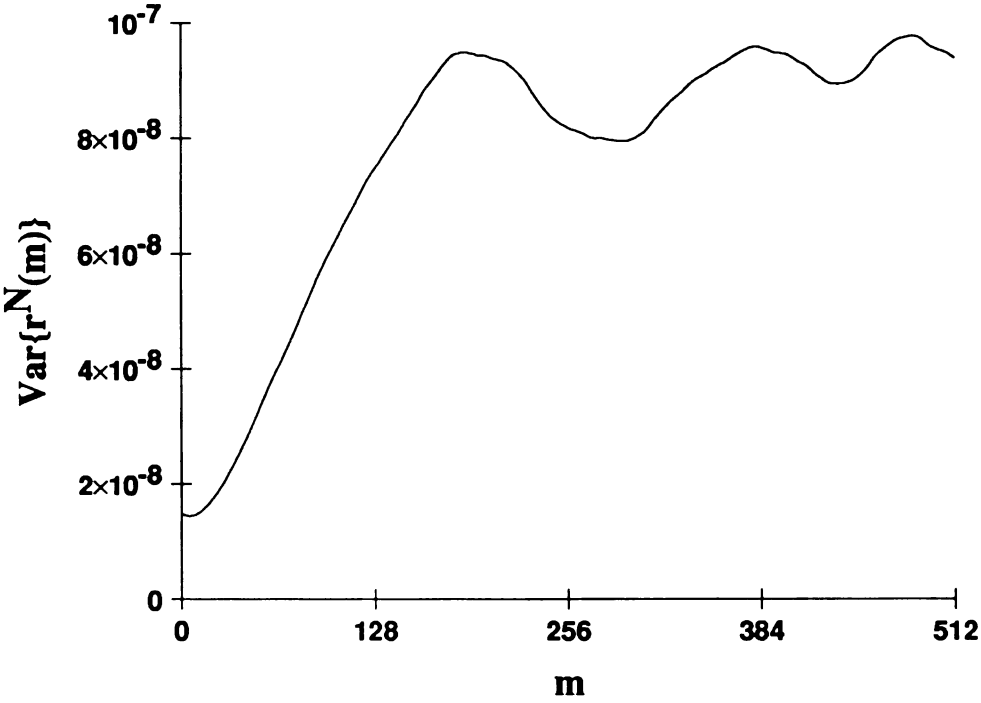

Figure 3.9: Monte Carlo simulated variance of $r^N(m)$ with random quadrature excitation using a Gaussian white noise sequence. $T_1 = 0.5$s, $T_2 = 10$ms, $T_R = 0.1$ms, $\nu = 250$Hz, $N = 25600$ and the RMS flip angle is 1.15°.

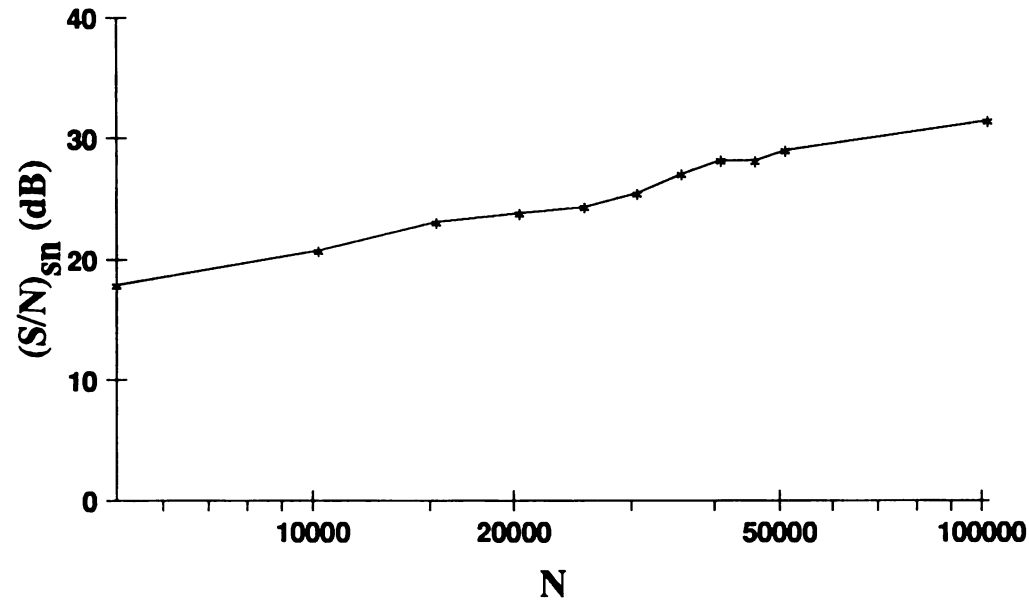

Figure 3.10: Log-log plot of signal-to-systematic-noise ratio of $r^N(m)$ versus N, obtained by Monte Carlo simulations with random phase excitations. $T_1 = 0.5$s, $T_2 = 10$ms, $T_R = 0.1$ms, $\nu = 250$Hz, and RMS flip angle of 1.15°.

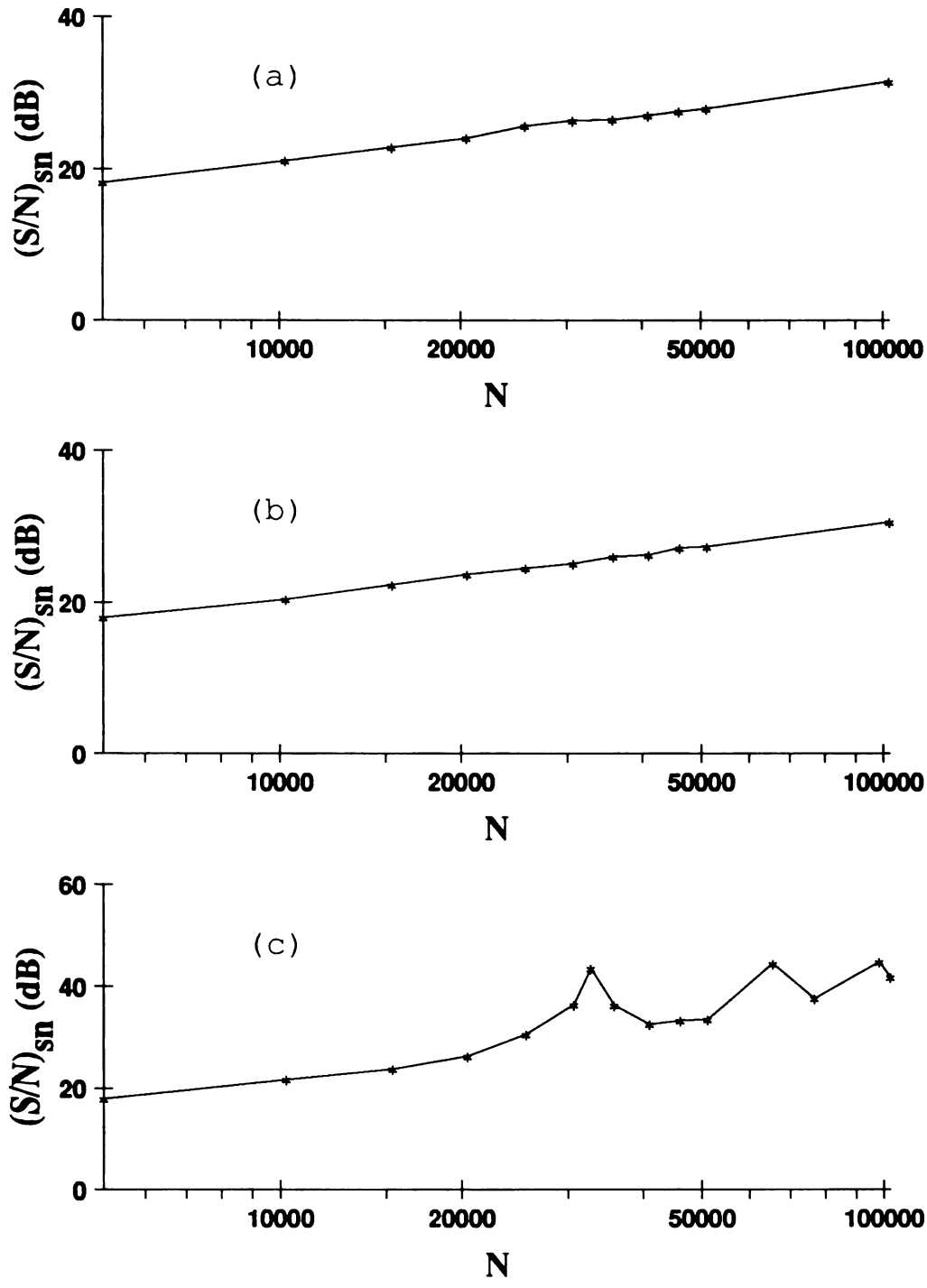

Figure 3.11: Log-log plot of signal-to-systematic-noise ratio of $r^N(m)$ versus N, obtained by Monte Carlo simulations with random flip angle excitations. The excitation sequences are (a) Gaussian white noise, (b) 31-bit MLS and (c) 15-bit MLS. $T_1 = 0.5$s, $T_2 = 10$ms, $T_R = 0.1$ms, $\nu = 250$Hz, and RMS flip angle of 1.15°.

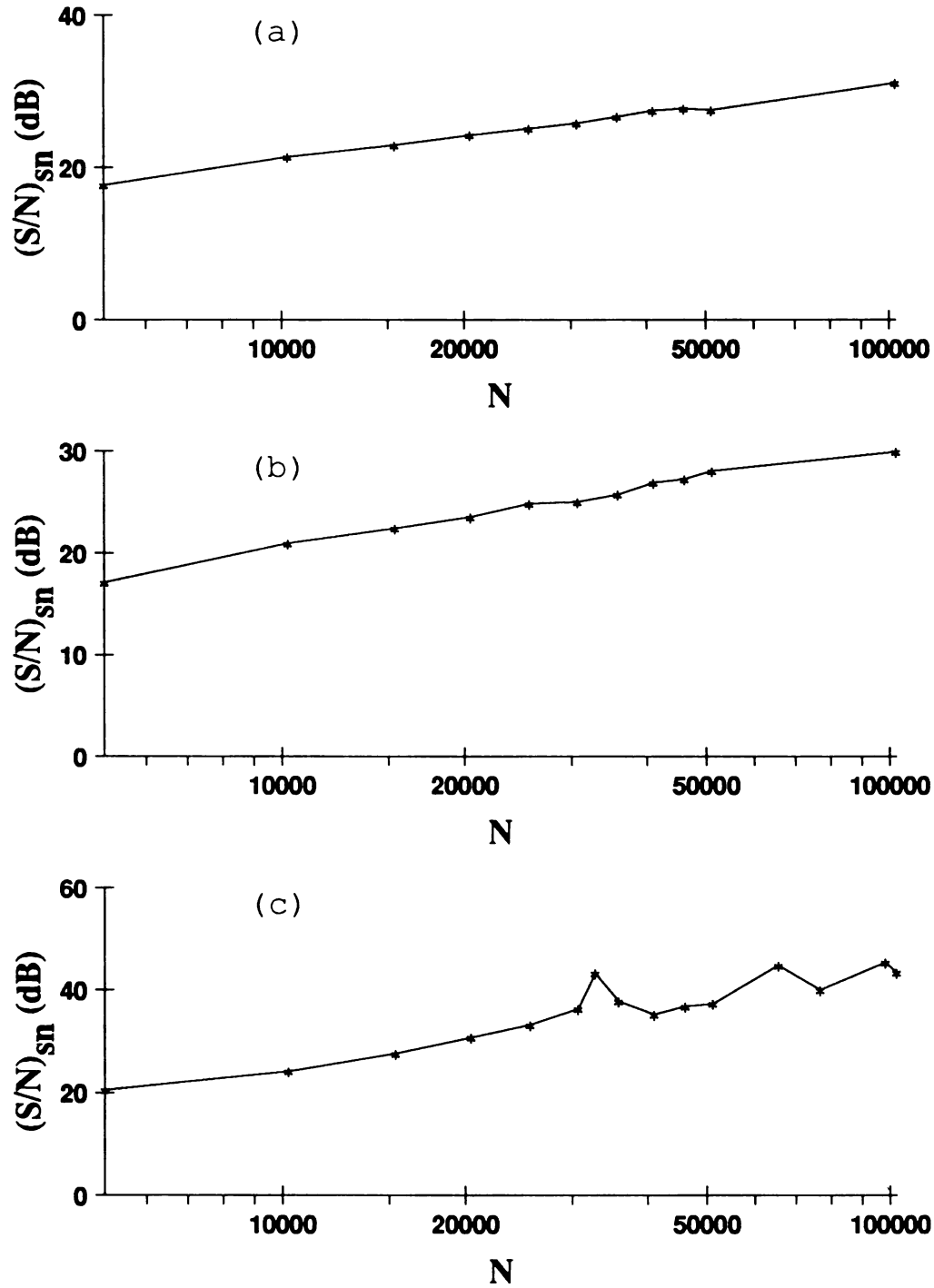

Figure 3.12: Log-log plot of signal-to-systematic-noise ratio of $r^N(m)$ versus N, obtained by Monte Carlo simulations with random quadrature excitations. The excitation sequences are (a) Gaussian white noise, (b) 31-bit MLS and (c) 15-bit MLS. $T_1 = 0.5$s, $T_2 = 10$ms, $T_R = 0.1$ms, $\nu = 250$Hz, and RMS flip angle of 1.15°.

3.4 Nonlinear Systematic Noise With MLS Excitations

The closed form expression of $K_1(\omega)$ obtained in Chapter 2 predicts only two types of spectral distortion: a line broadening and/or non-uniform response across the spectrum. However, in 1982 Blümich and Ziessow [14] showed that noise-like distortion occurs in the reconstructed spectra when a high power MLS excitation is used. They attributed the distortions to linear processing of a nonlinear spin response and used a heuristic ansatz for the Volterra kernels to describe the distortions. The following analysis will show that the distortions are actually due to characteristics of the MLS which manifest themselves in $k_1(m)$ and $K_1(\omega)$ only when the spin system is driven to a nonlinear regime with high excitation power.

Figure 3.13 shows Monte Carlo simulated line shapes of $K_1(\omega)$ for random flip angle excitation using zero mean binary MLS. As the RMS flip angle is increased, there is an increase in the relative amount of noise-like distortion in addition to line broadening and a notch artifact. This agrees with Blümich and Ziessow's experimental observations. The systematic noise due to the variance of $k_1(m)$ in these plots should be negligible since N(=512000) is very large. Figure 3.14 shows that there is less noise-like distortion when a Gaussian white noise generator is used. A comparison of $k_1(m)$ generated with MLS and Gaussian white noise in Figure 3.15 shows that the noise-like distortion with MLS excitation are actually due to spurious components at $m = 62, 143$ and 255. Theoretical results for a truly random binary sequence obtained in the previous chapter do not predict such spurious components. They are artifacts resulting from peculiar properties of the MLS.

A random binary sequence $\alpha(n)$ that takes on the equally likely values of ± 1 should have a zero third order auto-correlation:

$$\langle \alpha(n)\,\alpha(n-i)\,\alpha(n-j) \rangle \equiv 0. \tag{3.16}$$

A plot of $\langle \alpha(n)\,\alpha(n-i)\,\alpha(n-j) \rangle$ calculated numerically over a range of i and j for

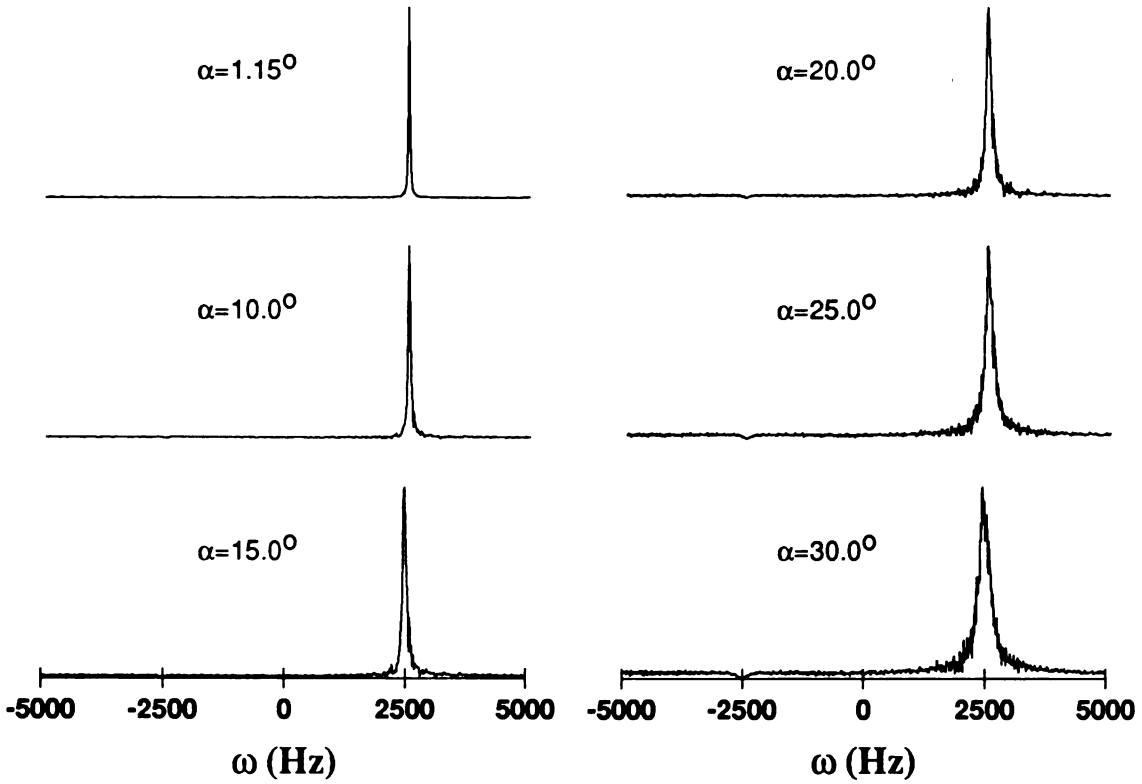

Figure 3.13: Monte Carlo simulated line shapes of $K_1(\omega)$ for random flip angle excitation with sub-sequences generated by a 31-bit MLS generator. $T_1 = 0.5$s, $T_2 = 10$ms, $T_R = 0.1$ms, $\nu = 2500$Hz and $N = 512000$.

a sub-sequence generated by a 31-bit MLS generator shows that the third order auto-correlation is almost zero everywhere except at (i, j) = (3,31), (31,3), (6,62), (62,6), (12,124) and (124,12) (Figure 3.16). At these points the third order auto-correlation has a value of 1. The spikes at (6,62) and (62,6) are clearly related to the spurious component of $k_1(m)$ at $m = 62$.

The fact that a spike occurs at $(31, 3)$ is a direct consequence of the algorithm used by the 31-bit MLS generator. Figure 3.17 is a block diagram of the 31-bit MLS generator. The generator consists of a 31-bit shift register with the exclusive-OR of the 31^{st} bit and the 3^{rd} bit fed back to form the 0^{th} bit, the bit at the input of the register SR1. Therefore the 0^{th}, 3^{rd} and 31^{st} bits of the MLS generated are perfectly correlated, giving rise to

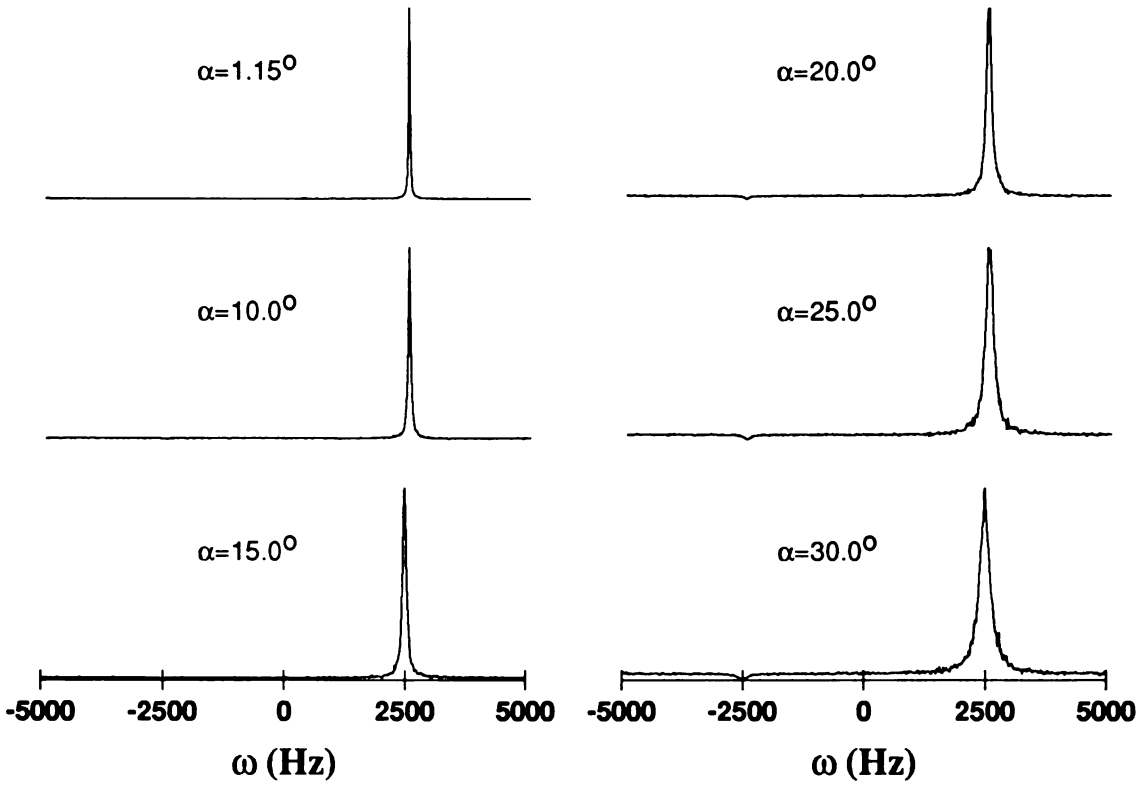

Figure 3.14: Monte Carlo simulated line shapes of $K_1(\omega)$ for random flip angle excitation with sequences generated by a Gaussian white noise generator. $T_1 = 0.5$s, $T_2 = 10$ms, $T_R = 0.1$ms, $\nu = 2500$Hz and $N = 512000$.

the spikes at (31,3) and (3,31). Similarly, the 1^{st}, 4^{th} and 32^{nd} bits are also perfectly correlated. By propagating this triplet along the sequence, it can be shown that the 0^{th}, 6^{th} and 62^{nd} bits are also perfectly correlated, giving rise to the spikes at (62,6) and (6,62). This indicates that the spikes are MLS generator dependent and are not due to the use of sub-sequences. No erroneous spikes occur in the third order auto-correlation of a sequence generated by the Gaussian white noise generator (Figure 3.18).

The fourth order auto-correlation is

$$\langle \alpha(n)\,\alpha(n-i)\,\alpha(n-j)\,\alpha(n-l)\rangle = 0 \tag{3.17}$$

when l is strictly bigger than i and j. Figures 3.19 and 3.20 are plots of the fourth order auto-correlation calculated numerically for a sub-sequence generated by a 31-bit MLS

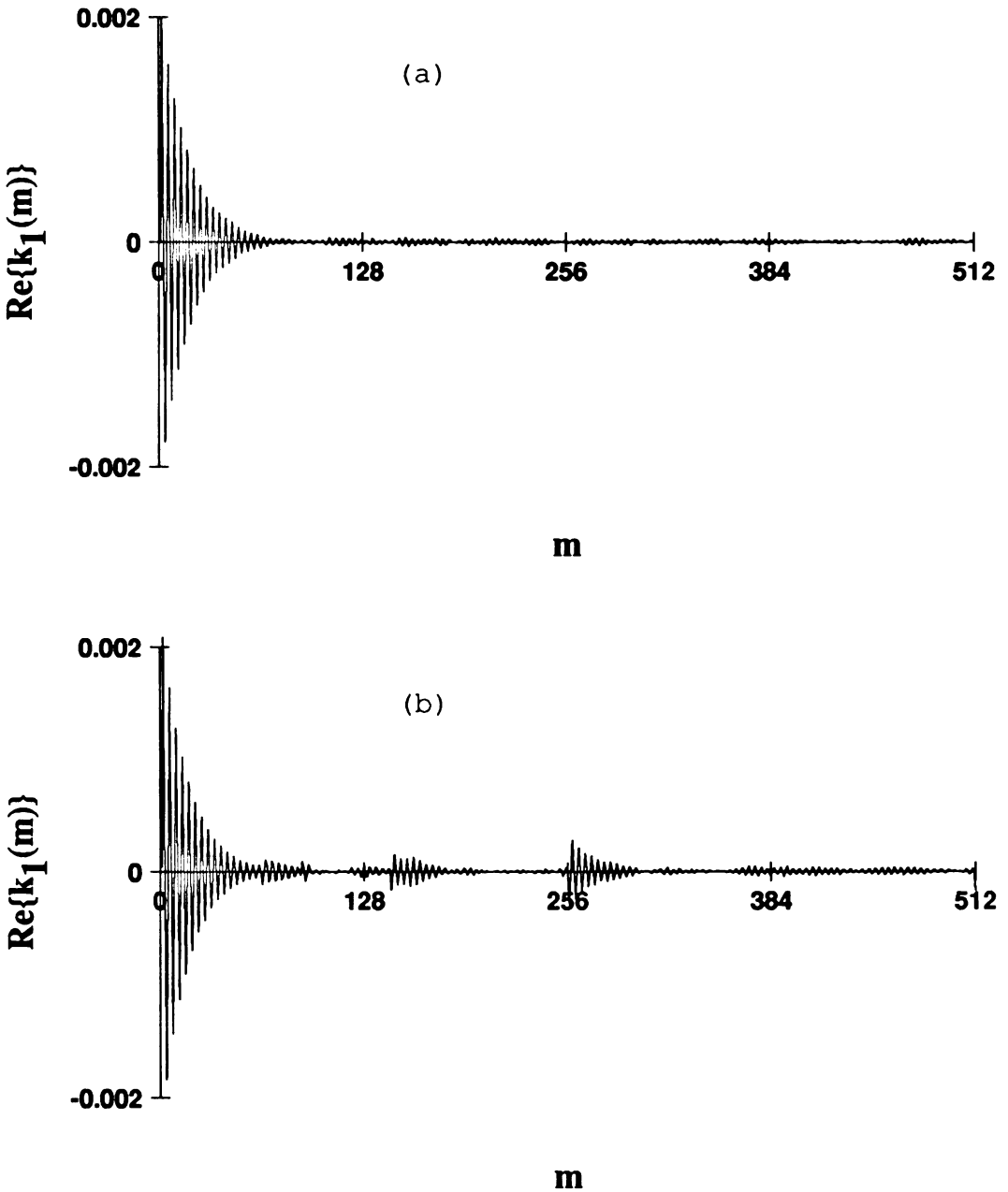

Figure 3.15: Monte Carlo simulated real part of $k_1(m)$ for random flip angle excitation with sub-sequences generated by (a) a Gaussian white noise generator and (b) a 31-bit MLS generator. $T_1 = 0.5$s, $T_2 = 10$ms, $T_R = 0.1$ms, $\nu = 2500$Hz, $\alpha = 25°$ and $N = 512000$.

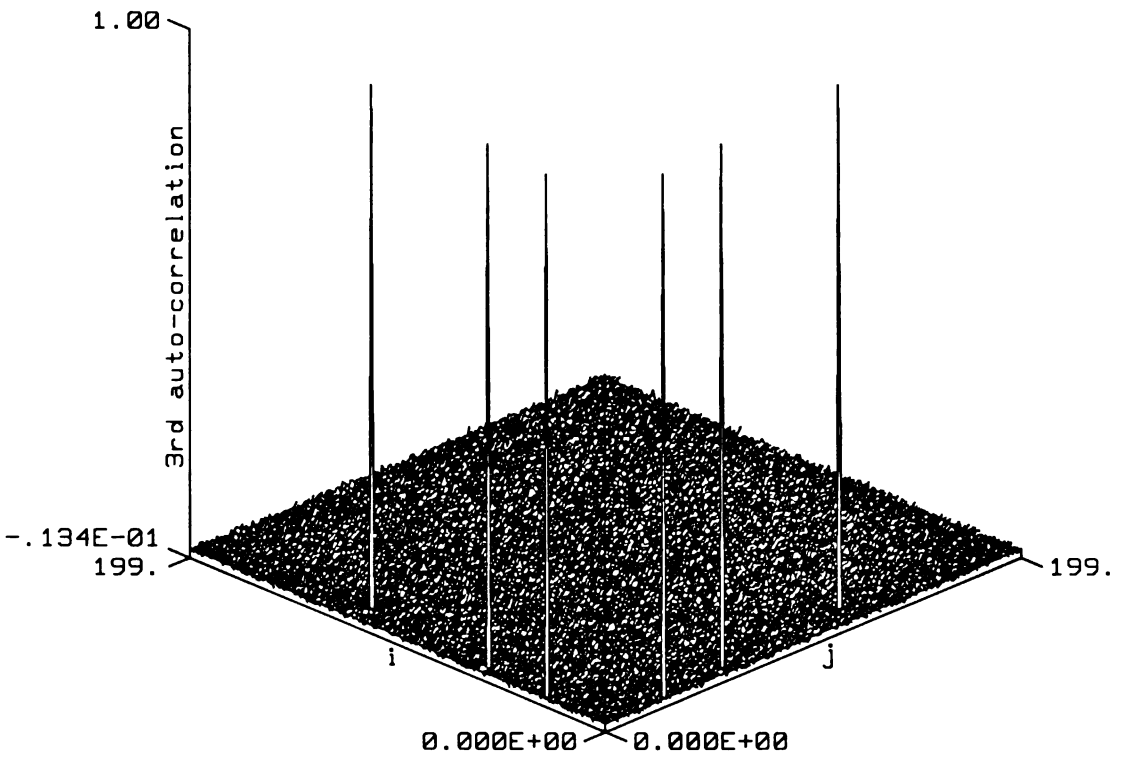

Figure 3.16: Numerically calculated third order auto-correlation of a sub-sequence generated by a 31-bit MLS generator. The sequence takes on the values ± 1. $N = 20000$.

generator with l being 143 and 255, respectively. The plots show spikes at (i, j, l) = (3,19,143), (19,3,143), (3,7,255) and (7,3,255). These spikes are clearly related to the spurious components of $k_1(m)$ at $m = 143$ and 255. Figure 3.21 is a plot of the fourth order auto-correlation with $l = 100$. Expected spikes occur at (i, j, l) = (100,0,100) and (0,100,100) and there are no erroneous spikes. Therefore, there is no spurious component of $k_1(m)$ at $m = 100$. The reason for a spike at (3,19,143) is similar to the reason for the spike at (62,6) of the third order auto-correlation. The 0^{th}, 3^{rd}, 19^{th} and 143^{rd} bits are perfectly correlated due to the propagation of the perfectly correlated triplet, the 0^{th}, 3^{rd} and 31^{st} bits.

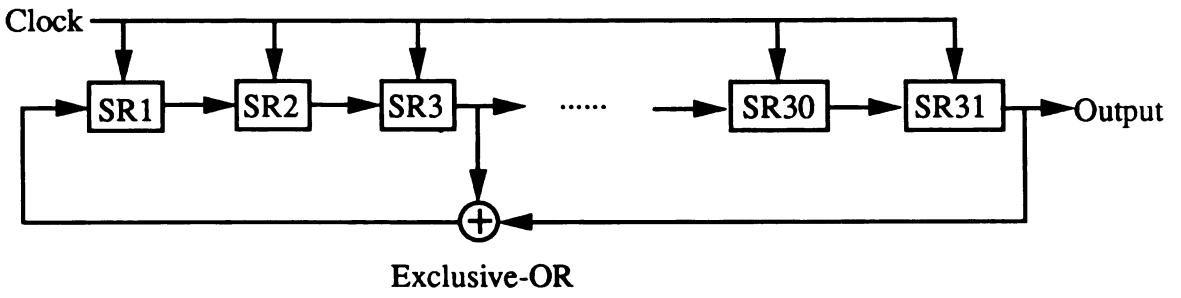

Figure 3.17: A 31-bit MLS generator implemented with a 31-bit shift register.

The auto-correlations of orders higher than two are related to the nonlinear components of the magnetization response. Consider the random flip angle excitation experiment, wherein the magnetization response can be written as a Volterra series:

$$\begin{aligned} M_{xy}(n) &= h_0 + \sum_{i=0}^{n} h_1(i)\,\alpha(n-i) + \sum_{i=0}^{n}\sum_{j=0}^{n} h_2(i,j)\,\alpha(n-i)\,\alpha(n-j) \\ &\quad + \sum_{i=0}^{n}\sum_{j=0}^{n}\sum_{l=0}^{n} h_3(i,j,l)\,\alpha(n-i)\,\alpha(n-j)\,\alpha(n-l) + \cdots, \end{aligned} \tag{3.18}$$

where h_i is the i^{th} order Volterra kernel. For a zero mean excitation sequence $\alpha(n)$, the input-output cross-correlation is given by

$$\begin{aligned} k_1(m) &= \frac{1}{\alpha^2}\langle M_{xy}(n)\,\alpha(n-m)\rangle \\ &= h_1(m) + \frac{1}{\alpha^2}\sum_{i=0}^{n}\sum_{j=0}^{n} h_2(i,j)\langle\alpha(n-i)\,\alpha(n-j)\,\alpha(n-m)\rangle \\ &\quad + \frac{1}{\alpha^2}\sum_{i=0}^{n}\sum_{j=0}^{n}\sum_{l=0}^{n} h_3(i,j,l)\langle\alpha(n-i)\,\alpha(n-j)\,\alpha(n-l)\,\alpha(n-m)\rangle. \end{aligned} \tag{3.19}$$

A truly random binary sequence will have a zero third order auto-correlation and so the second order Volterra kernel does not contribute to $k_1(m)$. When $\alpha(n)$ is a subsequence generated by the 31-bit MLS generator in Figure 3.17, the spikes in the third order auto-correlation will give rise to terms depending on the second order Volterra kernel in Equation 3.19. For example, consider the spikes at (i,j) = (6,62) and (62,6),

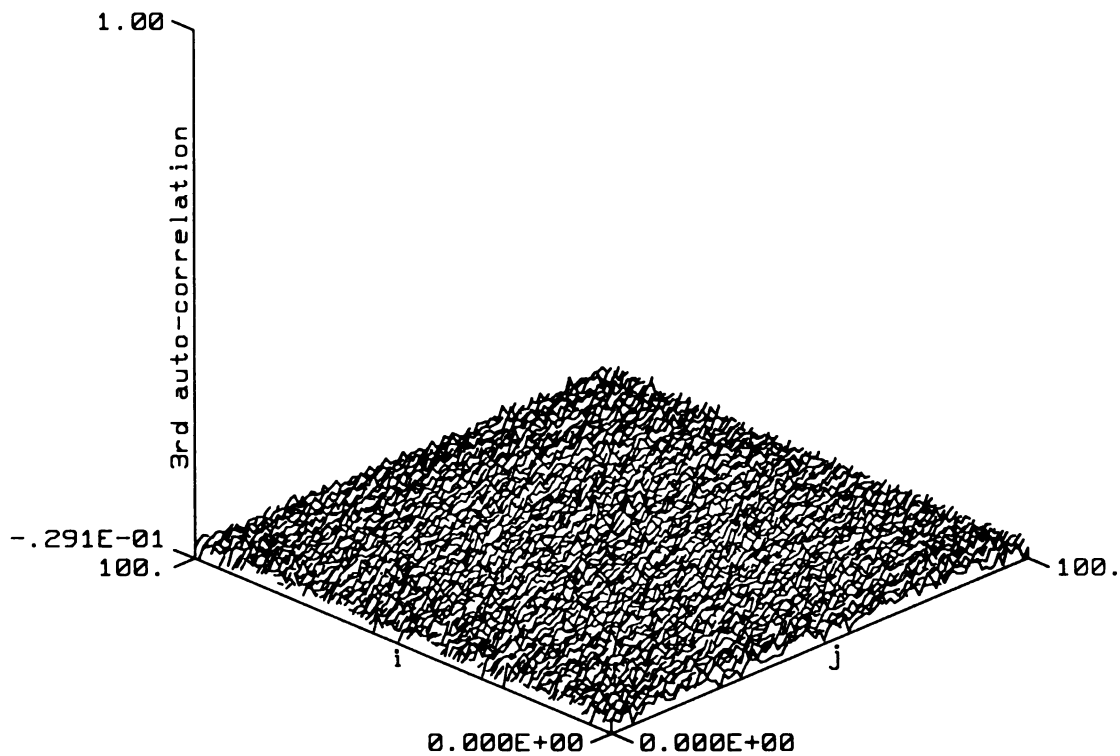

Figure 3.18: Numerically calculated third order auto-correlation of a sub-sequence generated by a Gaussian white noise generator. The sequence has a variance of 1. $N = 10000$.

they will contribute the following terms to $k_1(m)$:

$$\alpha \left[h_2(m+6, m+62) + h_2(m+62, m+6) + h_2(m-6, m+56) \right.$$
$$\left. + h_2(m+56, m-6) + h_2(m-56, m-62) + h_2(m-62, m-56) \right] . \quad (3.20)$$

The spin system is a causal system and so $h_2(i,j)$ is zero whenever i or j is negative. This implies that the terms $h_2(m-56, m-62)$ and $h_2(m-62, m-56)$ do not contribute to $k_1(m)$ until m is bigger than or equal to 62. This explains the spurious component of $k_1(m)$ at $m = 62$. Similarly, the various unexpected spikes in the fourth order auto-correlation will generate terms like $h_3(m-140, m-124, m-143)$ and

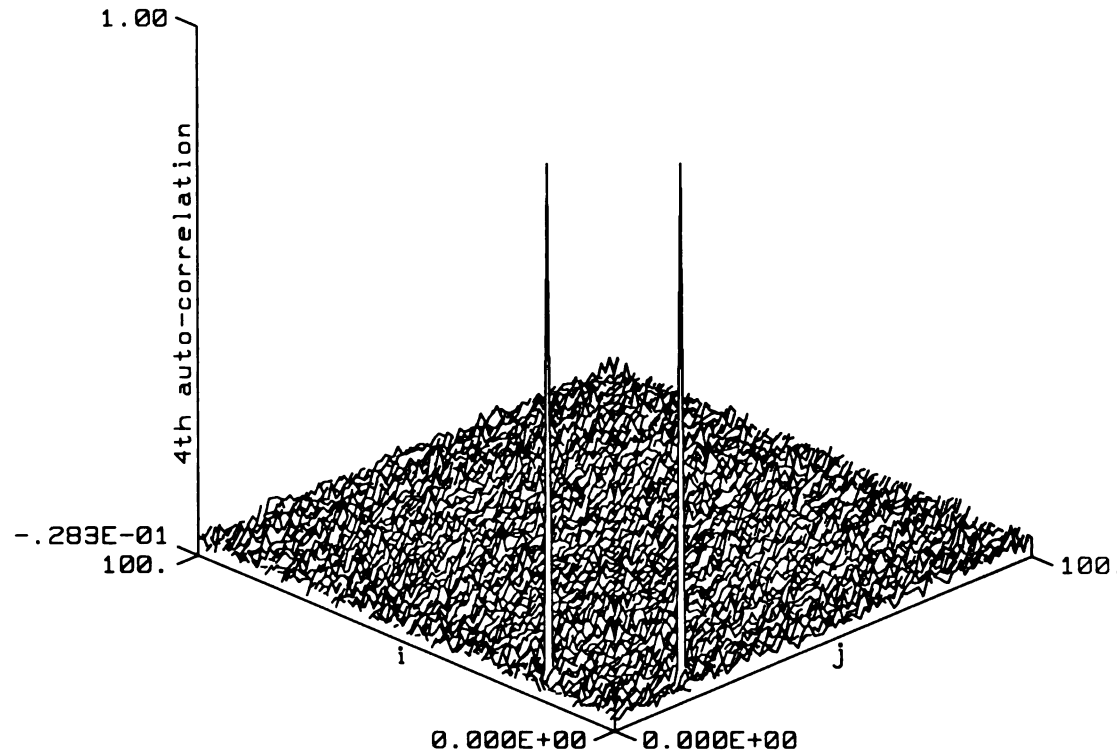

Figure 3.19: Numerically calculated fourth order auto-correlation of a sub-sequence generated by a 31-bit MLS generator, $\langle \alpha(n)\,\alpha(n-i)\,\alpha(n-j)\,\alpha(n-143) \rangle$. The sequence takes on the values ± 1. $N = 10000$.

$h_3(m-140, m-137, m-255)$ that give rise to the spurious components of $k_1(m)$ at $m = 143$ and $m = 255$. When the excitation power is low, the magnetization response is linear with respect to the excitation and the higher order Volterra kernels are insignificant compared to the linear kernel h_1. Therefore, the unexpected spikes in the higher order auto-correlations of the MLS do not cause significant spurious components in $k_1(m)$. However, when the excitation power is increased, the higher order nonlinear components in the magnetization response become larger than the linear component and the spurious components in $k_1(m)$ are observed. Also, when the excitation sequence is a random binary sequence, the even order Volterra kernels are zero and hence no spu-

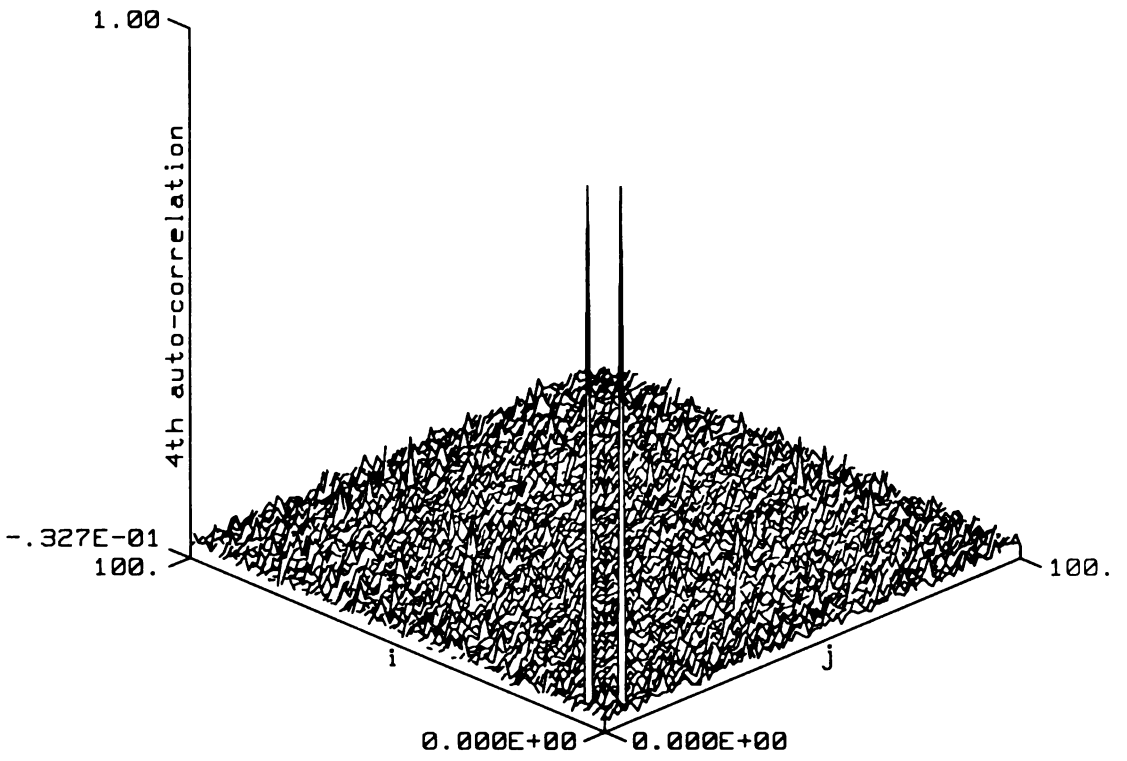

Figure 3.20: Numerically calculated fourth order auto-correlation of a sub-sequence generated by a 31-bit MLS generator, $\langle \alpha(n)\,\alpha(n-i)\,\alpha(n-j)\,\alpha(n-255) \rangle$. The sequence takes on the values ± 1. $N = 10000$.

rious component can be generated from the even order kernels. When the sequence is a MLS with high power, the even order kernels are not necessarily zero and spurious components may be generated from these kernels.

For one dimensional NMR spectroscopy, the optimum excitation power level that gives the maximum signal-to-noise ratio is usually so small that the magnetization response is roughly linear (see Chapter 2). Therefore, the undesirable features in the higher order auto-correlations of MLS do not cause significant noise-like distortion in the reconstructed spectrum. However, these undesirable features will make the interpretation of multi-dimensional stochastic NMR data very difficult. One easy way to reduce the

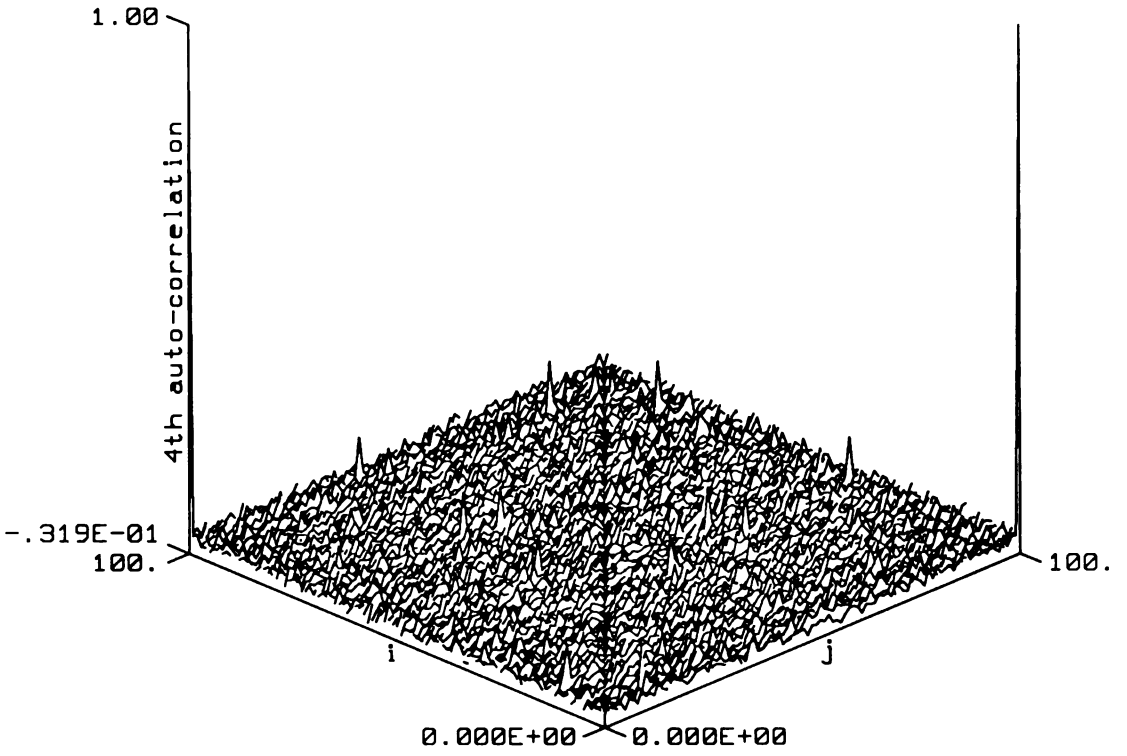

Figure 3.21: Numerically calculated fourth order auto-correlation of a sub-sequence generated by a 31-bit MLS generator, $\langle \alpha(n)\,\alpha(n-i)\,\alpha(n-j)\,\alpha(n-100)\rangle$. The sequence takes on the values ± 1. $N = 10000$.

amount of noise-like distortion for a given excitation power is to use a MLS generator with more feedback paths (taps). For example, a 30-bit MLS generator consists of a 30-bit shift register with the exclusive-OR of the 1^{st}, 4^{th}, 6^{th} and 30^{th} bits fed back to form the 0^{th} bit. Erroneous spikes will only occur in auto-correlations of order 5 or higher, therefore, only Volterra kernels of order 5 or higher will contribute spurious components to $k_1(m)$. As shown in Chapter 2 the integrated line intensity decreases rapidly as the excitation power is increased, i.e. as the system is more nonlinear; we expect the non-linear components of the magnetization response to decrease rapidly with the order of the nonlinearity. Hence, the spurious components generated by the 5^{th} order Volterra

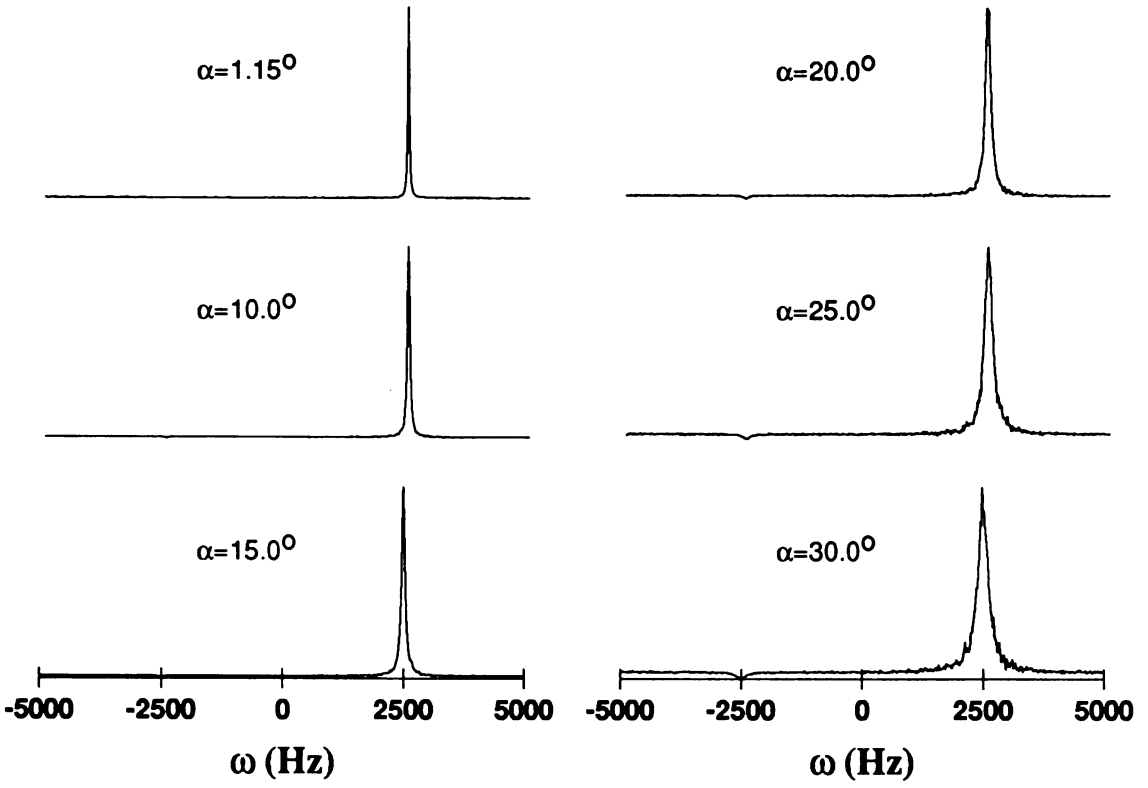

Figure 3.22: Monte Carlo simulated line shapes of $K_1(\omega)$ for random flip angle excitation with sub-sequences generated by a 30-bit MLS generator. $T_1 = 0.5$s, $T_2 = 10$ms, $T_R = 0.1$ms, $\nu = 2500$Hz and $N = 512000$.

kernel is usually much smaller than those by the 3^{rd} and the 4^{th} order kernels. Consequently there will be less noise-like distortion when the 30-bit MLS is used. This is demonstrated by the Monte Carlo simulated $K_1(\omega)$ in Figure 3.22. The lines have much less noise-like distortion than those in Figure 3.13.

Chapter 4

Experimental Verification

4.1 Experimental Setup

To verify the theoretical results of the previous two chapters, stochastic NMR experiments were done on a 0.5T whole body imaging system. Experiments at 0.5T are justified by the fact that the analysis is independent of field strength, and the results will be applicable to studies at field strength 10 to 20 times greater. The imaging system was developed by IBM Corporation, Massachusetts Institute of Technology and Lawrence Berkeley Laboratory. It consists of a 1 meter bore superconducting magnet, gradient power supplies (Oxford Instruments, Oxford, England) and a spectrometer (IBM/MIT/LBL). The flexible architecture of the system allows many different types of NMR experiments, including stochastic NMR, to be performed with very little hardware modification.

The RF transmitter has sixteen 2-word ECL registers that determine the magnitude and phase of an RF pulse. These registers are loaded by software and selected using four TTL digital logic lines. These four lines are usually driven by the pulse programmer which compiles and runs the pulse program set up by the users. To perform stochastic NMR with binary MLS excitation, a circuit was built to interpose two 31-bit MLS generators between the pulse programmer and transmitter (Figure 4.1). The 31-bit MLS generator is a 31-bit shift register with the exclusive-OR of the 3^{rd} bit and the 31^{st} bit fed back to form the first bit after the next clock pulse (Figure 3.17). One pseudo-random

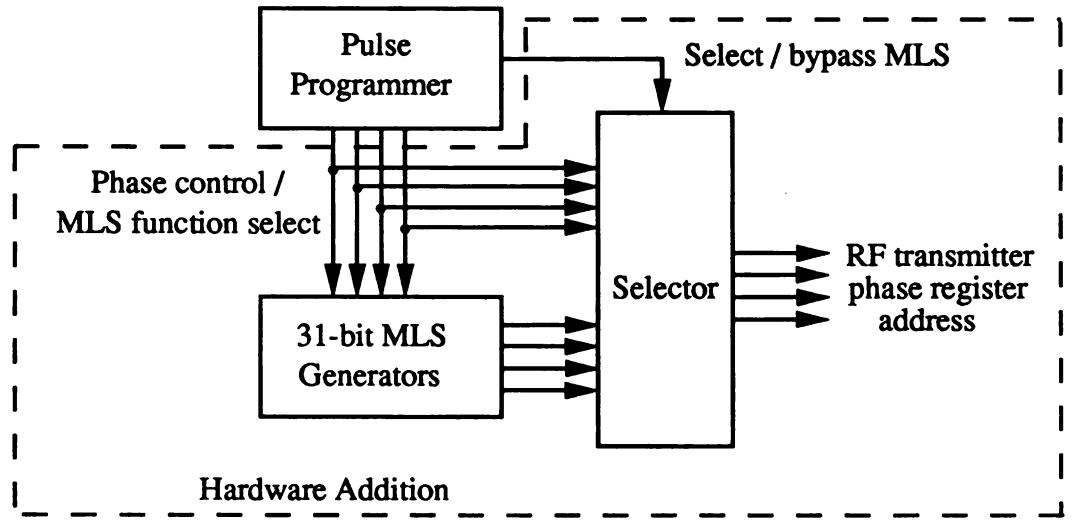

Figure 4.1: Modification of the hardware required for stochastic NMR with MLS excitations.

binary number is generated at the 31st bit after every clock pulse. The schematic diagram of the additional hardware required to do stochastic NMR with MLS excitation is shown in Figure 4.1. Each of the two MLS generators has eight dip switches which allow a selection of 256 different starting points of the MLS. The starting point of the two MLS generators must be different and the cross-correlation of the outputs of the two generators must be calculated to ensure that there is no correlation between the two sub-sequences generated.

Only one MLS generator is used for random flip angle excitation. The output of this MLS generator will select two phase registers which are preset to give two RF vectors that have the same magnitude but 180° out of phase. To perform random phase excitation or random quadrature excitation, both MLS generators are enabled, yielding a 2-bit binary number that selects one of four different phase registers. These phase registers are preset to have the same magnitude but four different phases: ±45° and ±135°. Both MLS generators can be enabled and clocked in software (via the pulse

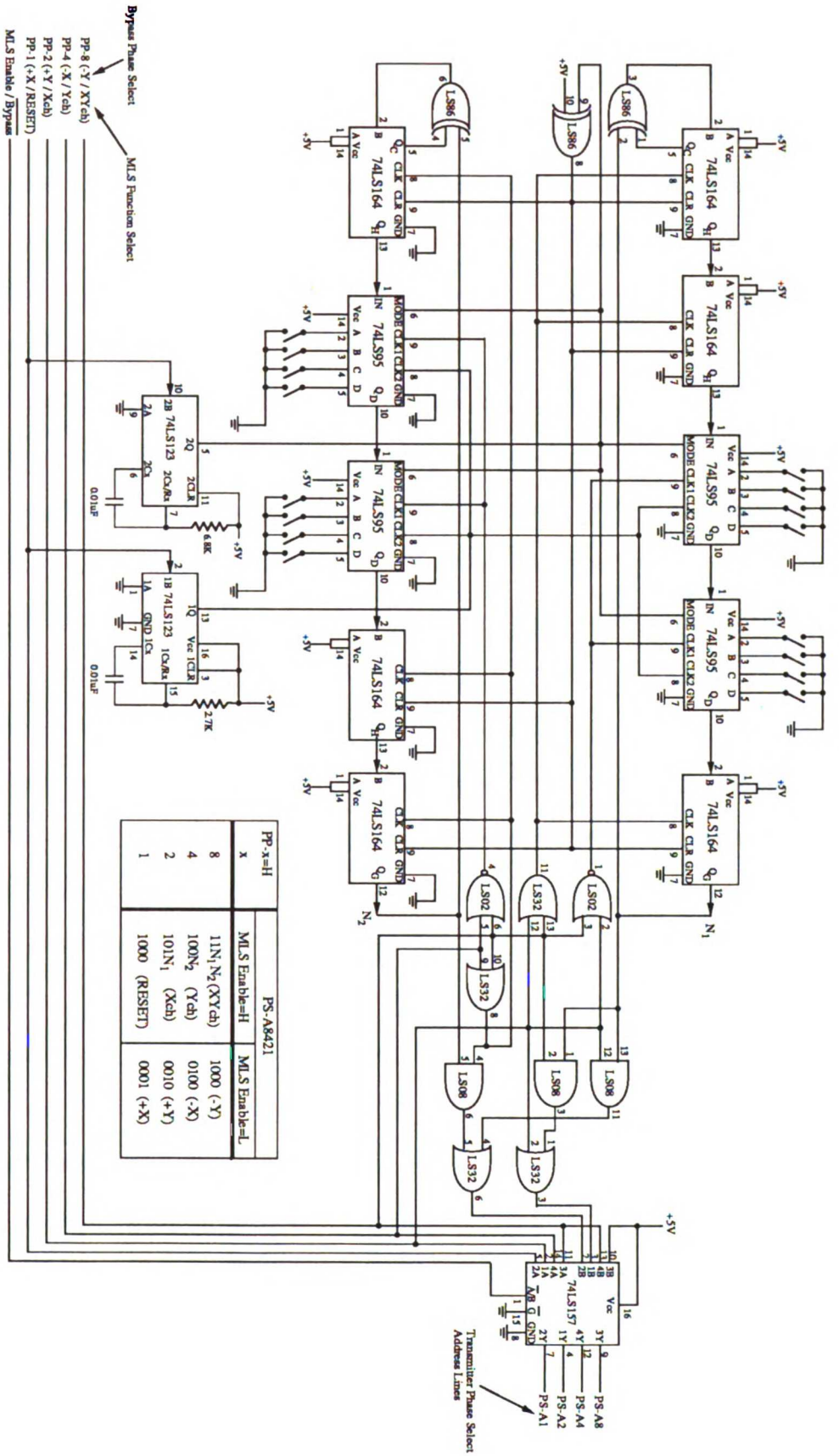

Figure 4.2: Schematic diagram of MLS generators and logic control

programmer). Every pulse sent to the MLS generator will generate a RF pulse which is then followed by sampling of one signal data point. The algorithm used in the hardware MLS generator is also implemented in software to regenerate the random sequence for calculation of the input-output cross-correlation. Non-zero mean sequences can also be generated easily. For example, random flip angle excitation with any non-zero mean can be achieved by presetting the two phase registers to have different magnitudes but still are 180° out of phase.

As discussed earlier, random flip angle excitation, random phase excitation and random quadrature excitation can all be implemented with random binary sequences. Except at very high excitation power, random binary excitation and Gaussian white noise excitation give almost identical responses. Also, the hardware implementation of a Gaussian white noise sequence is substantially harder. Therefore Gaussian white noise excitation was not implemented for this dissertation.

The sample used is a sphere with a diameter of 10cm filled with a copper sulphate solution. The T_1 and T_2 of the sample are measured to be 160ms and 140ms respectively. However, due to static field inhomogeneity (1ppm), the effective T_2, T_2^*, is only 45ms. All the experiments were done with a T_R of 200μs. This corresponds to an optimum RMS flip angle of about 2.8°. The width of the reconstructed spectrum is $1/T_R$ = 5kHz (Equation 2.15). The duration of the RF pulse is 25μs, which corresponds to an excitation bandwidth of about 40kHz. Therefore, the RF pulses satisfy the hard pulse assumption made in Chapter 1. The flip angles of the RF pulses were calibrated by a conventional NMR experiment that consisted of a single RF pulse followed by sampling of the FID; the peak height of the reconstructed spectral line is proportional to the sine of the flip angle. The number of data points, N, sampled for each experiment is 65536.

4.2 Experimental Results

Initial results showed that there was an unexpected component with very broad line width in addition to the line from the copper sulphate solution. The broad component was significant only when the excitation power was high, i.e., when the line from the copper sulphate solution was highly saturated and gave out very little signal as shown in Figure 4.3a. Further investigation with the copper sulphate sample removed from the magnet showed that the broad component was Lorentzian (Figure 4.3b) and behaved like a stochastic NMR line with an optimal flip angle $\alpha_{max} = 25°$. The broad component disappeared when the RF probe was removed from the magnet. This suggested that the signal was resulted from the plastic material in the RF probe. Using Ernst angle formula, T_1 of the plastic material is about 2ms, and from the line width, T_2 is about 0.5ms. This suggests that stochastic NMR is a very good tool for studying samples with very short T_2. In order to avoid confusion in the interpretation of the spectral line of the copper sulphate solution, the plastic line was obtained for each study and subtracted to correct the baseline.

The first set of experiments was performed with random flip angle excitation. Figure 4.4 is a plot of the average signal power as a function of the RMS flip angle. The average signal power is given by the time average of the magnitude square of the sampled signal sequence. The symbol * represents experimental data and the solid line is the corresponding theoretical prediction. The plot shows good agreement between theory and experiment. It also shows that $\alpha_{max} \approx 3.0°$. This corresponds to a peak RF power of only 1/500 of that needed to give the Ernst angle for a conventional pulsed FT-NMR experiment using a 25μs RF pulse with $T_R = T_1 = 160$ms.

Analysis in Chapter 2 shows that there will be line broadening and a notch artifact in $K_1(\omega)$ as the excitation power is increased. Figure 4.5 is a side-by-side comparison of experimental and theoretical line shapes of $K_1(\omega)$. There are three important features

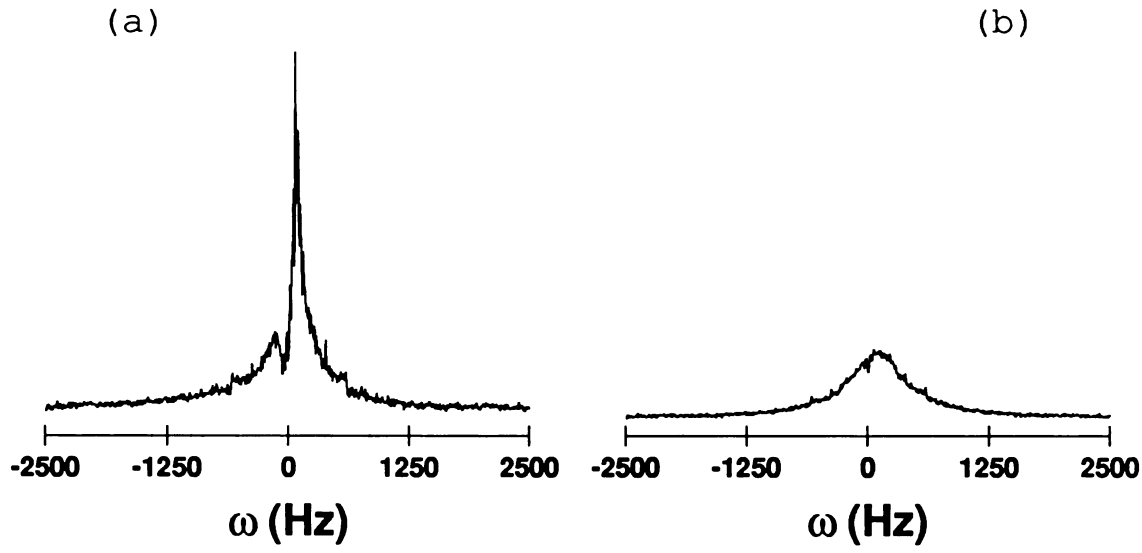

Figure 4.3: Experimental line shapes of $K_1(\omega)$ for random flip angle excitation with MLS. The copper sulphate solution is (a) inside and (b) removed from the RF probe. $T_1 = 160$ms, $T_2^* = 45$ms, $T_R = 0.2$ms, $\nu = 60$Hz, $N = 65536$ and a RMS flip angle of 24°.

of the lines that should be noticed: (1) the line width, (2) the notch artifact and (3) the noise-like distortions. The line broadens and the notch artifact gets worse as the RMS flip angle is increased. They behave just as predicted in Figure 4.5b for random binary flip angle excitation. Since the experimental excitation sequence is a MLS, it is not surprising to have noise-like distortion. The noise-like distortion increases as the RMS flip angle increases. This agrees with Blümich and Ziessow's observations [14] and the Monte Carlo simulated results shown in the previous chapter (Figure 3.13). The Monte Carlo simulated result in Figure 3.15 shows spurious components in $k_1(m)$ at $m = 62$, 143 and 255. These spurious components are expected to be present in the experimental results since the hardware MLS generator is the same as the one used in the Monte Carlo simulation. Figure 4.6 shows the real part of $k_1(m)$ obtained by experiment with an RMS flip angle of 24° and a resonance offset of 1250Hz. It looks strikingly similar to Figure 3.15 even though the T_1, T_2 and the imaging parameters are different. The spurious components are at $m = 62$, 143 and 255.

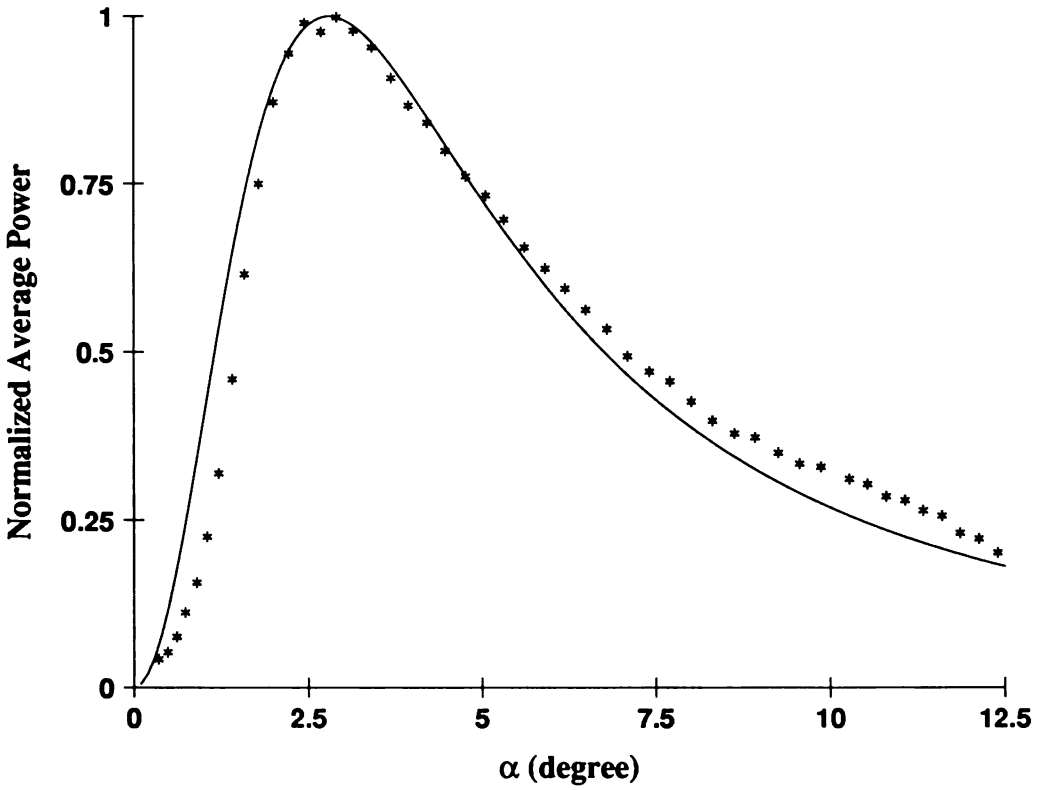

Figure 4.4: Average signal power for random binary flip angle excitation. The excitation sequence is a sub-sequence of a 31-bit MLS generator. The symbol * represents experimental data and the solid line is the theoretical prediction. $T_1 = 160$ms, $T_2^* = 45$ms, $T_R = 0.2$ms and $\nu = 500$Hz.

Theoretical analysis in Chapter 2 shows that the signal power spectrum has less notch artifact than $K_1(\omega)$. Also, the noise analysis in Chapter 3 shows that measurement noise should appear as a DC offset in the signal power spectrum. Figure 4.7a shows the signal power spectra of the same data sets used to obtained $K_1(\omega)$ in Figure 4.5a. They show good agreement with the theoretical predictions shown in Figure 4.5b except for a DC offset resulting from the measurement noise. The notch artifact is indeed smaller than that in $K_1(\omega)$. It is very interesting to notice that the signal power spectrum shows insignificant noise-like distortion even when the excitation power is very high. This may be another advantage of signal power spectrum over $K_1(\omega)$ as an estimate of the real spectrum.

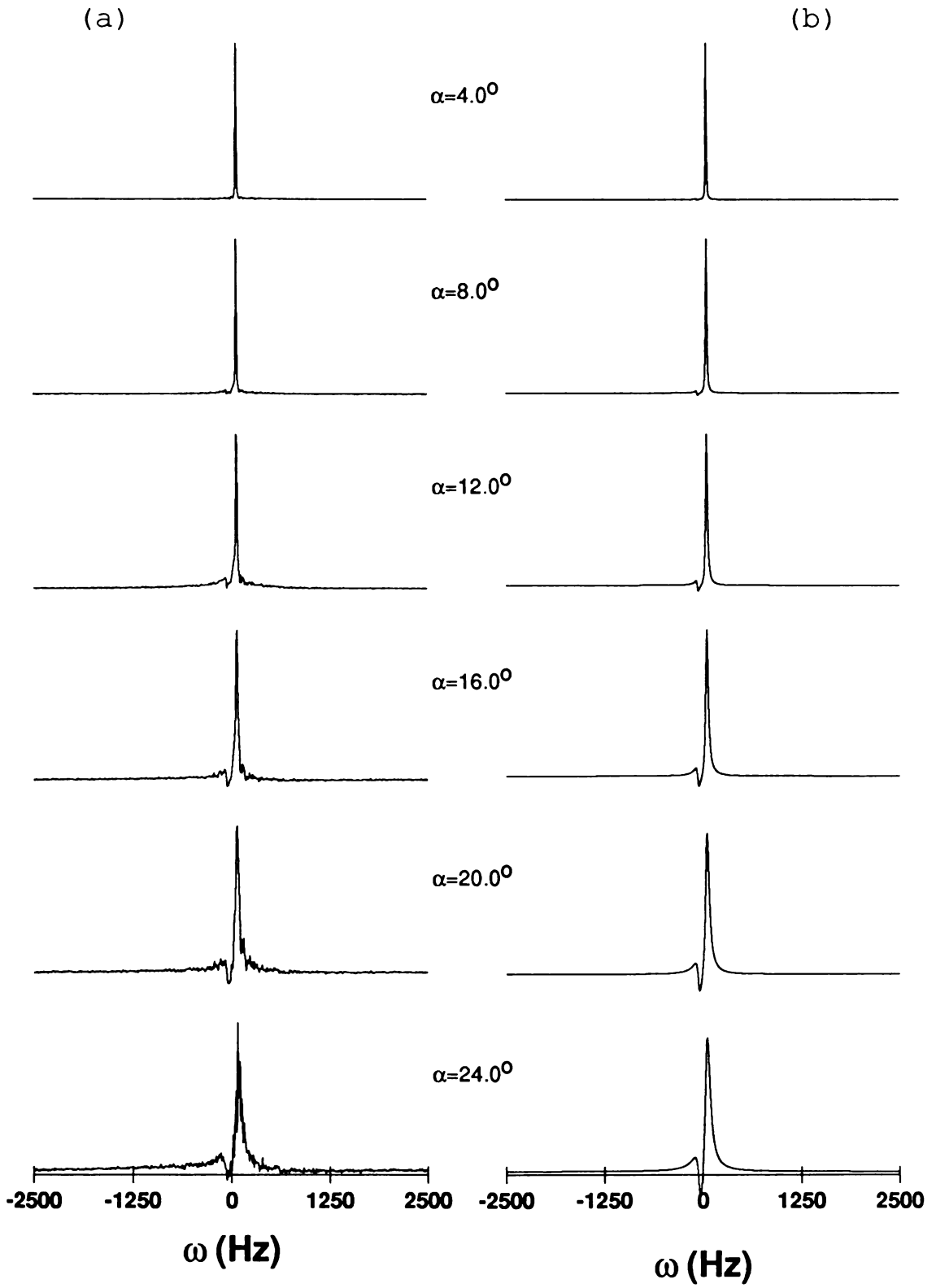

Figure 4.5: Line shapes of $K_1(\omega)$ for random binary flip angle excitation. (a) Experimental results using a 31-bit MLS generator and (b) theoretical predictions with truly random binary sequences. $T_1 = 160$ms, $T_2^* = 45$ms, $T_R = 0.2$ms, $N = 65536$ and $\nu = 60$Hz.

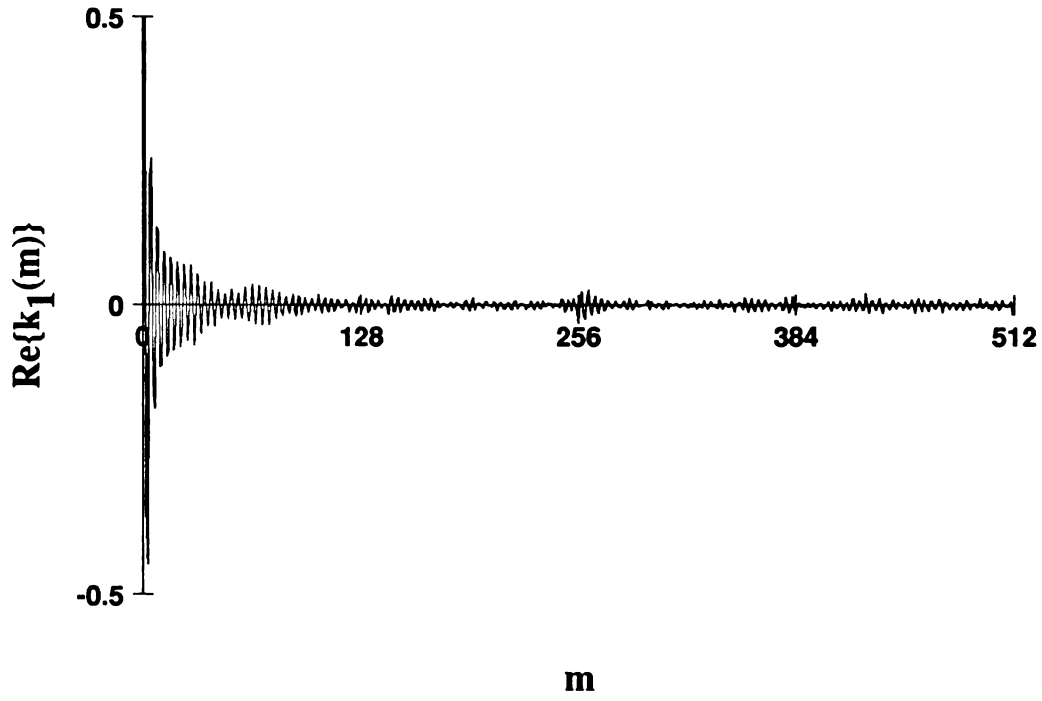

Figure 4.6: Experimentally obtained real part of $k_1(m)$ for random flip angle excitation with a sub-sequence generated by a 31-bit MLS generator. $T_1 = 160$ms, $T_2^* = 45$ms, $T_R = 0.2$ms, $\nu = 1250$Hz, $N = 65536$ and a RMS flip angle of 24°.

Figures 4.8, 4.9 and 4.10 are the corresponding results for random phase and/or random quadrature excitations. There is very good agreement between experimental and theoretical results. As predicted in theory (Chapter 2), there is no notch artifact observed in $K_1(\omega)$. All other aspects are very much the same as those for random flip angle excitation.

A non-zero mean excitation sequence may set up a steady state magnetization response that results in a notch artifact at zero resonance offset and a mirror image artifact at the negative of the resonance offset of the line (see Chapter 2). Figure 4.11 is a comparison of experimental and theoretical results for a non-zero mean excitation sequence that takes on the two values, 0 and α, equally likely. The resonance offset is 100Hz and α is 5°. Notice the erroneous component at -100Hz, the negative of the resonance offset. The artifact is significant even for such small flip angle.

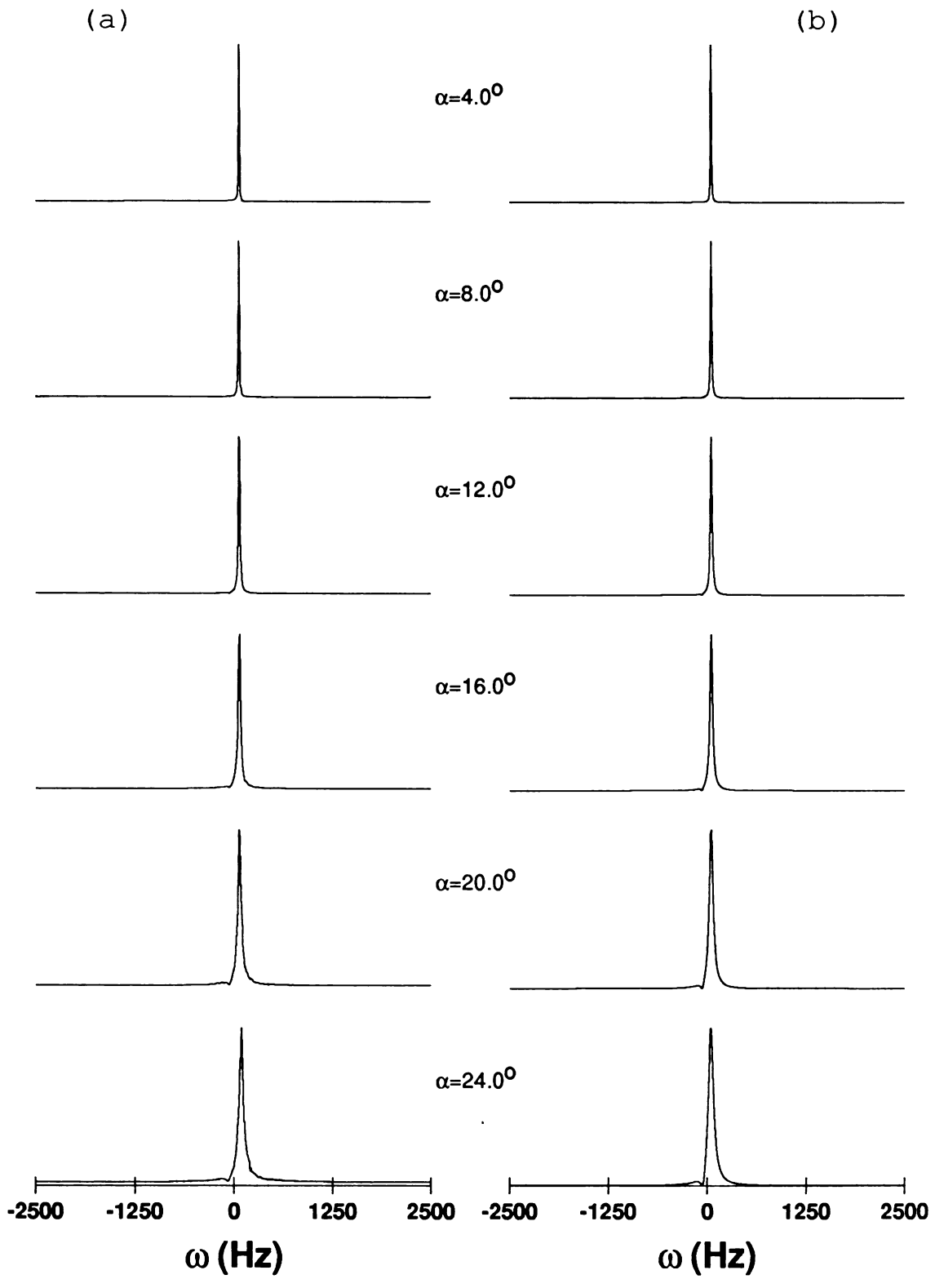

Figure 4.7: Signal power spectrum for random binary flip angle excitation. (a) Experimental results using a 31-bit MLS generator and (b) theoretical predictions with truly random binary sequences. $T_1 = 160$ms, $T_2^* = 45$ms, $T_R = 0.2$ms, $N = 65536$ and $\nu = 60$Hz.

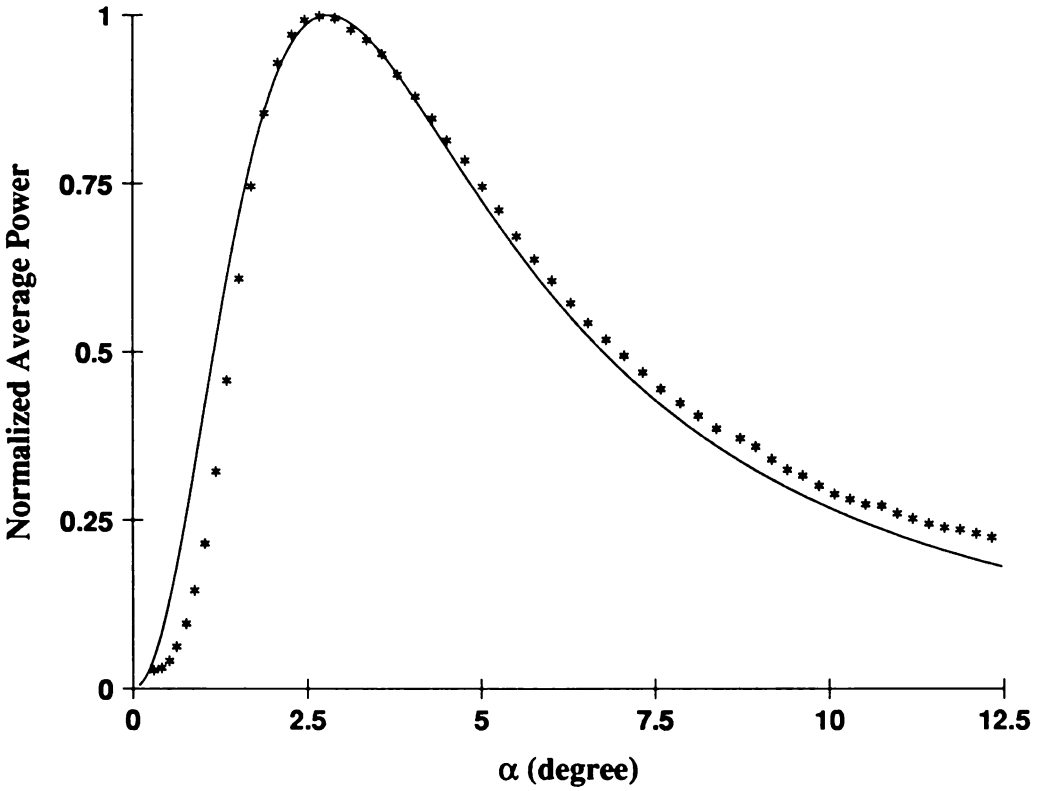

Figure 4.8: Average signal power for random quadrature/random phase excitation. The excitation sequence is a complex sub-sequence generated by two 31-bit MLS generators. The symbol * represents experimental data and the solid line is the theoretical prediction. $T_1 = 160$ms, $T_2^* = 45$ms, $T_R = 0.2$ms and $\nu = 500$Hz.

As discussed in the introduction chapter of this dissertation, one reason for applying discrete excitation and characterizing the stochastic experiments with discrete analysis is that the theoretical results correspond exactly to practical experiments. This is verified by the good agreement between theoretical and experimental results shown in this chapter.

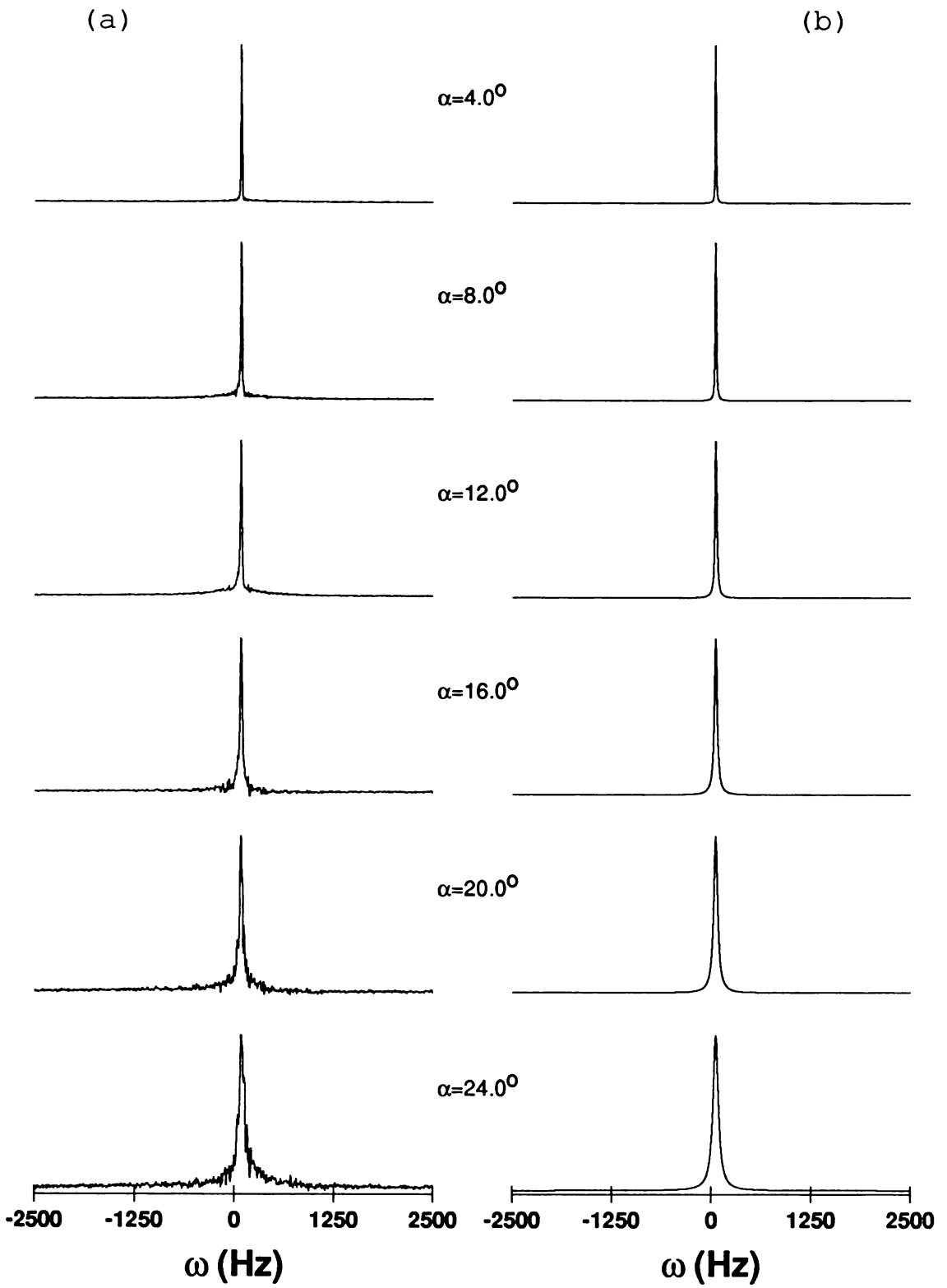

Figure 4.9: Line shapes of $K_1(\omega)$ for random quadrature/random phase excitation. (a) Experimental results using two 31-bit MLS generators and (b) theoretical predictions with truly random binary sequences. $T_1 = 160$ms, $T_2^* = 45$ms, $T_R = 0.2$ms, $N = 65536$ and $\nu = 60$Hz.

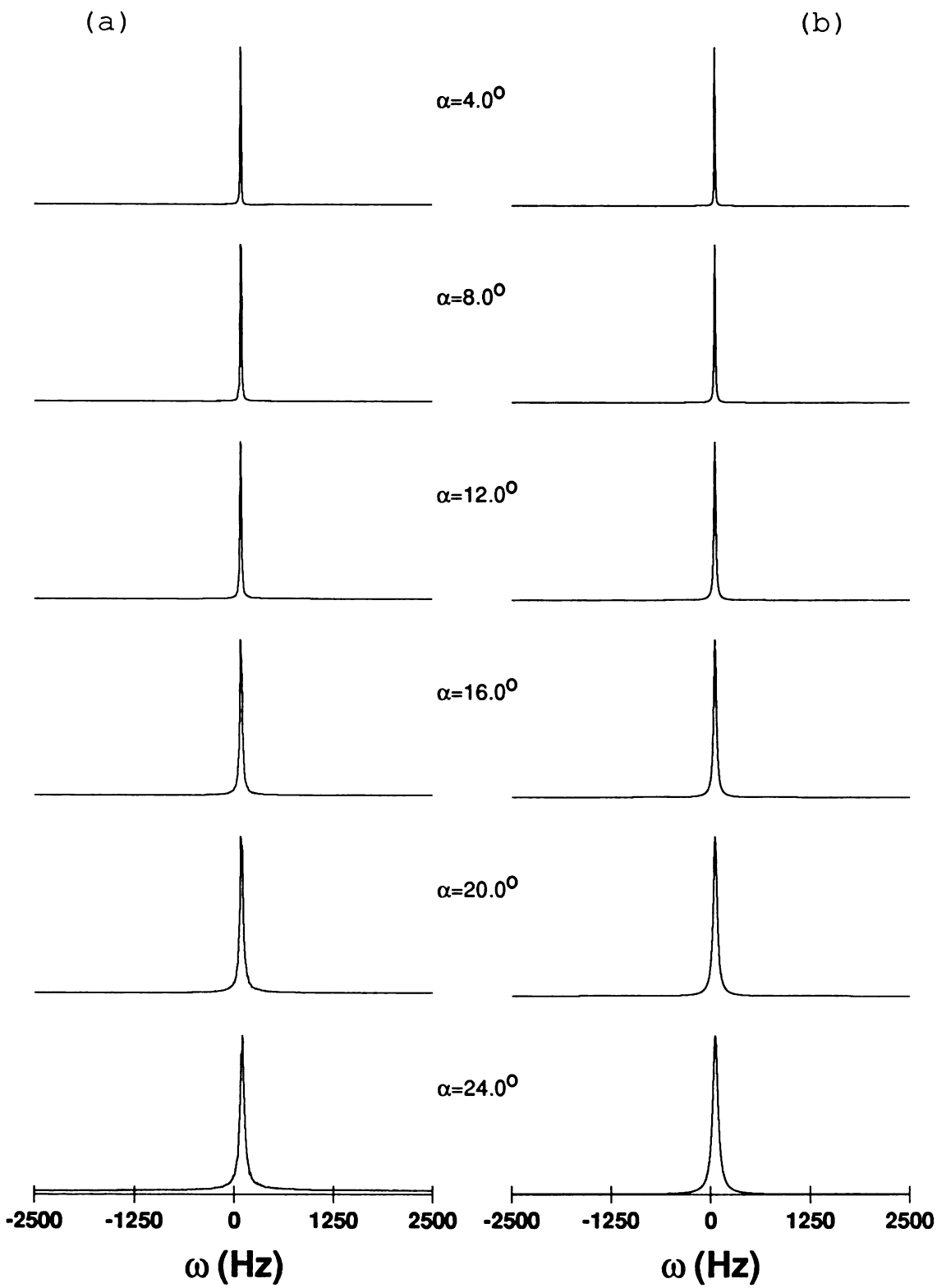

Figure 4.10: Signal power spectrum for random quadrature/random phase excitation. (a) Experimental results using two 31-bit MLS generators and (b) theoretical predictions with truly random binary sequences. $T_1 = 160$ms, $T_2^* = 45$ms, $T_R = 0.2$ms, $N = 65536$ and $\nu = 60$Hz.

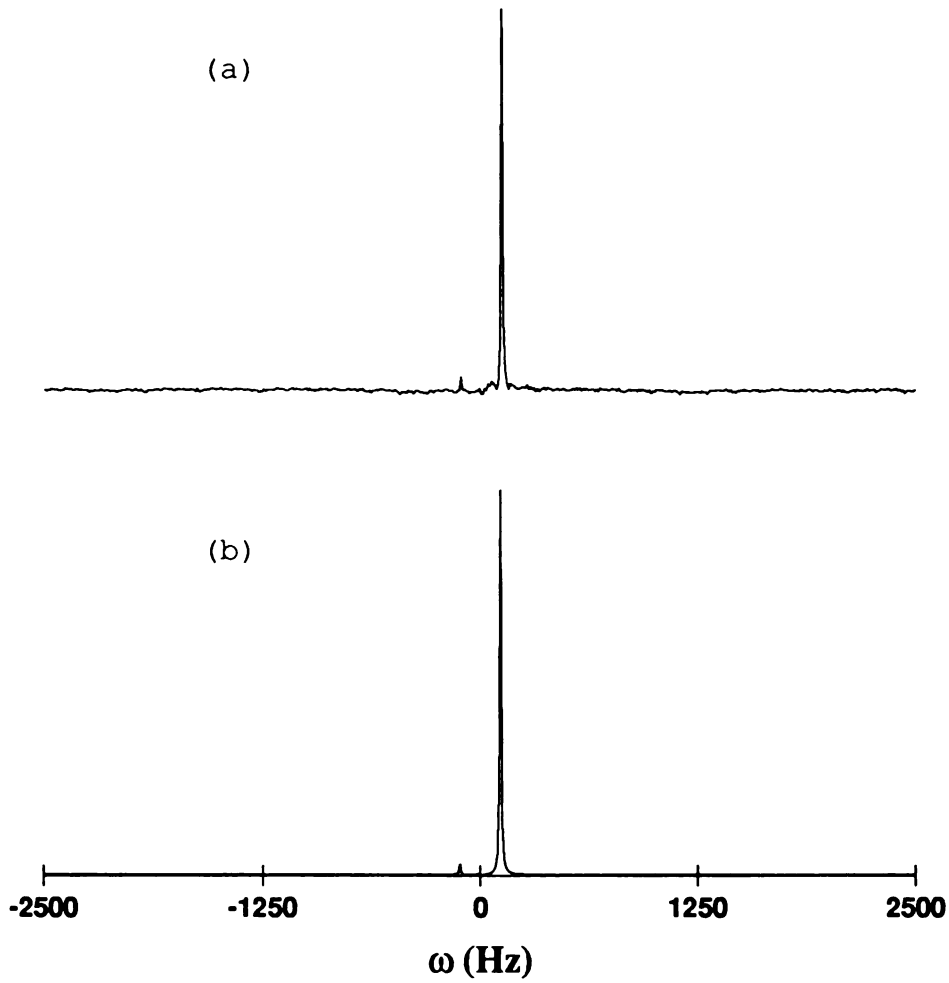

Figure 4.11: Line shape of $K_1(\omega)$ for random flip angle excitation with a binary sequence that takes on 0 and α. (a) Experimental result using a 31-bit MLS generator and (b) theoretical predictions with truly random binary sequences. $T_1 = 160$ms, $T_2^* = 45$ms, $T_R = 0.2$ms, $N = 65536$, $\nu = 100$Hz and $\alpha = 5°$.

Chapter 5

Summary and Conclusion

The analysis in the previous chapters will be summarized in the following three sections. The first section will compare the saturation characteristics of the three different excitation schemes. The effectiveness of using the Fourier transform of the input-output cross-correlation and the signal power spectrum as estimates of the spectrum will be addressed in the second section. The third section will discuss the pros and cons of using MLS to approximate the random binary excitation. The fourth section is an outline of possible future work. The last section is a grand summary of the dissertation.

5.1 Comparison of Excitation Schemes

Studies of only one type of excitation, the random flip angle excitation, have been reported in the literature. Analysis of the input-output cross-correlation for continuous excitation [3,10,12] reported line broadening and a slight shift in resonance offset as the only types of spectral distortion at high excitation power. However, the analysis in Chapter 2 shows that there is also a notch artifact at the negative of the resonance offset. In addition there is a non-uniform line broadening across the spectrum, lines close to zero resonance offset have twice the line broadening of lines far off resonance. When the RMS flip angle is set to the RMS flip angle that maximizes the S/N ratio, the notch artifact is usually insignificant. However, the non-uniformity of the response may still be quite noticeable for lines with natural line width small compared to the line broadening.

To improve on the results of previous workers, two new types of excitation were introduced in Chapter 2, the random phase excitation and the random quadrature excitation. The random phase of both types of excitation removes the notch artifact and gives a uniform line broadening across the spectrum. The shift in resonance offset of the reconstructed lines is usually negligible, leaving the line broadening as the only distortion. The line broadening results in a loss of resolution, however, it is predictable and it does not affect the integrated line intensity.

The random phase excitation and the random quadrature excitation give almost identical average signal power that is independent of the resonance offset. The signal-to-noise ratio is maximized when the RMS flip angle is equal to α_{max}, which is approximately the Ernst angle, $\cos^{-1}(e^{-T_R/T_1})$. For RMS flip angles up to α_{max}, the performance of the two types of excitation are identical and both the Fourier transform of the input-output cross-correlation and the signal power spectrum are good estimates of the true spectrum. In addition, α_{max} is usually one to two orders of magnitude smaller than the Ernst angle for a conventional pulsed FT-NMR experiment with $T_R \approx T_1$. This corresponds to a reduction of the peak RF power requirement by a factor of 10^2 to 10^4 when compared to the conventional pulsed FT-NMR experiments.

The average signal power obtained with the random flip angle excitation is very similar to the other two types of excitation except for a small dependence on the resonance offset of the line. This is a consequence of the non-uniformity in the spectral response of this type of excitation. Even though the signal power spectrum has much less notch artifact than the Fourier transform of the input-output cross-correlation, the signal power spectrum still suffers from the non-uniformity in response across the spectrum, even when the RMS flip angle is α_{max}. The amount of non-uniformity can be reduced by dropping the RMS flip angle below α_{max}, i.e. by sacrificing the S/N ratio.

The comparison above shows that the random phase excitation and the random quadrature excitation are better excitation schemes than the random flip angle excita-

tion no matter whether the Fourier transform of the input-output cross-correlation or the signal power spectrum is used to approximate the real spectrum.

5.2 Comparison of $K_1(\omega)$ and $S(\omega)$

At low excitation power such that the magnetization response is linear, both the Fourier transform of the input-output cross-correlation, $K_1(\omega)$, and the signal power spectrum, $S(\omega)$, are good estimates of the real spectrum. At higher excitation power, they show slightly different saturation behavior. The advantages of $S(\omega)$ over $K_1(\omega)$ are

1. $S(\omega)$ is obtained from the signal only. The excitation sequence need not be stored or regenerated for the reconstruction. This simplifies hardware and software design.

2. In the case of random flip angle excitation, $S(\omega)$ shows much less notch artifact.

3. $S(\omega)$ is much less sensitive to the undesirable spikes in the higher order autocorrelations of the MLS. Consequently, it shows much less noise-like distortion.

4. $S(\omega)$ will look smoother, less noisy than $K_1(\omega)$ when the measurement noise is the dominating noise source because white measurement noise will behave as white noise in $K_1(\omega)$, whereas this noise appears as a DC offset in $S(\omega)$.

The disadvantages are:

1. The signal-to-systematic-noise ratio for $S(\omega)$ is about 3dB lower than that for $K_1(\omega)$.

2. The measurement noise is transformed to a process consisting mainly of a DC offset. The non-white systematic noise may result in observable structural artifacts

when the signal-to-measurement-noise ratio is low. A longer signal sequence, i.e. a large N, must be used to guarantee a higher signal-to-measurement-noise ratio.

5.3 Pros and Cons of MLS

Theoretical analysis shows that at the optimal excitation power that maximizes the average signal power, random binary sequences and Gaussian white noise sequences give almost identical spectral response. The major advantage of random binary sequences over Gaussian white noise sequences is that random binary sequences can be approximated by maximum length sequences (MLS). The advantages of MLS are:

1. MLS is inexpensive to generate in hardware and software. The sequence can be regenerated any time it is needed.

2. The binary nature simplifies the computations of cross-correlations and auto-correlations. Time consuming multiplication operations are replaced by simple additions and subtractions in the Fast Hadamard Transform algorithms. The computation time is even shorter than using Fast Fourier Transform algorithms.

3. The periodic nature of MLS allows coherent signal averaging to improve S/N ratio.

4. When Gaussian white noise sequences or truly random binary sequences are used, the systematic noise power is inversely proportional to N, the total number of signal points used to calculate the cross-correlation and auto-correlation by time averaging. However, when a MLS is used and N is equal to an integral multiple of the period of the MLS, there is a gain of about 20dB in signal-to-systematic-noise ratio over Gaussian white noise sequences and truly random binary sequences of similar length.

However, one must observe some precautions when using MLS:

1. The sum of a full MLS that takes on the values $\pm\alpha$ is non-zero. Therefore, if the product of the period of the MLS and T_R is comparable or shorter than T_1 and T_2, the magnetization response may acquire a non-zero steady state component that results in an artifact at the negative of the resonance offset and a non-uniform response across the spectrum. If this is the case, a MLS with a longer period must be used. This may result in a large N.

2. MLS has very undesirable higher order statistics. Auto-correlations of high orders have unexpected generator-dependent spikes. These spikes excite high order nonlinear components of the spin system and cause noise-like distortion to be introduced into the Fourier transform of the input-output cross-correlation when the excitation power is high. The amount of noise-like distortion is usually insignificant at the power level that maximizes the S/N ratio, i.e. when the magnetization response is nearly linear. One way to reduce the noise-like distortion for a given excitation power is to use a MLS generator that has more bits being fed back to form the 0^{th} bit (Section 3.4). The noise-like distortion can also be reduced significantly by using the signal power spectrum to approximate the real spectrum.

5.4 Future Developments

Blümich and Ziessow [13,14,15,16,17,18,19,20] have demonstrated experimentally that the same set of data that is used to estimate the one dimensional spectrum can also be used to study the correlations between different resonances and multiple-quantum coherence effects in complex spin systems. The multi-dimensional spectroscopic information is related to the multi-dimensional input-output cross- correlations. It is a logical extension of this dissertation to characterize the reconstructed multi-dimensional spectra

obtained with discrete stochastic excitations, namely, to

- identify the types of multi-dimensional spectroscopic information that the spectra deliver, possibly as a function of excitation power,
- find the optimal excitation power that maximizes a given type of spectroscopic information, yet maintaining a reasonable S/N ratio, and
- compare the information content of the spectra obtained with different types of excitation sequences, e.g., Gaussian white noise sequences versus random binary sequences.

The assumption of isolated spin systems will no longer be valid, i.e. the Bloch equations are not applicable. Density matrix notations must be used to describe the spin systems. RF excitations and spin-spin interactions must be treated using quantum mechanics. Thus the analysis will be substantially more complicated than that in this dissertation.

As discussed in the previous section, MLS is the ideal excitation sequence for one dimensional spectroscopy at low excitation power. In multi-dimensional stochastic NMR, spectral information is obtained through spin-spin interactions which are basically nonlinear interactions. The spin system must be driven to a nonlinear regime. The undesirable higher order statistics of MLS may lead to the reconstructed spectral information of limited value. One formidable task is to investigate the nonlinear response for different MLS generators so that the unexpected spikes in the auto-correlations can be used to infer spectral information. Another formidable task is to search for binary, or multi-level, random sequences that possess the advantages of the MLS, but with better statistical properties.

So far the randomness of the experiment is introduced through RF excitations. However, randomness may be introduced through T_R. Knight and Kaiser [26] have analyzed the input-output cross-correlation of the Bloch equations driven by a random telegraph

signal. One possible application of such stochastic experiments is to achieve spectral localization or selective excitation through use of non-white excitation processes.

The advance in gradient coil design allows fast switching of magnetic field gradients [27,28,29]. Stochastic gradients may become another source of randomness in the forseeable future. Since the gradients are tightly related to the spatial distribution of spins, stochastic gradient approach are applicable to NMR imaging. The analysis will be very similar to that in this dissertation because the Bloch equations are usually applicable.

Finally, NMR imaging and spectroscopic imaging can also be achieved by stochastic RF excitations together with time varying gradients. Based on a linearized model Roos *et al* [23] have obtained theoretical expressions describing the spatial localization function achieved with sinusoidal gradients. They have verified their results experimentally and extended the idea to spectroscopic imaging. Further work needs to be done to

- study the saturation effects when the analysis includes the full Bloch model,
- obtain results with different types of excitation,
- study the localization functions and S/N ratio as a function of the excitation power and
- obtain results with different time varying gradient waveforms.

The main problem of these studies is that the magnetization response will no longer be wide-sense stationary due to the time varying gradients. Most of the results cannot be expressed in a closed form and Monte Carlo simulations will be required for the analysis.

5.5 Summary

This dissertation presents an analysis of a stochastic NMR experiment that consists of exciting the spin system with RF pulses where the flip angles or the phases of the pulses

are samples of a discrete stochastic process. The analysis shows that the maximum signal-to-noise ratio is achieved when the RMS flip angle is approximately the Ernst angle. The Ernst angle for the stochastic experiment is usually more than an order of magnitude smaller than that for a conventional FT-NMR experiment. This results in a peak RF power requirement that is several orders of magnitude smaller than the conventional experiment.

The analysis shows that the maximum signal-to-noise ratio is achieved when the RMS flip angle is approximately the Ernst angle. When the RMS flip angle is below the Ernst angle, the input-output cross-correlation is a good estimate of the FID. Increase of excitation power causes line broadening. In addition, the use of random flip angle, fixed phase excitation causes a notch artifact and a non-uniform response across the spectrum both of which are not found in two new types of excitation, the random phase excitation and the random quadrature excitation. The signal power spectrum is also a good estimate of the real spectrum. The approximation of the cross-correlation by a time average causes systematic noise. The amount of systematic noise is found to be significantly reduced when an entire maximum length sequence (MLS) is used for excitation. Noise-like distortion at high power MLS excitation is discovered to be related to the number of feedback paths in the MLS generator, more feedback paths gives less distortion.

This dissertation shows that stochastic NMR with random phase excitation or random quadrature excitation using MLS is simple to implement and is an effective technique for high field *in vivo* NMR studies.

Bibliography

[1] R. R. Ernst and W. A. Anderson. "Application of Fourier Transform Spectroscopy to Magnetic Resonance". *Rev. Sci. Instrum.* **37**, 93 (1966).

[2] D. I. Hoult and P. C. Lauterbur. "The Sensitivity of the Zeugmatographic Experiment Involving Human Samples". *J. Magn. Reson.* **34**, 425 (1979).

[3] R. R. Ernst. "Magnetic Resonance with Stochastic Excitation". *J. Magn. Reson.* **3**, 10 (1970).

[4] R. Kaiser. "Coherent Spectrometry with Noise Signals". *J. Magn. Reson.* **3**, 28 (1970).

[5] E. Wong. *Introduction to Random Processes*. Springer-Verlag, 1983.

[6] N. Wiener. *Non-linear Problems in Random Theory*. MIT Press, 1958.

[7] M. Schetzen. *The Volterra and Wiener Theories of Nonlinear Systems*. John Wiley & Sons, 1980.

[8] W. H. Press, B. P. Flannery, S. A. Teukolsky, and W. T. Vetterling. *Numerical Recipes, The Arts of Scientific Computing*. Cambridge University Press, 1986.

[9] R. Kaiser. "Application of the Hadamard Transform to NMR Spectrometry with Pseudonoise Excitation". *J. Magn. Reson.* **15**, 44 (1974).

[10] E. Bartholdi, A. Wokaun, and R. R. Ernst. "Theory of Stochastic NMR Spectroscopy. Application of the Itô and Stratonovich Calculus". *Chem. Phys.* **18**, 57 (1976).

[11] R. Kaiser and W. R. Knight. "Random Excitation of Magnetic Spin Systems". *J. Magn. Reson.* **50**, 467 (1982).

[12] W. R. Knight and R. Kaiser. "The Random Driven Bloch Equations". *J. Magn. Reson.* **48**, 293 (1982).

[13] B. Blümich and D. Ziessow. "2D NMR Spectra from Stochastic NMR. Coupling and Exchange Information from Third Order Frequency Kernel". *Ber. Bunsenges. Phys. Chem.* **84**, 1090 (1980).

[14] B. Blümich and D. Ziessow. "Saturation in Hadamard NMR spectroscopy and Its Description by a Correlation Expansion". *J. Magn. Reson.* **46**, 385 (1982).

[15] B. Blümich and D. Ziessow. "Practice of Multidimensional Stochastic NMR spectroscopy. The Derivation of 1D, 2D and 3D Spectra". *J. Magn. Reson.* **52**, 42 (1983).

[16] B. Blümich and R. Kaiser. "Magnetization Exchange, Zero and Double Quantum Spectra in Stochastic NMR Spectroscopy". *J. Magn. Reson.* **54**, 486 (1983).

[17] B. Blümich and D. Ziessow. "Multidimensional Spectroscopy. I. Perturbation Theory". *Molec. Phys.* **48**(5), 955 (1983).

[18] B. Blümich and D. Ziessow. "Multidimensional Spectroscopy. II. Analysis of 3D Lineshapes obtained from Stochastic NMR of Two Level Systems". *Molec. Phys.* **48**(5), 969 (1983).

[19] B. Blümich and D. Ziessow. "Nonlinear Noise Analysis in Nuclear Magnetic Resonance Spectroscopy. 1D, 2D and 3D Spectra". *J. Chem. Phys.* **78**(3), 1059 (1983).

[20] B. Blümich. "Stochastic Time Resolved CIDNP spectroscopy: Suggestion of an Experimental Method". *Molec. Phys.* **51**(5), 1283 (1984).

[21] B. Blümich. "Stochastic NMR Imaging". *J. Magn. Reson.* **60**, 37 (1984).

[22] D. Chaudhuri. *Hadamard Zeugmatography Using 3-D Projection Reconstruction.* Master's thesis, State University of New York at Stony Brook, August 1986.

[23] M. S. Roos, S. T. S. Wong, and R. D. Newmark. "Stochastic NMR Imaging: Spatial Localization with Oscillating Gradients". *Book of Abstracts, 7^{th} Annual Meeting of the Society of Magnetic Resonance in Medicine* **1**, 956 (1988).

[24] D. E. Knuth. *The Art of Computer Programming.* Volume 2, Addison-Wesley, 2 edition, 1981.

[25] I. S. Gradshteyn and I. M. Ryzhik. *Table of Integrals, Series and Products.* Academic Press, 1980.

[26] W. R. Knight and R. Kaiser. "Bloch Equations Driven by a Random Telegraph Signal". *J. Magn. Reson.* **62**, 65 (1985).

[27] R. Turner. "Coils of Minimum Inductance". *Book of Abstracts, 7^{th} Annual Meeting of the Society of Magnetic Resonance in Medicine* **1**, 26 (1988).

[28] S. Fujita, Y. Fujio, Y. Hashimoto, and T. Kubodera. "A New Method of Gradient Coil Design in MRI". *Book of Abstracts, 7^{th} Annual Meeting of the Society of Magnetic Resonance in Medicine* **1**, 27 (1988).

[29] J. W. Carlson. "An Optimized, Highly Homogeneous Shielded Gradient Coil Design". *Book of Abstracts, 7^{th} Annual Meeting of the Society of Magnetic Resonance in Medicine* **1**, 28 (1988).

Appendix A

Derived Wiener Kernels

One difficulty in deriving the derived Wiener kernels is to find a set of consistent notations that can be extended to different orders of derived Wiener kernels. One approach is to extend the matrix notations in Chapter 2 to tensor notations, however, the derivation would become very cumbersome. The approach taken here is to deal with the components of the magnetization vector individually. The derivation is long and tedious, even for $k_{1(5)}$, due to the large number of terms involved. The derivation of $K_{1(3)}(\omega)$ for random flip angle excitation will be outlined here. A similar derivation is used to obtain $K_{1(5)}(\omega)$.

According to Equations 2.46 and 2.47 $k_{1(3)}(m)$ is

$$k_{1(3)}(m) = -3\alpha^2 \sum_{n=-\infty}^{\infty} k_3(n,n,m), \tag{A.1}$$

where

$$\begin{aligned} k_3(n,n,m) &= \frac{1}{6\alpha^6}\langle [M_{xy}(j) - \sum_{l=0}^{\infty} k_1(l)\alpha_x(j-l)]\alpha_x(j-m)\alpha_x^2(j-n)\rangle \\ &= \begin{cases} \frac{1}{6\alpha^6}\langle M_{xy}(j)\alpha_x(j-m)\alpha_x^2(j-n)\rangle - \frac{1}{2\alpha^4}k_1(m) & \text{if } n = m \\ \\ \frac{1}{6\alpha^6}\langle M_{xy}(j)\alpha_x(j-m)\alpha_x^2(j-n)\rangle - \frac{1}{6\alpha^4}k_1(m) & \text{otherwise.} \end{cases} \end{aligned} \tag{A.2}$$

Denote the real and imaginary parts of $k_3(n,n,m)$ as $k_{3x}(n,n,m)$ and $k_{3y}(n,n,m)$ respectively. Similarly, denote the real and imaginary parts of $k_1(m)$ as $k_{1x}(m)$ and

$k_{1y}(m)$ respectively. Using the stochastic difference equation, Equation 2.4, and Equation A.2 we obtain the difference equations

$$\begin{aligned} k_{3x}(n,n,m) &= E_2 \cos\theta\, k_{3x}(n-1,n-1,m-1) \\ &\quad + E_2 \sin\theta\, k_{3y}(n-1,n-1,m-1) \end{aligned} \tag{A.3}$$

and

$$\begin{aligned} k_{3y}(n,n,m) &= -E_2 \sin\theta\, e^{-\alpha^2/2} k_{3x}(n-1,n-1,m-1) \\ &\quad + E_2 \cos\theta\, e^{-\alpha^2/2} k_{3y}(n-1,n-1,m-1) \end{aligned} \tag{A.4}$$

with the following boundary values

$$k_{3x}(0,0,m) = 0, \tag{A.5}$$

$$k_{3y}(0,0,m) = \frac{-1}{6} k_{1y}(m), \tag{A.6}$$

$$k_{3x}(n,n,0) = 0 \quad \text{and} \tag{A.7}$$

$$k_{3y}(n,n,0) = \frac{-1}{6} k_{1y}(0)\, E_1^n\, e^{-n\alpha^2/2}. \tag{A.8}$$

Take the double $\mathcal{Z}$-transform of $k_{3x}(n,n,m)$ and $k_{3y}(n,n,m)$:

$$K_{3x}(w,w,z) = \sum_{n=0}^{\infty}\sum_{m=0}^{\infty} k_{3x}(n,n,m)\, w^{-n} z^{-m} \tag{A.9}$$

and

$$K_{3y}(w,w,z) = \sum_{n=0}^{\infty}\sum_{m=0}^{\infty} k_{3y}(n,n,m)\, w^{-n} z^{-m}. \tag{A.10}$$

The double $\mathcal{Z}$-transform of $k_3(n,n,m)$ can be obtained by combining Equations A.5 to A.10

$$\begin{aligned} K_3(w,w,z) &= \sum_{n=0}^{\infty}\sum_{m=0}^{\infty} k_3(n,n,m)\, w^{-n} z^{-m} \\ &= \frac{-i}{6}\left[K_{1y}(z) + \frac{k_{1y}(0) E_1 e^{-\alpha^2/2} w^{-1}}{1 - E_1 e^{-\alpha^2/2} w^{-1}}\right] \\ &\quad \times \frac{1 - E_2 e^{i\theta} w^{-1} z^{-1}}{1 - E_2 \cos\theta (1 + e^{-\alpha^2/2}) w^{-1} z^{-1} + E_2^2 e^{-\alpha^2/2} w^{-2} z^{-2}}, \end{aligned} \tag{A.11}$$

where $K_{1y}(z)$ is the $\mathcal{Z}$-transform of $k_{1y}(m)$. The $\mathcal{Z}$-transform of $k_{1(3)}(m)$ evaluated on the unit circle of the complex $\mathcal{Z}$-plain gives $K_{1(3)}(\omega)$. Using Equation A.1

$$K_{1(3)}(\omega) = -3\alpha^2 K_3(1, 1, e^{-i\omega T_R}). \tag{A.12}$$

Combining the last two equations together with $K_1(\omega)$ in Equation 2.49 gives

$$K_{1(3)}(\omega) = \frac{\alpha^2 K_1(\omega)}{2}\left[Y(\omega) + \frac{E_1 e^{-\alpha^2/2}}{1 - E_1 e^{-\alpha^2/2}}\right] \tag{A.13}$$

where

$$Y(\omega) = \frac{1 - E_2 \cos\theta\, e^{i\omega T_R}}{D(\omega)}$$

and

$$D(\omega) = 1 - E_2 \cos\theta(1 + e^{-\alpha^2/2})\, e^{i\omega T_R} + E_2^2\, e^{-\alpha^2/2}\, e^{2i\omega T_R}.$$

Appendix B

Non-zero Mean Binary Quadrature Excitation

Consider the binary quadrature excitation sequence $\boldsymbol{\alpha}(n) = [\alpha_x(n) + \frac{\mu}{\sqrt{2}}, \alpha_y(n) + \frac{\mu}{\sqrt{2}}, 0]^T$ where $\alpha_x(n)$ and $\alpha_y(n)$ are independent and each takes on the values $\pm\frac{\alpha}{\sqrt{2}}$ with equal probability. Define the RF magnitude and phase, respectively, as

$$\begin{aligned} \beta(n) &= \sqrt{\boldsymbol{\alpha}^T(n)\,\boldsymbol{\alpha}(n)} \\ &= \sqrt{\alpha^2 + \mu^2 + \sqrt{2}\mu[\alpha_x(n) + \alpha_y(n)]} \end{aligned} \tag{B.1}$$

and

$$\phi(n) = \tan^{-1}\left[\frac{\alpha_y(n) + \mu/\sqrt{2}}{\alpha_x(n) + \mu/\sqrt{2}}\right]. \tag{B.2}$$

The RF rotation matrix $\boldsymbol{R}_\alpha(n)$ is given by Equation 2.55, which has a mean

$$\boldsymbol{\mu}_R = \begin{bmatrix} \frac{1+\mu_1}{2} & \mu_2 & -\mu_3 \\ \mu_2 & \frac{1+\mu_1}{2} & \mu_3 \\ \mu_3 & -\mu_3 & \mu_1 \end{bmatrix} \tag{B.3}$$

where

$$\mu_1 = \frac{1}{2}(\cos\alpha\,\cos\mu + \cos\sqrt{\alpha^2+\mu^2}), \tag{B.4}$$

$$\mu_2 = \frac{1}{4}\left[1 - \cos\alpha\,\cos\mu - \frac{\alpha^2-\mu^2}{\alpha^2+\mu^2}\,(1 - \cos\sqrt{\alpha^2+\mu^2})\right] \text{ and} \tag{B.5}$$

$$\mu_3 = \frac{1}{4\sqrt{2}}\left[\sin(\alpha+\mu) - \sin(\alpha-\mu) + \frac{2\mu}{\sqrt{\alpha^2+\mu^2}}\,\sin\sqrt{\alpha^2+\mu^2}\right]. \tag{B.6}$$

Using Equation 2.6 the mean magnetization is

$$\begin{aligned}\boldsymbol{\mu}_M &= (1-\boldsymbol{\mu}_R\boldsymbol{R}_\theta)^{-1}\boldsymbol{\mu}_R\boldsymbol{C} \\ &= \frac{M_c(1-E_1)}{D}\begin{bmatrix} \mu_3E_2(\cos\theta+\sin\theta)(\mu_2+\frac{1+\mu_1}{2})-\mu_3 \\ \mu_3E_2(\sin\theta-\cos\theta)(\mu_2+\frac{1+\mu_1}{2})+\mu_3 \\ \left\{\mu_1[1-E_2(1+\mu_1)\cos\theta-E_2^2\mu_2^2+E_2^2\left(\frac{1+\mu_1}{2}\right)^2] \right. \\ \left. +2E_2\mu_3^2[E_2(\mu_2+\frac{1+\mu_1}{2})-\cos\theta]\right\}\end{bmatrix} \qquad \text{(B.7)}\end{aligned}$$

where

$$\begin{aligned}D &= (1-E_1\mu_1)\left[1-E_2(1+\mu_1)\cos\theta-E_2^2\mu_2^2+E_2^2\left(\frac{1+\mu_1}{2}\right)^2\right] \\ &\quad -2E_1E_2\mu_3^2\left[E_2(\mu_2+\frac{1+\mu_1}{2})-\cos\theta\right]. \qquad \text{(B.8)}\end{aligned}$$

Define $\boldsymbol{\mu}_{\alpha x} = \langle \boldsymbol{R}_\alpha(n)\,\alpha_x(n)\rangle$ and $\boldsymbol{\mu}_{\alpha y} = \langle \boldsymbol{R}_\alpha(n)\,\alpha_y(n)\rangle$, then

$$\boldsymbol{\mu}_{\alpha x} = \begin{bmatrix} p & r & -s \\ r & q & t \\ s & -t & -2r \end{bmatrix} \qquad \text{(B.9)}$$

and

$$\boldsymbol{\mu}_{\alpha y} = \begin{bmatrix} q & r & -t \\ r & p & s \\ t & -s & -2r \end{bmatrix} \qquad \text{(B.10)}$$

where

$$p = \frac{\alpha}{4\sqrt{2}}\left[\frac{2\alpha\mu}{\alpha^2+\mu^2}(1-\cos\sqrt{\alpha^2+\mu^2})-\sin\alpha\,\sin\mu\right], \qquad \text{(B.11)}$$

$$q = \frac{-\alpha}{4\sqrt{2}}\left[\frac{2\alpha\mu}{\alpha^2+\mu^2}(1-\cos\sqrt{\alpha^2+\mu^2})+\sin\alpha\,\sin\mu\right], \qquad \text{(B.12)}$$

$$r = \frac{\alpha}{4\sqrt{2}}\sin\alpha\,\sin\mu, \qquad \text{(B.13)}$$

$$s = \frac{\alpha}{4}\left[\sin\alpha\,\cos\mu-\frac{\alpha}{\sqrt{\alpha^2+\mu^2}}\sin\sqrt{\alpha^2+\mu^2}\right] \quad \text{and} \qquad \text{(B.14)}$$

$$t = \frac{\alpha}{4}\left[\sin\alpha\,\cos\mu+\frac{\alpha}{\sqrt{\alpha^2+\mu^2}}\sin\sqrt{\alpha^2+\mu^2}\right]. \qquad \text{(B.15)}$$

The input-output cross-covariance is then given by

$$k_1(m) = \frac{1}{\alpha^2} \boldsymbol{B}^\dagger (\boldsymbol{\mu}_R \boldsymbol{R}_\theta)^m \boldsymbol{A} \boldsymbol{B} \tag{B.16}$$

where $\boldsymbol{B} = [1, -i, 0]^T$,

$$\begin{aligned} \boldsymbol{A} &= \langle \boldsymbol{M}(n) \boldsymbol{\alpha}^T(n) \rangle - \boldsymbol{\mu}_M \boldsymbol{\mu}_\alpha^T \\ &= \left[\boldsymbol{\mu}_{\alpha x}(\boldsymbol{R}_\theta \boldsymbol{\mu}_M + \boldsymbol{C}), \quad \boldsymbol{\mu}_{\alpha y}(\boldsymbol{R}_\theta \boldsymbol{\mu}_M + \boldsymbol{C}), \quad \mathbf{0} \right] \end{aligned} \tag{B.17}$$

and $\mathbf{0} = [0, 0, 0]^T$. Fourier transformation of $k_1(m)$ gives $K_1(\omega)$.

Appendix C

Theoretical Calculation of Variance

Theoretical calculation of the variances of $k_1^N(m)$ and $r^N(m)$ is a laborous process. The results are usually in the form of difference equations which can only be studied numerically. The steps are outlined here for the variance of $k_1^N(m)$ for random binary quadrature excitation.

Consider the binary excitation sequence $\boldsymbol{\alpha}(n) = [\alpha_x(n), \alpha_y(n), 0]^T$ where $\alpha_x(n)$ and $\alpha_y(n)$ are independent and each takes on the values $\pm\alpha/\sqrt{2}$ with equal probability. The RF magnitude and phase are, respectively, α and

$$\phi(n) = \tan^{-1} \frac{\alpha_y(n)}{\alpha_x(n)}. \tag{C.1}$$

The RF rotation matrix $\boldsymbol{R}_\alpha(n)$ and its mean $\boldsymbol{\mu}_R$ are given by Equations 2.55 and 2.56 respectively.

The variance of $k_1^N(m)$ is defined as

$$Var\{k_1^N(m)\} = \langle |k_1^N(m)|^2 \rangle - |k_1(m)|^2 \tag{C.2}$$

Using the expression of $k_1^N(m)$ in Equation 3.2 the first term on the right is

$$\langle |k_1^N(m)|^2 \rangle = \frac{1}{N^2\alpha^4} \sum_{n=0}^{N-1} \sum_{j=0}^{N-1} \boldsymbol{B}^\dagger \langle \Gamma^T(n-m)\boldsymbol{M}(n)\boldsymbol{M}^T(j)\Gamma(j-m) \rangle \boldsymbol{B} \tag{C.3}$$

where $\boldsymbol{B} = [1, -i, 0]^T$ and

$$\Gamma(n) = \begin{bmatrix} \alpha_x(n) & -\alpha_y(n) & 0 \\ \alpha_y(n) & \alpha_x(n) & 0 \\ 0 & 0 & 0 \end{bmatrix}. \tag{C.4}$$

When $n = j$, $\langle \Gamma^T(n-m)\boldsymbol{M}(n)\boldsymbol{M}^T(j)\Gamma(j-m)\rangle = \alpha^2 P$ where P is the average signal power. When $n \neq j$,

$$\langle \Gamma^T(n-m)\boldsymbol{M}(n)\boldsymbol{M}^T(j)\Gamma(j-m)\rangle = \langle \Gamma^T(j-m)\boldsymbol{M}(j)\boldsymbol{M}^T(n)\Gamma(n-m)\rangle^* \tag{C.5}$$

where the symbol * is the complex conjugate operator. Therefore, it is only necessary to consider $n > j$.

When $n - m > j$, iterating Equation 2.4 gives

$$\begin{aligned} &\langle \Gamma^T(n-m)\boldsymbol{M}(n)\boldsymbol{M}^T(j)\Gamma(j-m)\rangle = \\ &\quad (\boldsymbol{\mu}_R\boldsymbol{R}_\theta)^m \langle \Gamma^T(n-m)\boldsymbol{R}_\alpha(n-m)\boldsymbol{R}_\theta\rangle (\boldsymbol{\mu}_R\boldsymbol{R}_\theta)^{n-j-m-1}\langle \boldsymbol{M}(j)\boldsymbol{M}^T(j)\Gamma(j-m)\rangle \\ &\quad +(\boldsymbol{\mu}_R\boldsymbol{R}_\theta)^m \langle \Gamma^T(n-m)\boldsymbol{R}_\alpha(n-m)\rangle [(\boldsymbol{R}_\theta\boldsymbol{\mu}_R)^{n-j-m-1} + \cdots + \boldsymbol{I}] \\ &\qquad \times \boldsymbol{C}\langle \boldsymbol{M}^T(j)\Gamma(j-m)\rangle. \end{aligned} \tag{C.6}$$

The second term on the right can be obtained by straightforward manipulations:

$$\frac{M_e^2(1-E_1)^2\alpha^2 \sin^2\alpha (E_2 \cos^2\frac{\alpha}{2})^{2m}[1-(E_1\cos\alpha)^{n-j-m}]}{(1-E_1\cos\alpha)^2} \times \begin{bmatrix} \sin^2 m\theta & \sin m\theta\cos m\theta & 0 \\ \sin m\theta\cos m\theta & \cos^2 m\theta & 0 \\ 0 & 0 & 0 \end{bmatrix}.$$

The first term on the right of Equation C.6 can be obtained by solving a set of four simultaneous difference equations with the following four unknowns: $\langle M_x(j)M_z(j)\alpha_x(j-m)\rangle$, $\langle M_x(j)M_z(j)\alpha_y(j-m)\rangle$, $\langle M_y(j)M_z(j)\alpha_x(j-m)\rangle$ and $\langle M_y(j)M_z(j)\alpha_y(j-m)\rangle$.

When $n - m \leq j$, it can be shown that

$$\langle \Gamma^T(n-m)\boldsymbol{M}(n)\boldsymbol{M}^T(j)\Gamma(j-m)\rangle = (\boldsymbol{\mu}_R\boldsymbol{R}_\theta)^{n-j}\langle \Gamma^T(n-m)\boldsymbol{M}(j)\boldsymbol{M}^T(j)\Gamma(j-m)\rangle. \tag{C.7}$$

A set of nine simultaneous difference equations can be obtained with the nine unknowns being the nine components of $\langle \Gamma^T(n-m)\boldsymbol{M}(j)\boldsymbol{M}^T(j)\Gamma(j-m)\rangle$. By solving these two sets of simultaneous difference equations the variance of $k_1^N(m)$ can be calculated.